NUMERICAL SIMULATION AND EROSION PREDICTION FOR AN ELECTRICAL SUBMERSIBLE PUMP

A Dissertation

by

YIMING CHEN

Submitted to the Office of Graduate and Professional Studies of
Texas A&M University
in partial fulfillment of the requirements for the degree of

DOCTOR OF PHILOSOPHY

Chair of Committee,	Gerald Morrison
Committee Members,	Adolfo Delgado
	Je-Chin Han
	Robert E. Randall
Head of Department,	Andreas Polycarpou

December 2017

Major Subject: Mechanical Engineering

ABSTRACT

Electrical Submersible Pumps (ESP) are widely used in the oil industry to lift oil and gas at the same time with high efficiency. Many ESPs operate with multiphase flow – liquid, gas and a low concentration of sand, thus having problems of pressure degradation and erosion. To investigate these problems, a numerical method can be used, which provides details of the inner flow field. Using the commercial software ANSYS Fluent, 3D transient multiphase simulations are conducted for a Baker Hughes made ESP MVP-G400. The simulations focus on three parts: secondary flow path in multiphase flow, pressure degradation due to gas volume fraction and erosion prediction.

Aside from the main flow path, the clearances and balancing holes inside the ESP create a secondary path which enables the flow to recirculate. Although the volume flow rate in this path is low compared with the main flow path, the erosion in the secondary path cannot be neglected and can result in pump failure. In this research, a water-air-sand three phase simulation is performed on dual stages of the ESP, with all secondary path included.

Second part of this research focuses on the pressure degradation due to the presence of a gas phase, especially at the first stage near the pump inlet. The compressibility of gas and the bubble break-up and coalescence effects are considered using the Population Balancing Module in ANSYS Fluent.

The last part is the erosion prediction. A low concentration of sand is often inevitable during the operation of an ESP, causing erosion and reducing the life span of

the ESP. This erosion becomes more severe with the existence a of gas phase. The three-phase simulations with both Eulerian multiphase and particle tracking explain the erosion and the role of gas in this process, giving a reasonable qualitative prediction on the erosion of the ESP.

DEDICATION

To my loving parents, grandparents and my lovely wife

ACKNOWLEDGMENTS

I would like to express my gratitude to my advisor and committee chair, Dr. Gerald Morrison for all his help, support, understanding and guidance throughout my study. I would like to thank him for accepting me as a PhD student in his research team, and for all his precious time and effort supporting my research. He is a great mentor and always provides priceless trust, guidance, support, and encouragement to his students.

I would also like to thank my committee members, Dr. Han, Dr. Randall, and Dr. Delgado, for their guidance and support throughout the course of this research. Thanks to Dr. Strzelec for her help during the preliminary examination of this research.

Special thanks to Dr. Ahbay Patil for all his help in my research. Discussions of my research with him were always progressive and joyful. Special thanks to Dr. Yi Chen for all the kind guidance since I joined the lab. Thanks to all my friends and colleagues and staff in the Turbomachinery lab for all the help and support.

Thanks to Shell Oil Company for funding and providing me with all the knowledge and information I needed throughout my research.

Finally, thanks to my parents and grandparents for their encouragement and support. Thanks to my wife for all her dedication and understanding.

CONTRIBUTORS AND FUNDING SOURCES

This work was supervised by a dissertation committee consisting of Professor Morrison, Professor Delgado and Professor Han of the Department of Mechanical Engineering and Professor Randall of the Department of Ocean Engineering.

The experiment data for comparison was provided by Professor Morrison.

All other work conducted for the dissertation was completed by the student independently.

Graduate study was supported by funding from Shell Oil Company.

NOMENCLATURE

GVF	Gas Volume Fraction
CFD	Computational Fluid Dynamics
ESP	Electric Submersible Pump
Re	Reynolds Number
ΔP	Differential Pressure
Δt	Time step
v	Velocity
T	Temperature
$\dot{m}_g$	Mass flow rate of gas
$\dot{m}_l$	Mass flow rate of liquid
Q_l	Volume flow rate of liquid
Q_g	Volume flow rate of gas
ω	Pump speed
ρ_g	Gas density
ρ_l	Liquid density
P_i	Inlet pressure
P_o	Outlet pressure
v_i	Inlet velocity
v_o	Outlet velocity
ρ_i	Inlet density

k	Turbulent kinetic energy
$\overline{k_{w_0}}$	Reference turbulent kinetic energy
α_s	Sand volume fraction
V_s	Near wall sand velocity
$\overline{V_{s_0}}$	Reference sand velocity
EF	Erosion factor
ER	Erosion rate
BEP	Best efficient point
WS	Water and sand
WAS	Water, air and sand

TABLE OF CONTENTS

Page

LIST OF FIGURES

Page

LIST OF TABLES

Page

1. INTRODUCTION

The electrical submersible pump, typically called an ESP, is an efficient and reliable artificial-lift method for lifting moderate to high volumes of fluids from wellbores. A typical ESP is a multistage centrifugal pump with one impeller and one diffuser in each stage, as shown in Fig.1. All impellers are connected to the rotating shaft and diffusers are stationary. Every stage increases the pressure and redirects the flow to the next stage/outlet, providing high artificial lift ability for multiphase flow including liquid and gas. These volumes range from a low of 150 BPD to as much as 150,000 BPD. (Petrowiki 2016)

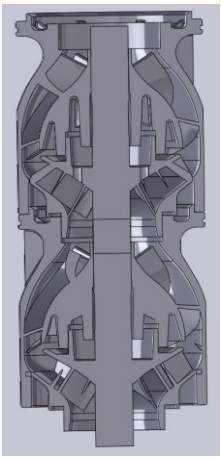

Figure 1. A section view of a two-stage ESP (Baker Hughes G400)

There are mainly two types of ESPs: radial flow pumps (Fig. 2a) and mixed flow pumps (Fig. 2b). In radial flow pumps, the head is generated with pure centrifugal action. Flow enters the impeller axially and leaves the impeller outlet radially. Then the diffuser redirects the flow to enter the impeller in the next stage axially. As the gas volume

fraction increases, the bubbles occupy a major portion of the impeller flow area until gas lock occurs (Barrios 2007). Mixed flow pumps are used to generate head from centrifugal force and impeller design. These pumps have better performance under multiphase conditions. (Gudigopuram 2016)

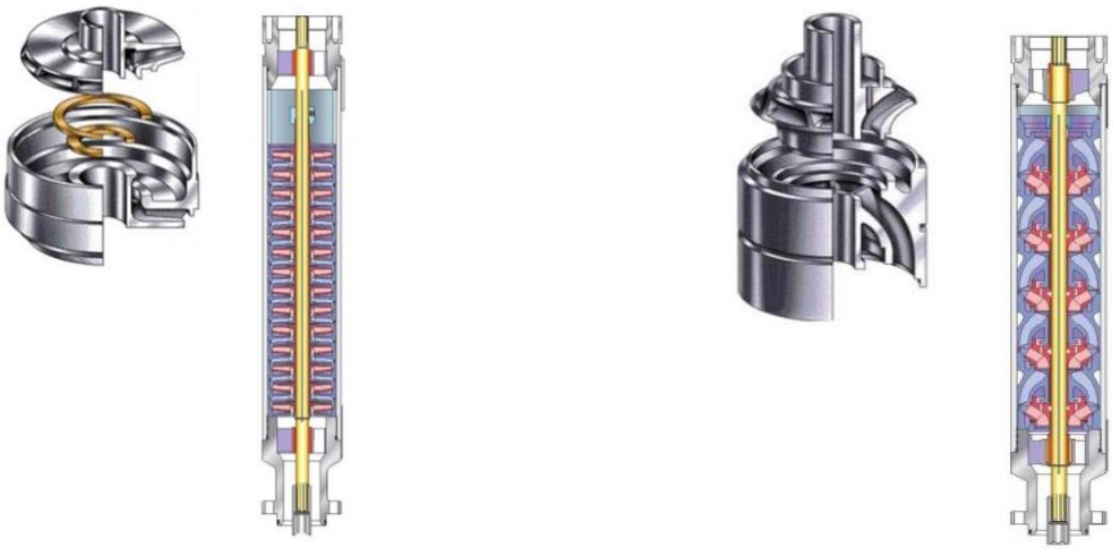

(a) (b)

Figure 2. ESP types (a) Radial flow (b) Mixed flow (Nguyen 2011)

ESPs are severely degraded by the presence of gas in their inlet. The resulting degradation can vary from a slight deterioration in the pump performance to surging and even to gas locking caused by entrained gas in the flow path. (Zhou, 2010)

To better handle the gas problem and improve the ESP performance under high gas volume fraction (GVF), the split-vane design of the impeller was adopted by pump manufacturers. The split-vane ESP generates pressure rise from centrifugal force and impeller design, just like other mixed flow ESPs. What makes it unique is that the impellers in split-vane ESPs consist of balancing holes and a multiset of blades, thus

granting the pump the capability to handle fluid with GVF up to 70% (Pirouzpanah 2014). The split vane impeller makes the flow more homogenized and helps reduce the accumulation of gas pockets near the vane. A schematic view of the MVP-G400 pump from Baker Hughes is shown in Fig. 3.

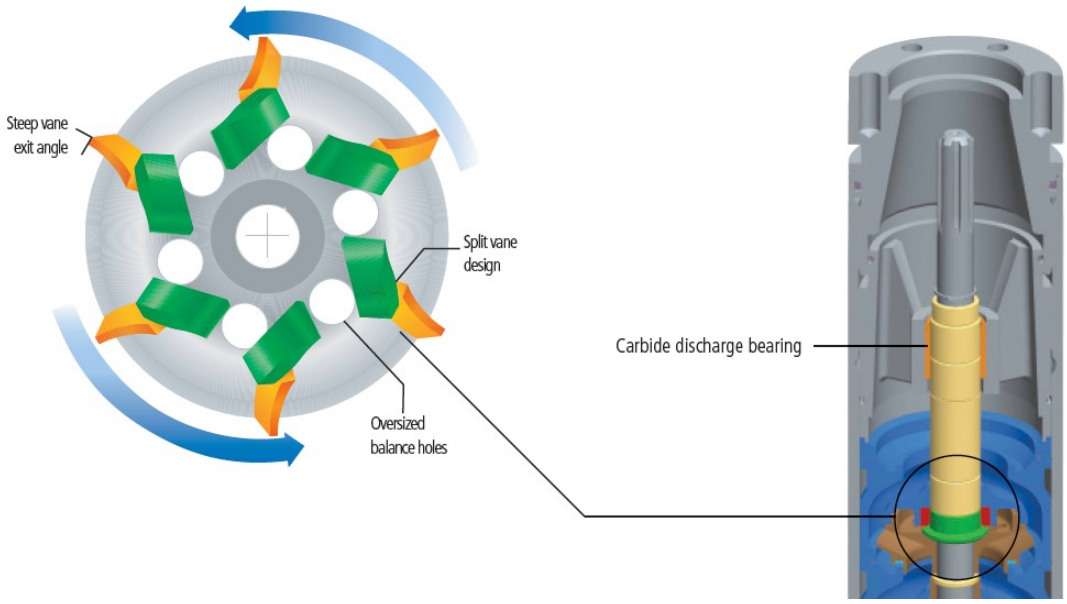

Figure 3. Schematic views of the MVP pump impeller (Baker Hughes 2010)

The split-vane ESPs can be used separately or combined with traditional ESP for better performance under high GVF. In industry, they are located at the inlet of ESPs to homogenize the fluid, increase the pressure of the flow and lower the GVF for the other stages.

Although ESPs have the advantage of handling large volume flow rates with high GVF, the cost is a main factor which preventing the oil industry to increase the use of ESPs. With the high manufacture and installation cost, the lifespan of the ESP becomes

crucial for further reducing the cost of the ESP in the oil industry. One of the main reasons for the ESP to fail is the erosion. Most ESPs are designed for multiphase flow including liquid and gas, but not for sand. However, in the real usage, small amount of sand particles are inevitably sucked into the pump inlet and cause severe erosion, resulting in pressure degradation and a much shorter pump lifespan than designed. Thus for the industry to better take the advantages of ESPs, further research and improvement should be made to extend the lifespan and lower the cost.

1.1 Literature review

To solve the aforementioned problem, researchers and engineers become interested in analysis of the erosion mechanism as well as the flow field inside ESPs. Both experimental and numerical approaches have been made by previous researchers. Since ESPs are multistage centrifugal pumps, not only research progresses on ESPs but also on other centrifugal pumps are reviewed in this part.

1.1.1 Experimental studies

Mitsukiyo and Kiyoshi (1974a) are the first group who conducted a comprehensive study on centrifugal pumps working with gas. They made the observation that the head degradation changes with flow rates and GVF due to the change of gas-liquid flow patterns in the impeller. They conducted the tests under different GVFs and successfully identified different flow regimes of the gas-liquid mixture: isolated bubble, bubbly flow, slug flow and segregated gas. According to their research, while the GVF>4% there was a considerable drop in the head developed by the impeller due to bubble disturbing the flow condition. Fig. 4 shows the changes in the

flow pattern and velocity triangle due to the presence of air bubbles. This was mainly due to the density change of the mixture that directly affected the momentum of the flow. They also observed a negative pressure gradient at the leading edge of the blade that reduced the speed of the bubbles, causing the accumulation of some bubbles on the suction side of the blade near the leading edge.

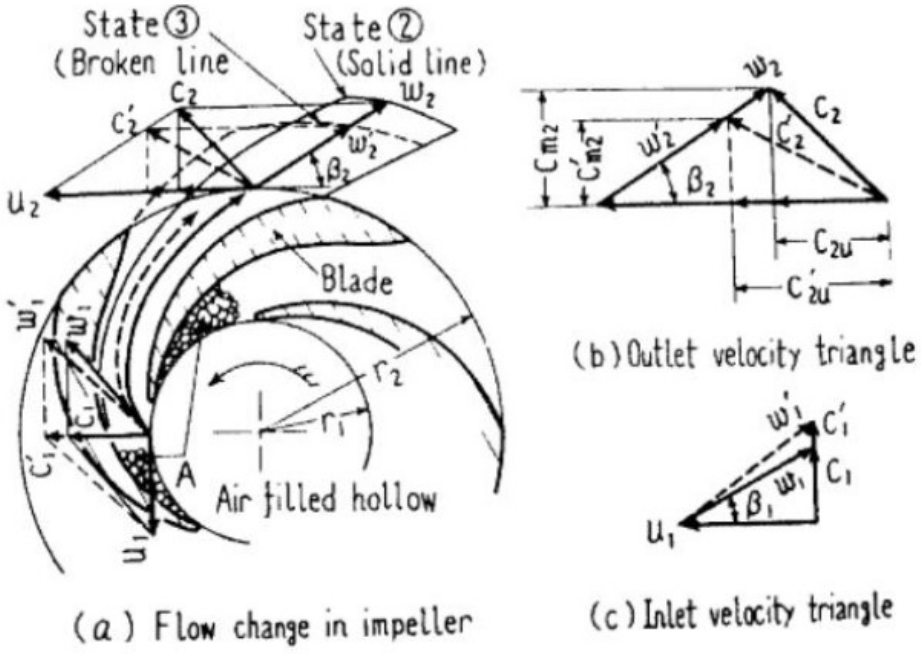

Figure 4. Flow pattern change due to the change of GVF (Mitsukiyo, *et al*, 1974a)

Mitsukiyo and Kiyoshi (1974b) carried out another study on the effect of number of blades on the performance of the pump (Fig. 5). They made the conclusion that a low amount of air bubbles shifts the mean flow to the suction side of the impeller and consequently change the peripheral component of the absolute velocity which results in a rise in the pressure head. According to the authors, the bubble size reduces when the rotating speed decreases or the number of blades increases.

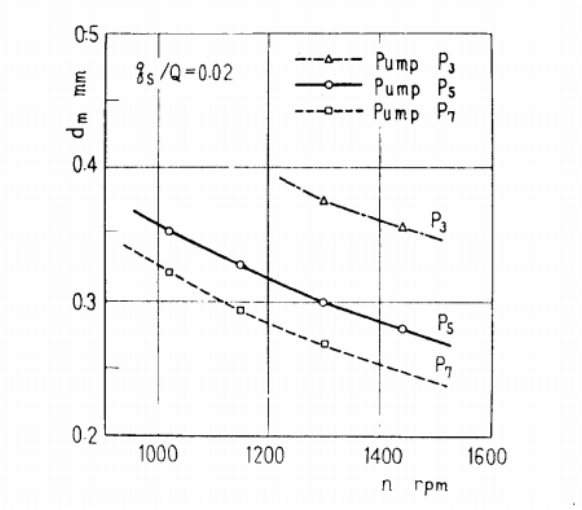

Figure 5. Bubble diameters against pump speeds (Mitsukiyo, *et al*, 1974b)

Lea, *et al*., (1982) conducted the first report on a two phase ESP pump available in the industry. They conducted tests on three different pumps. Air-water test on a 5 stage I-42 pump; Diesel-CO2 tests on I-42B, C-72 and K-70 pumps. The I-42 and C-72 were radial pumps and K-70 was mixed flow pump. Their test facility was designed to operate up to 400 psi with the maximum GVF of 50%. According to their results, the pump performance was seen to be dependent on inlet pressure, type of fluid, gas volume fraction and pump type. By increasing GVF, the amount of head degradation increases and the operating flow rate range of the pump decreases. Decreasing the air content and increasing the inlet pressure enhances the performance of the pumps. Meanwhile, increasing inlet pressure increases the flow rate operation range of the pumps.

Sekoguchi (1984) studied the variation of void fraction within a transparent impeller using electric resistivity probe. For low inlet gas volume fractions bubble flow was observed. By increasing the flow rate of the pump, the onset of formation of air slugs within the impeller increases. Then surge was observed when the air slug starts to

leave the impeller. These slugs occupy a substantial portion of the cross section of the impeller, resulting in a significant increase in the velocity of the liquid phase. The velocity slippages between the phases are an important factor pertaining to head degradation.

Sato *et al*. (1996) performed flow visualization on a centrifugal pump with a vane-less diffuser. They used a transparent shrouded impeller to observe the flow inside the pump. According to the authors, the gas pockets were formed on the pressure side of the impeller, and become larger with the increase of GVF. They also observed that the size of the gas pocket directly affected the pump head degradation as when the gas accumulated on the impeller increased, the pump head decreased.

Poullikkas (2003) conducted an experiment to visualize the bubble motion within the impeller of nuclear reactor cooling pumps. The author observed that at low gas contents the gas bubbles tend to concentrate at the impeller eye on the blade suction side, adjacent to the back plate of the impeller; at medium gas contents gas accumulations advances towards the passage length, width and height of the impeller; at “high” gas contents (around 9 percent by volume) passage blockage and break in the pump flow occurs. This type of the pump limits the maximum GVF, so their “high” GVF condition are not the high GVF conditions usually observed in ESPs.

Barrios (2007) studied the two phase flow in an ESP and used a high speed camera to visualize the flow in an impeller stage. The impeller was an open-type impeller to facilitate the visualization throughout the blades. The author observed the gas

accumulation on the pressure side of the impeller blades at high GVF. She also observed that bubble size played an important role in the pressure head degradation.

Izturiz, D. L. *et al.* (2007) performed an experimental study which focused on the effect of bubble size at the inlet of an ESP under two phase flow (air-water). The results showed that bubble dynamic (drag and buoyancy forces) along with gas volumetric and suction pressure are factors of decisive importance in the ESP's performance. Bubble size shows sensibility to inlet pressure changes. Important variables such as flow rate as well as GVF did not show any significant effect. Furthermore, it was found that temperature does not show significant influence in pump performance when operating with air-water multiphase flow.

Gamboa, J. *et al.* (2010) studied the gas pocket behavior through the visualization of the flow pattern within an ESP impeller at different operation conditions and fluid properties. In his experiment, the maximum inlet GVF is up to 10%, with an inlet pressure of 2 psi and the rotation speed ranges from 600 rpm to 1000 rpm. This test condition has a relatively low inlet pressure and low rotation speed compared with the other researchers' test, but the results are satisfying and clearly show the isolated bubbles, bubble flow, gas pocket and segregated gas region (Fig. 6).

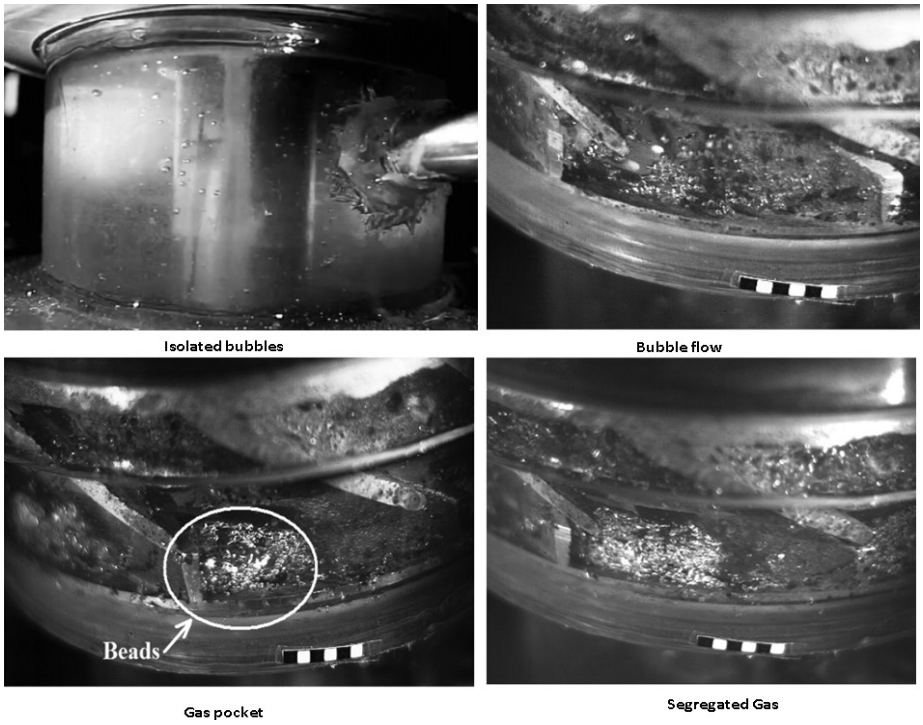

Figure 6. Various flow patterns for the two phase flow in the first impeller (Gamboa 2010)

With the data and visualization results, the researchers made a series of conclusion, including the rotational speed-surging relation, gas density, and surface tension effect. The critical surging GVF moves higher as the rotation speed increases. They also observed a stagnant gas pocket that causes the surging. For high liquid flow rates, the surging is associated with an unstable gas pocket, leading to an unstable stage performance. While surging at low liquid flow rates is related to a stable gas pocket that can be segregated to the back shroud of impeller. They also concluded that the bubble size at the stage inlet plays a key role in the two-phase performance of an ESP, which explains the difference in performance between a single stage and multistage arrangement.

To study experimentally the effect of number of stages on the overall performance of a multistage ESP, Salehi, E. *et al.* (2013) conducted a series of experiments injecting gas at certain stages and monitoring the pressure increment on stages downstream from the injection point at different inlet pressure, and rotational speed. Their experiment covers a wide range of factors affecting the performance of an ESP. As GVF increases, the ESP stage performance deteriorates; the deterioration is very mild until the GVF reaches a critical value where surging initiates. After this point, the rate of deterioration becomes a function of stage number. In an interval of quality starting from the quality at which surging initiates at the first stage, the stages closest to the gas injection point suffer head deterioration while the stages beyond this point deteriorate very mildly. As this quality interval ends, the rate of deterioration becomes severe in all the stages specifically last stages. Their experiment result shows the first stage is crucial in the surging phenomenon when GVF increases.

Kirkland (2012) designed a test loop for evaluating the performance of a split-vane ESP made by Baker Hughes, MVP-G470. This pump was installed in a vertical configuration using air and water as test fluids. Pirouzpanah (2014) performed detailed studies on the same pump using stage by stage pressure measurements. The head degradation of the pump increases with increase in GVF.

In the same lab and similar test condition, Zheng D.(2014) performed a detailed study on the WJE-1000 ESP, a mixed flow ESP manufactured by Baker Hughes. Steck D. (2014) performed a similar test on the MVP-G400 ESP, a split vane pump made by the same manufacturer. Although made by the same company, these three ESPs

exhibited different performance in the water-sand wear test and water-air-sand wear test. The mixed flow pump, WJE-1000, survived much longer in the wear test than the other two split vane ESPs. The failure of the WJE-1000 pump was caused by the erosion of bearings in the secondary flow path, while the main cause of failure for the other two ESPs was the erosion on the impeller blades. These results shows there are different mechanisms in the erosion process of the pump, and the design of pump clearance and blades plays a critical role in the capability of wear resistance. Another interesting discovery is the stage by stage pressure increase. When the test was carried in the water-sand condition, the first stage pressure rise is almost the same level compared with other stages. However, when it comes to water-air-sand test, the first stage pressure rise significantly reduced to less than half of other stages (20% GVF in the pump inlet). This result means there were something “special” happening only at the first stage near the inlet when gas was added. The pressure degradation of G400 under water-sand flow condition and water-air-sand condition are shown in Fig.7 and Fig.8.

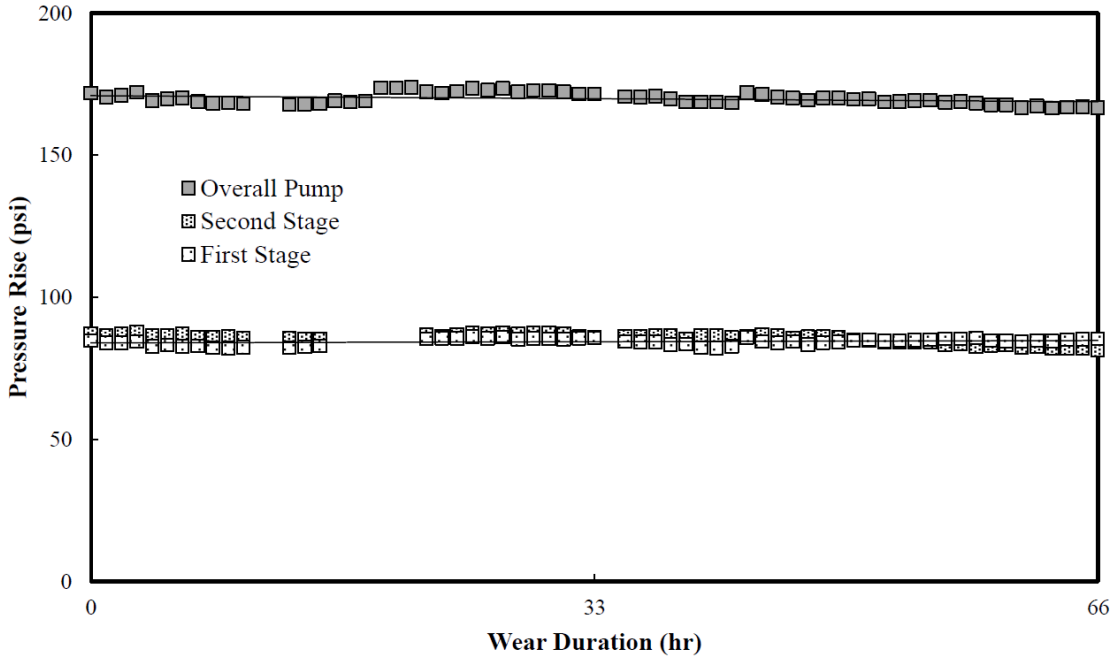

Figure 7. Pressure degradation during Water-Sand, wear (data obtained at 0% GVF) (Steck, D. 2014)

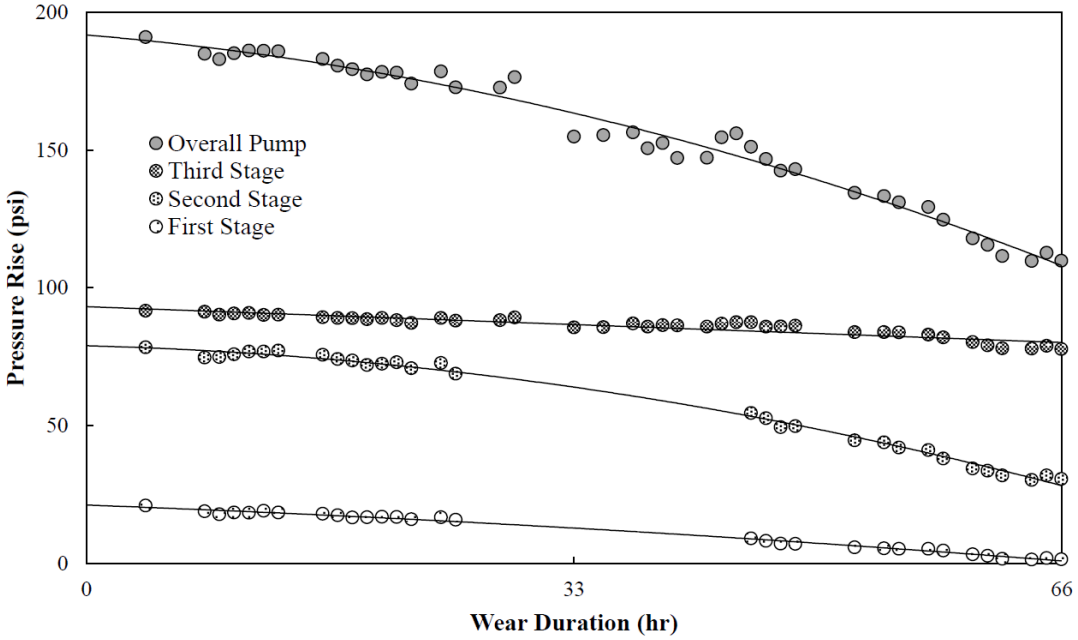

Figure 8. Pressure degradation during Water-Air-Sand, wear (data obtained at 20% GVF) (Steck, D. 2014)

1.1.2 Numerical simulations on ESP performance

Caridad *et al.* (2004) conducted a 3D simulation on a radial ESP impeller working with liquid-gas multiphase flow to predict the performance of the pump. This simulation method used a mixture k-ε model with pressure inlet and mass flow outlet boundary condition. He also studied the bubble size effect. With regard to the bubble diameter, there is a direct correspondence between this variable and the gas pocket size. Thus, even though the drag force increases as the bubble diameter augments (proportionally to the surface area of the bubble), the force due to the adverse pressure gradient increases even more (proportionally to the volume of the bubble), causing the big bubbles to accumulate easier than those of small diameters. The performance prediction was not satisfying, as shown in Fig. 9, it over predicts the head by 20% to 50%. According to the author, this could be caused by the simulation of only the impeller without the diffuser.

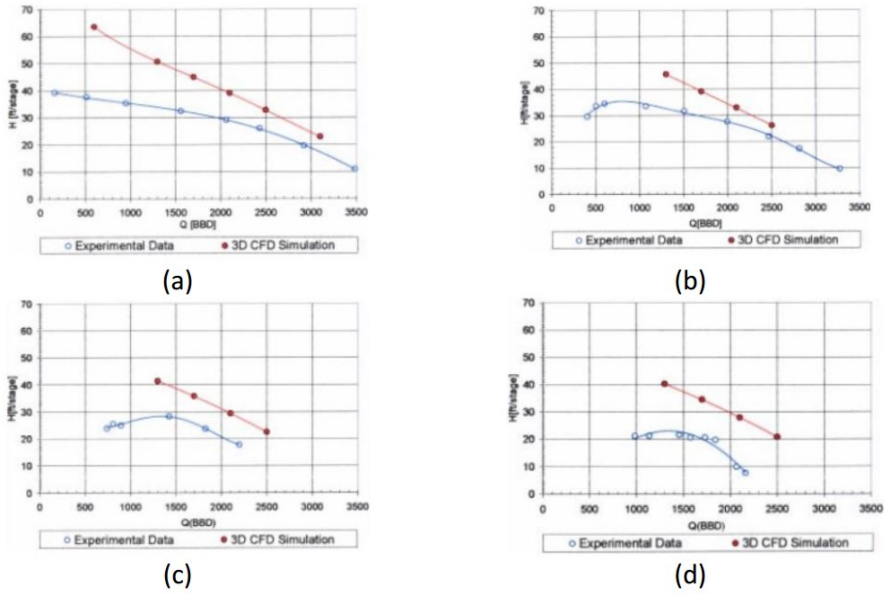

Figure 9. Pump performance for (a) Single phase flow (b) 10% GVF, bubble diameter = 0.1 mm (c) 15% GVF, bubble diameter = 0.1 mm (d) 17% GVF, bubble diameter = 0.1 mm (Caridad et al. 2004)

Barrios (2007) performed single phase and two phase simulations on a mixed flow impeller of an ESP to predict the performance and flow field. This simulation was done using the k-ε turbulence model and Eulerian multiphase model. A fixed bubble diameter obtained from the visualization was applied in the simulation. Although the GVF is very low in this simulation, the result did show the bubble concentration at certain area near the impeller blades, as shown in Fig.10.

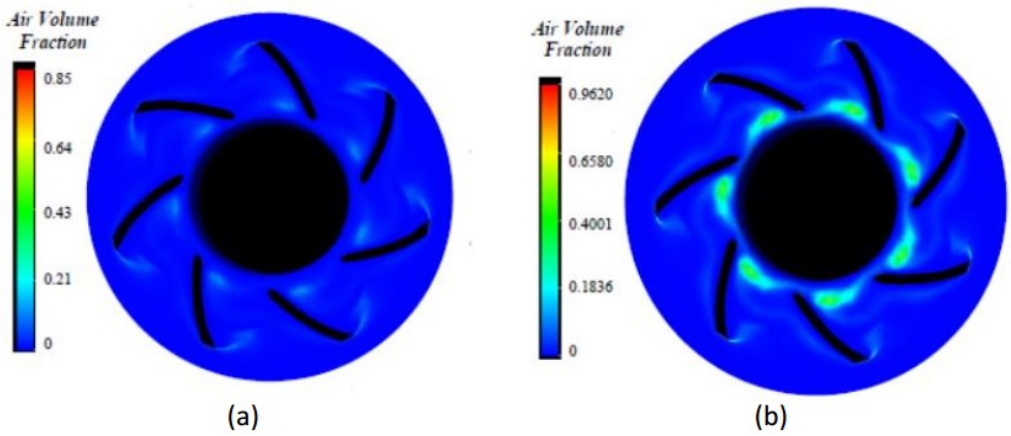

Figure 10. Air volume fraction for 500 BPD, 1500 RPM at (a) 0.05% GVF (b) 0.1% GVF (Barrios 2007)

Marsis, E. (2012) performed unsteady simulations for the split-vane ESP, MVP-G470. Simulations for both single-phase flow (water) and two-phase flow (water-air) were done with the multiphase Eulerian method and a further study on the optimization of blades was also performed by CFD. This is a fixed bubble size simulation. According to the author, the special head degradation in the first stages inlet is caused by inhomogeneous distribution of gas in the incoming flow. After adjusting the inlet gas distribution according to experiment condition, the result matches the experiment well. The gas distribution near the inlet is shown in Fig. 11. In this research the author also performed a test simulation with periodic boundary conditions and steady state simulation. Comparing with the transient simulation with the whole geometry and experiment results, the author made the conclusion that the use of periodic boundary conditions and steady state simulation is inappropriate.

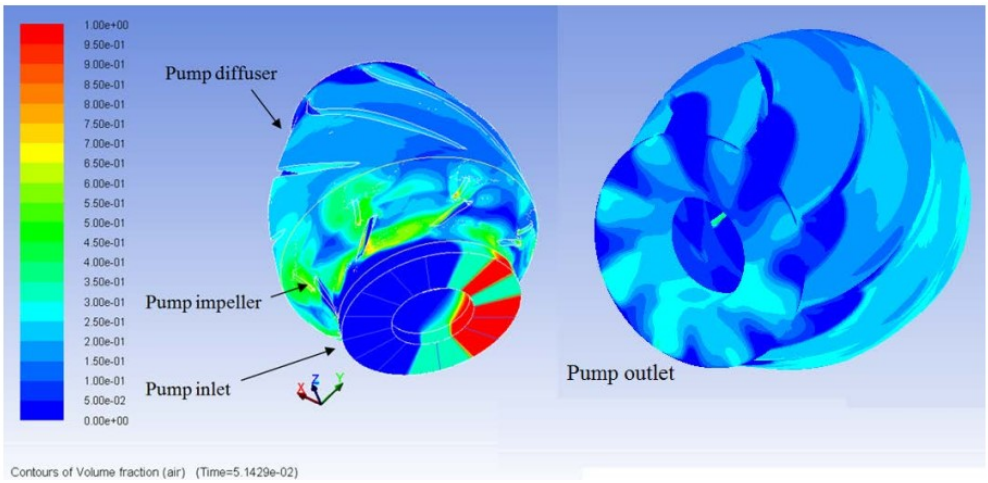

Figure 11. Pump inlet and first stage GVF distribution at inlet conditions of 20% GVF and 25 KBPD (Marsis, E. 2012)

Zhu, J. *et al.*(2014) performed a simulation of ESP under gassy conditions and made some estimation on the bubble size. This research focuses on a multistage simulation with periodic boundary conditions – only 1/5 of impeller and 1/9 of diffuser were simulated. This is a steady state simulation with the k-ε turbulence model and Eulerian multiphase model. The simulation of performance compared with experiment is shown in Fig.12. The simulation matches the experiment well only in high flow rate zones. The CFD result's deviation from the experiment could be caused by the steady state simulation. Referring to Marsis, E (2012)'s research, transient simulation with the whole pump should be performed instead of using periodic boundary conditions.

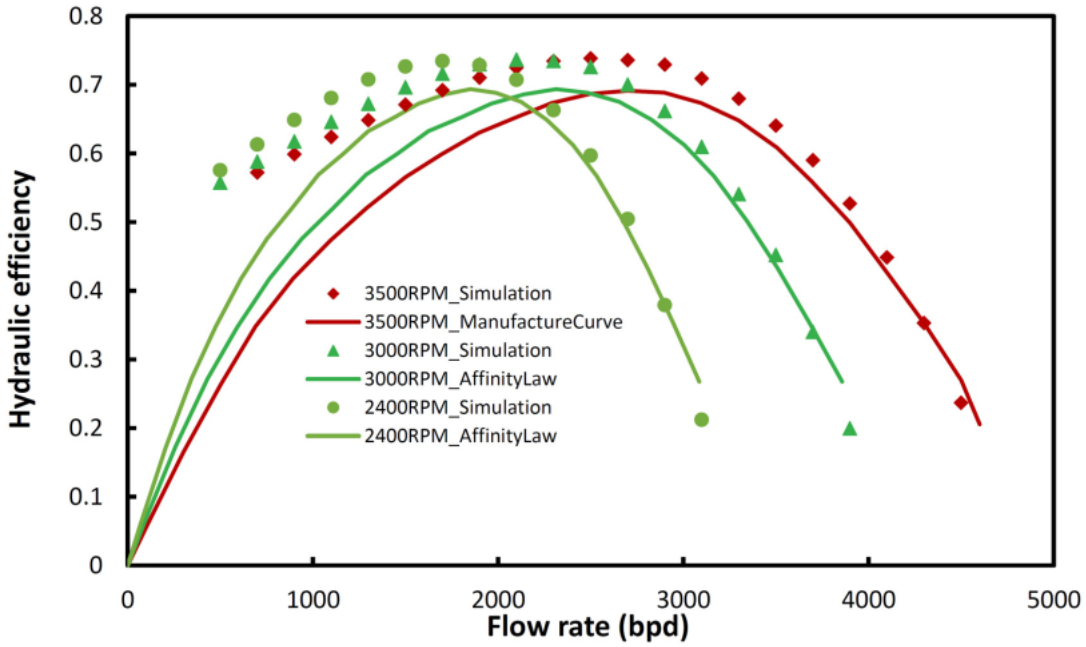

Figure 12. TE 2700 ESP single-phase performance curves (Zhu, J. *et al*. 2014)

One thing special in Zhu, J. *et al.*(2014) 's research is that the bubble size could be much bigger than 0.1~0.3mm range which other researchers observe and applies in their CFD. The author mentioned the bubble size may exceed 1.2 mm and large bubbles tend to move slower in the ESP.

Gudigopuram, S. (2016) performed a numerical simulation of the Poseidon ESP manufactured by Schlumberger, which is a helico-axial pump. His simulation was transient and stage by stage, which matches well with the experiment. The bubble size for this simulation is from the visualization observed data, 350 microns. For the first stage inlet, he applied Marsis, E. (2012)'s method and divided the inlet into different zones, allowing the incoming flow to have a ununiformed distribution of gas, as shown in Fig.13. The single phase simulations provided satisfying results, matching the

performance data from experiment. The water-air two phase simulations in this research showed that the head drop at higher GVF was due to slip between the phases. Because of this slip, stationary air pockets are observed on the pressure side of the impeller blade while minimizing the flow area. The author also suggested that the impeller blades must be redesigned in order to minimize the occurrence of air pockets and increase the head rise at higher GVF.

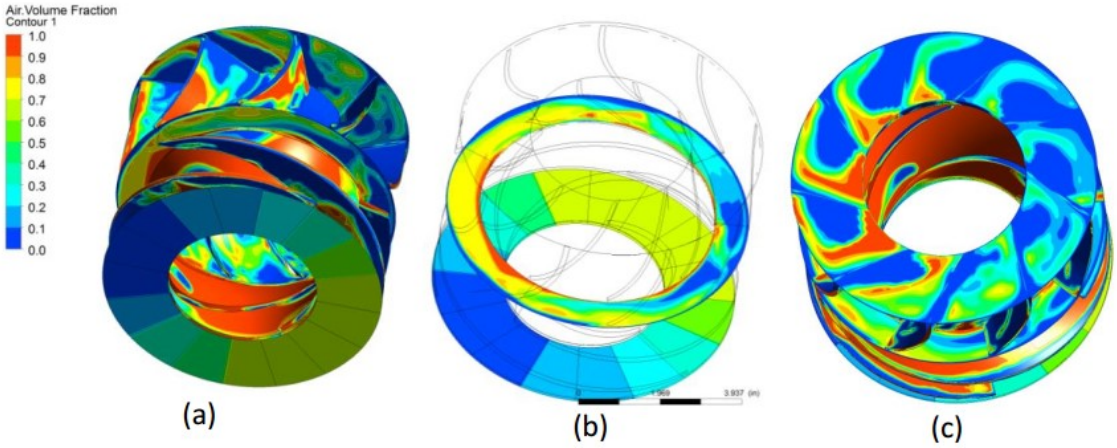

Figure 13. 1st stage air volume fraction contours for the flow conditions of 20 kBPD liquid flow rate, 50% GVF, 200 psig inlet pressure and 3600 RPM (a) Impeller inlet (b) Impeller-diffuser interface (c) Diffuser outlet

Pineda, H. *et al.* (2016) performed a phase distribution analysis in an ESP inlet handling water–air two-phase flow using CFD. They performed an unsteady multiphase simulation with Volume of Fluid (VOF) model in order to analyze and measure the void fraction at the inlet of an ESP and the effect of the gas in the head delivered by the first stage of this pump. In addition, the authors also made a comparison between the head results and experimental measurements. The results showed a higher scatter of the void fraction at higher rotation speeds. On the other hand, the head developed decreased with

higher gas flow rates and lower intake pressure. The average error between the experimental results and the numerical simulations was 25.6% and increased with higher rotation speed, probably due to the surging phenomenon present within the pump. The CFD result deviates from the experiment too much, which implies this simulation needs further improvement. Their comparison of CFD and experimental results are shown in Fig.14.

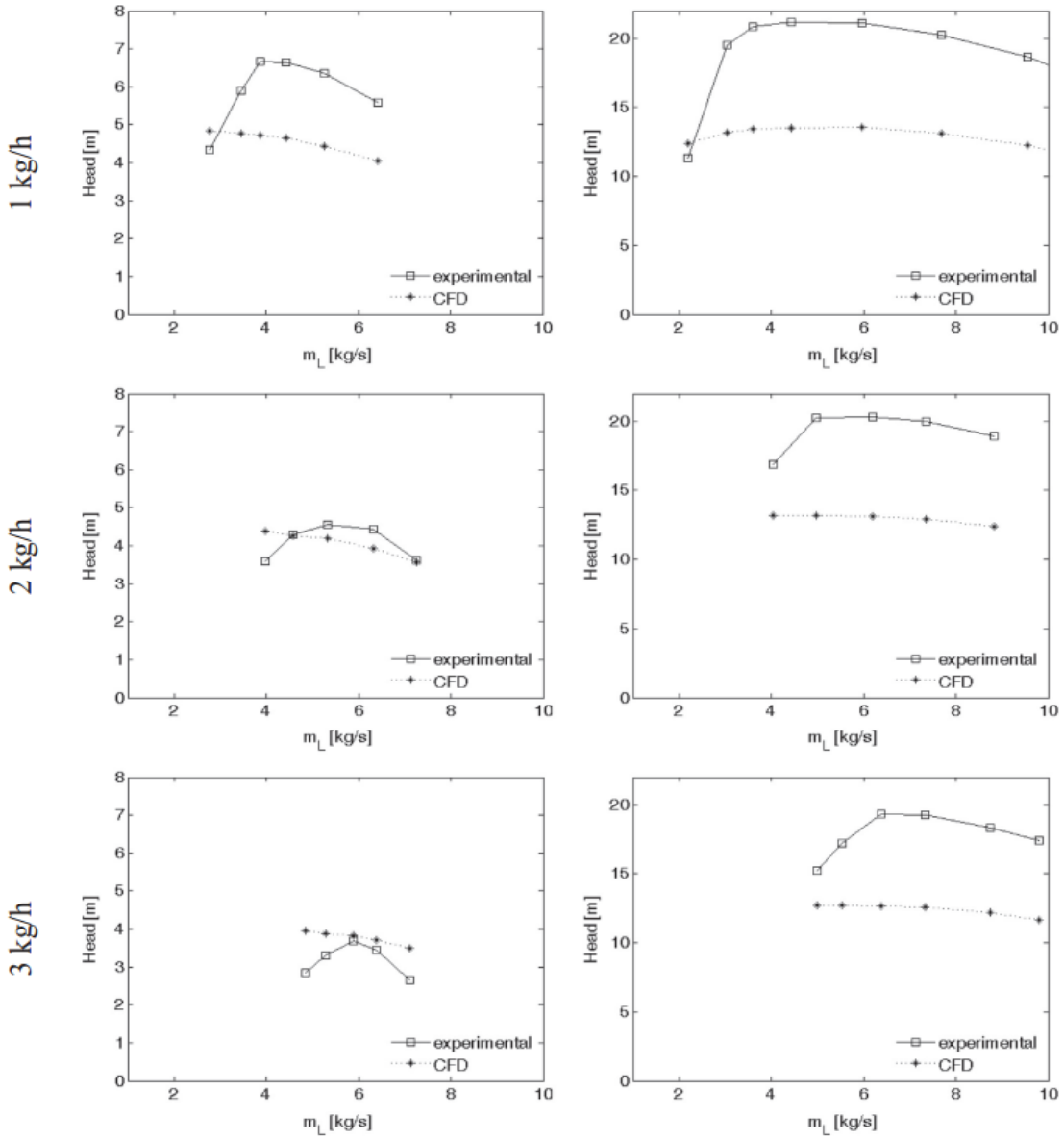

Figure 14. Head developed for the water–air mixtures at 100 kPa (Pineda, H. *et al*. 2016)

Although the simulation above shows an error over 25% with a significant deviation from the experiment under low pressure and low volume flow rate condition, it is still valuable. The authors made the conclusion that the VOF model is not able to capture accurately the bubbles coalescence and breakup in the impeller, and that an improvement in this matter will be needed to enhance the head prediction. They also

take the rotation speed into consideration. From their conclusion, the mean value of the void fraction increases at higher gas flow rates and lower pressures. The rotating speed does not presents an influence in the void fraction mean value, but it increases the variation of the void fraction as a function of time. This means that at higher rotating speeds there are more gas pockets, and these pockets explain the higher head degradation at 3000 RPM.

1.1.3 Numerical simulations on ESP erosion prediction

Krüger, *et al.* (2010) performed multiphase simulations on a centrifugal pump. In this research the simulations are not only modeled with the original geometry, but also modeled with an eroded geometry obtained from 3D scan after erosion test. Fig.15 (a) shows the comparison of key parameters of their leading edge erosion prediction between original geometry and eroded geometry. Fig 15 (b) shows the six key parameters related with erosion prediction in each result, which are particle impingement angle, solid concentration, measured erosion depth, erosion factor(a parameter defined by author to predict erosion), water turbulence kinetic energy and location of the impeller. The result is good at the leading edge but not applicable at the trailing edge and tip clearance. The author mentioned that in the simulation of the eroded geometry particle impingement angle and solids concentration reached peak values along the eroded region of the leading edge. Simulation with the eroded geometry the erosion factor showed a qualitatively good agreement with the experiment. The author also concluded that CFD can help to predict erosion on a qualitative level, while a quantitative prediction of erosion remains impossible at this time.

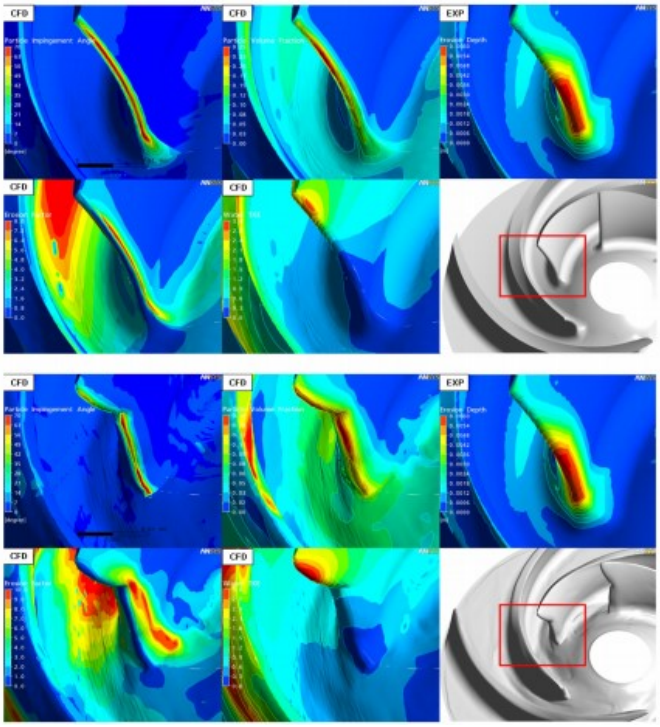

(a)

CFD Particle Impingement Angle [degree]	CFD Solids Concentration [-]	EXP Measured Erosion Depth [m]
CFD Erosion Factor [-]	CFD Water Turbulence Kinetic Energy [-]	Location of the impeller (enlargement)

(b)

Figure 15. (a) Key erosion parameters for initial(upper) and eroded (lower) impeller, focus on leading edge. (b) Structure of result visualization with selected key parameters (Krüger, *et al.* 2010)

Pagalthivarthi, *et al.*(2011) performed erosion prediction on a 2D centrifugal pump with ANSYS Fluent. This simulation was based on the Discrete Phase Model (DPM) and with this simulation they verified that the erosion will increase when rotation

speed increases or flow rate increases. The particle size effect was also studied in their research. Four mono-size slurries with particle sizes of 100 μm, 200 μm, 500 μm and 1000 μm, respectively, were studied to determine the effect on impact wear parameter along the casing wall. The author observed that larger particle diameter resulted in increased erosion prediction.

Pirouzpanah (2014) conducted a two phase simulation on particle laden flow in a mixed flow pump by applying the Eulerian-Granular scheme with ANSYS Fluent. The flow consists of the liquid phase-water and the granular phase-sand. Not only the main flow path is considered but also the balancing holes are simulated. Since the simulation did not cover the whole secondary path including the bearing clearance and stage clearance, the author assumed a small portion of the total flow is flowing backwards in to the balancing holes. Fig.16 shows the balancing holes and the mesh of the stage.

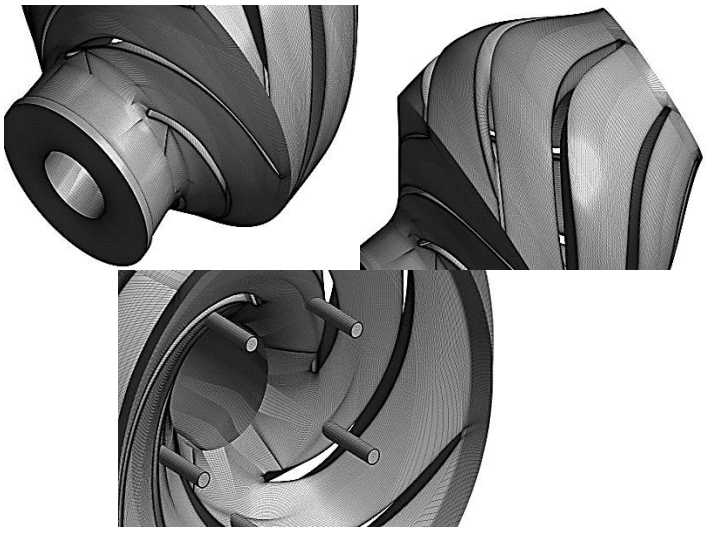

Figure 16. Mesh generated on single stage ESP-WJE1000 (Pirouzpanah 2014)

The author also developed a new erosion model based on sand fraction, near wall sand speed and liquid kinetic energy. (Note all input units are SI units except the erosion rate ER, which is um/hr.)

$$EF = (\alpha_s)^{0.08} \left(\frac{V_s}{V_{s_0}} \right)^{0.07} \left(\frac{k_w}{k_{w_0}} \right)^{1.25} \quad (1)$$

$$ER\ (\mu m / hr) = A.EF^2 + B.EF \quad (2)$$

$$A = 0.0163,\ B = 0.8774 \quad (3)$$

Applying the above erosion prediction model for his simulation, Pirouzpanah (2014) obtained a qualitatively well-matched result with the experiment, as shown in Fig.17.

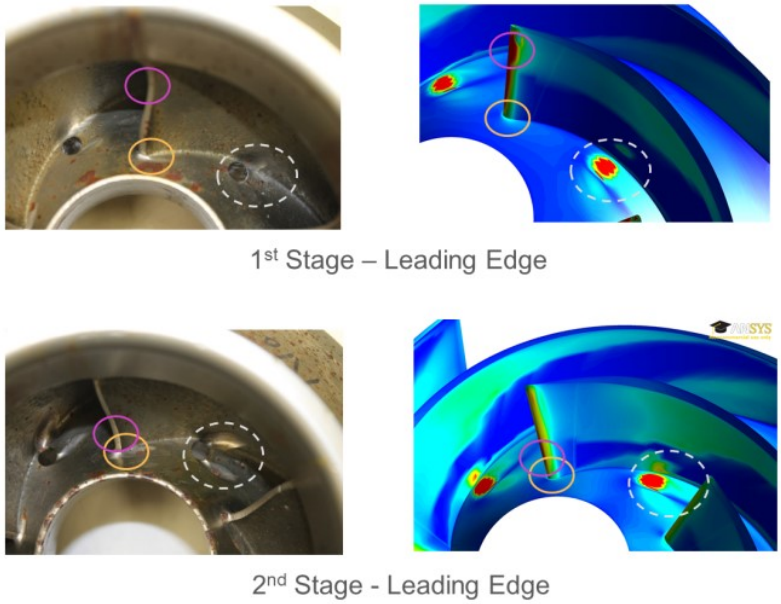

Figure 17. Comparison between the computed erosion rates with the eroded locations in the first and second impellers (Pirouzpanah 2014)

1.1.4 Summary

Experimental or numerical, most of the researchers concentrate their interest in the pump performance measure/prediction, head degradation analysis and the wear of the ESP. Little investigation has been made into the secondary flow path inside the ESP, which could affect the lifespan of the bearings and other parts inside the ESP. Many researchers have observed the abnormal head degradation in the first stage of the pump. The bubble size and gas volume distribution could be the reasons for this problem. The first stage is often the first to be eroded or detected with surging, thus a further investigation should be made on the first stage. As for the erosion prediction, more reliable simulation results are needed together with the support of experimental data to obtain a better prediction of the erosion. So far no universal model has been developed for the erosion prediction of ESP. Most progresses in the erosion simulation are qualitatively predictions.

2. OBJECTIVES

This research focuses on the numerical simulations of the split-vane ESP MVP-G400 with the commercial available software ANSYS Fluent. There are three main focuses in this research: the secondary flow path, the abnormal first stage pressure degradation and the erosion prediction.

The secondary flow path refers to the flow path formed by bearing clearances, stage clearances and balancing holes. The volume flow rate in the secondary flow path is much lower compared with the main flow stream, but the flow field is complicated with the backward flow and separation of different phases. The sand particles do cause severe erosion in the secondary flow path by either entering the bearing clearance or accumulating in some region with vortices, which can result in the pumps failure. Considering the difficulty of experimental methods to investigate the flow pattern in the secondary flow path, CFD is a good approach. This simulation should focus on multistage simulation with Eulerian multiphase flow.

From experiment results, the first stage of an ESP raises our interest. This stage often shows significantly higher pressure degradation compared with other stages when gas is added. It is also the stage where most surging and erosion is occurring. For this problem, an assumption is made that the changing of bubble size is a critical reason. Unlike other stages, the first stage inlet has a much lower turbulence level which allows bigger bubbles to exist. The injected bubbles could break-up and coalesce in the first stage, resulting gas pockets in the flow channel, which has been observed by other researchers' visualization. As a result, the multiphase simulation of the first stage should

include the ability to allow the bubbles to break-up and coalesce. The bubble size should be able to change instead of being a given size. After obtaining the simulation results with changing bubble sizes, the first stage pressure degradation and erosion can be explained.

With the proper numerical simulations, erosion predictions can be drawn based on multiple erosion models. Although it is hard to obtain quantitative erosion prediction due to the lack of calibration experiment for various materials, impact angles and sand particles, a qualitative illustration of the erosion zone can be obtained by simulation and data analysis. Since the simulations of sand particles are made with either the Eulerian approach or the Lagrangian approach, different erosion models should be applied and tested for the best result.

In summary, this research will use the numerical simulation approach to (1) analyze the flow field inside the ESP, (2) obtain the flow pattern inside the secondary flow path, (3) explain the abnormal flow phenomenon in the first stage and (4) predict the erosion of the stage qualitatively.

3. FUNDAMENTALS OF MVP-G400

MVP-G400 is a split-vane ESP manufactured by Baker Hughes. It can be used separately or connected to the inlet of other ESPs for better gas handling. The pump was tested by Steck, D.(2014) for performance and erosion in Dr. Morrison's lab at Texas A&M University.

3.1 The geometry of MVP-G400

A single stage in a G400 consists of one 6-blade impeller and one 7-vane diffuser. The impeller is shown in Fig.18 and Fig.19. Note this is a split-vane impeller, the blades was separated into one set of big blades and one set of small blades, in total there are 12 blades in the impeller. The split-vane design helps to prevent the occurrence of gas lock in the impeller when GVF is high.

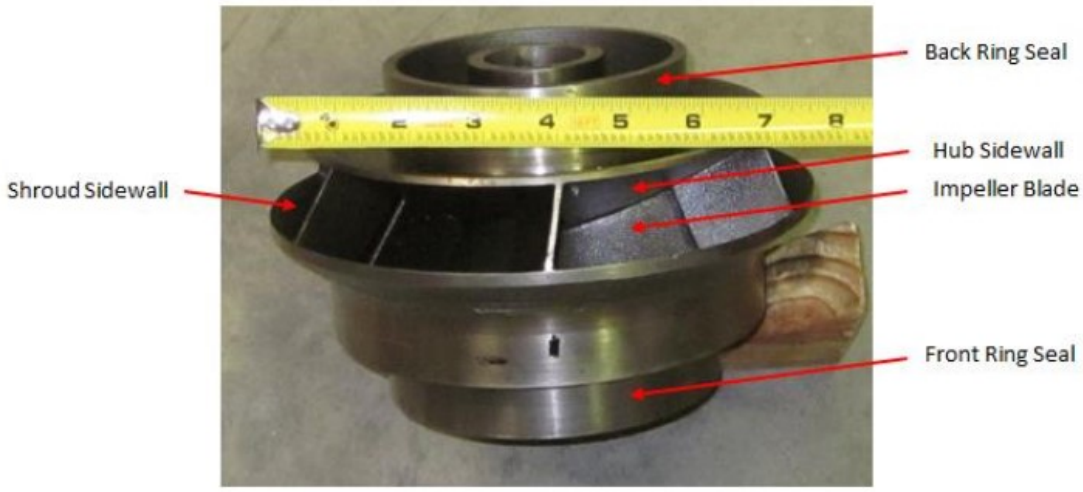

Figure 18. G400 impeller overall view (Steck, D. 2014)

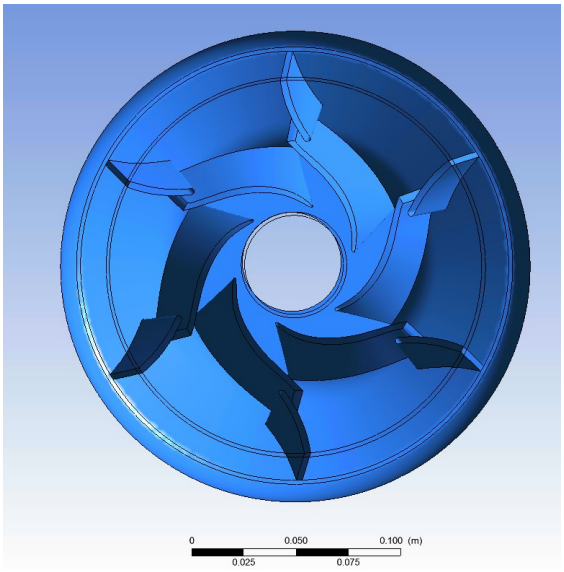

Figure 19. Two sets of blades in the G400 impeller (computation model)

Fig.20 shows the overall view of the diffuser and Fig.21 shows the computation model of the vanes inside the diffuser.

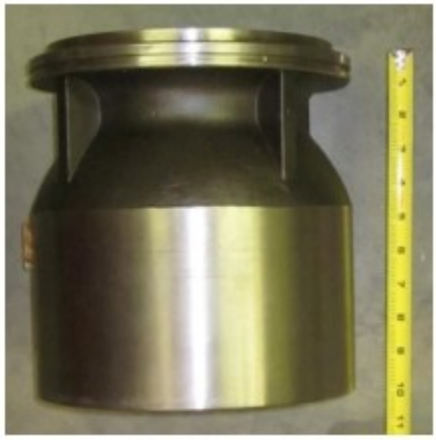

Figure 20. G400 diffuser overall view (Steck, D. 2014)

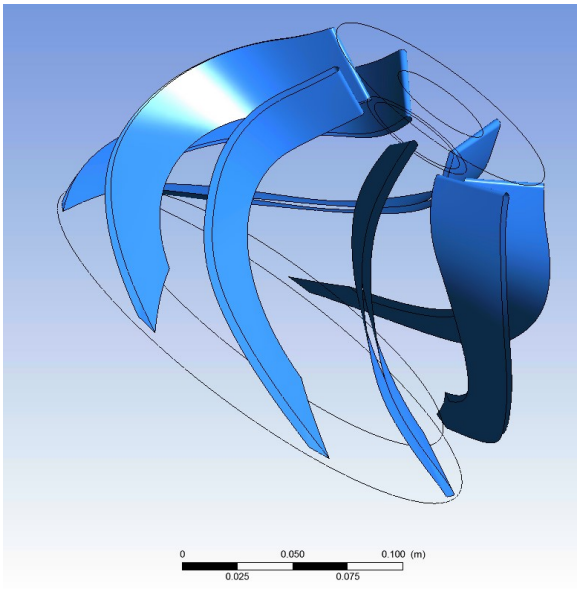

Figure 21. Vanes inside the diffuser of G400 (computation model)

3.2 Inner flow path

The main operating flow path in a single stage is shown in Fig 22. The multiphase flow enters the pump and raises its pressure by a combined work of centrifugal force and impeller motion, just like other mixed flow pumps.

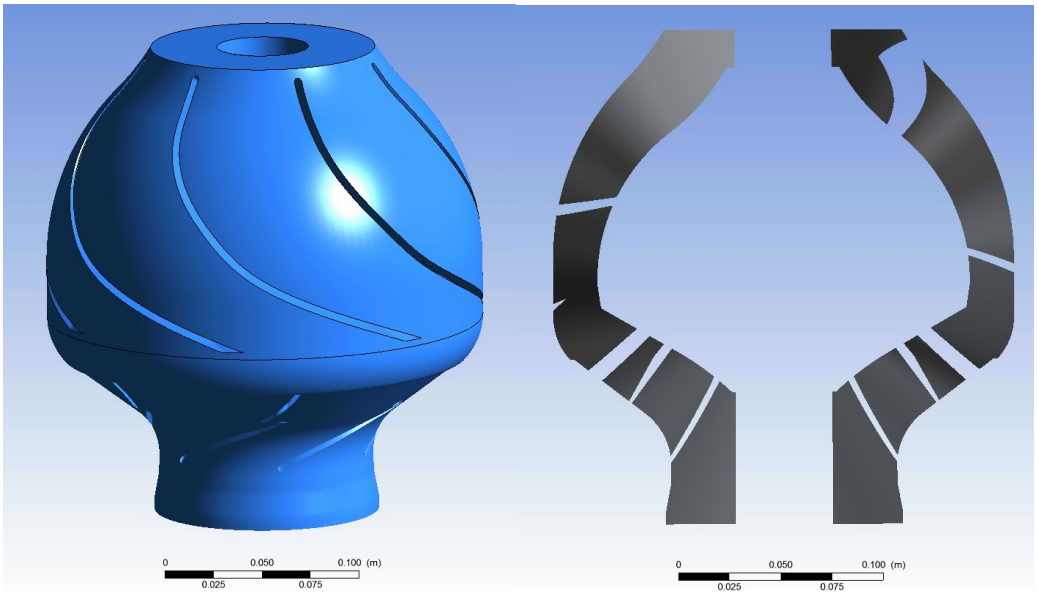

Figure 22. G400 main flow path (Left) with sectional view (Right)

In real operation of the ESP, the clearance between bearings and shaft, the clearance between impeller and diffuser, the clearance between stages due to installment and the balancing holes together creates a complicated secondary flow path, resulting in the backward flow and erosion of bearings. Fig. 23 shows the assembled two stages section view together with the section view of the flow path inside.

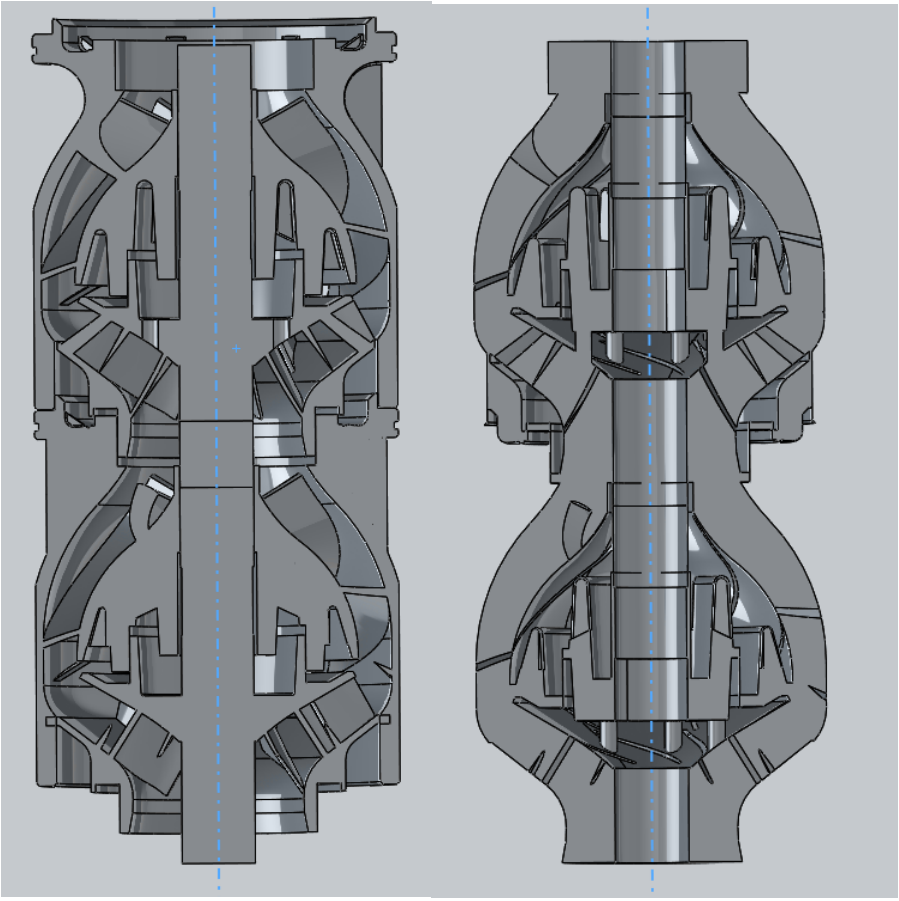

Figure 23. Section view of the assembled two-stage ESP with shaft (Left) and Section view of its flow path (Left)

3.3 Operating condition from previous experiment

The tests were finished by Steck, D. and Chen, Y in 2014. In total there were three erosion tests conducted with this ESP for inlet GVF of 0%, 10% and 20%. The first test was performed with water and sand only. The second and third tests added air as the gas phase into the pump. All three tests' inlet total flow rate were at the best efficient point (BEP) of this pump. The pump inlet pressure was maintained at 40 psig. All tests were conducted to a sand concentration of 0.2% (by weight), which is higher than the

operating environment in the oil industry to accelerate the erosion process. (Steck, D. 2014)

For all simulations in this thesis, the operating condition and boundary conditions are kept the same as the experiment in order to make a better comparison of the results.

4. METHODOLOGY

4.1 Mesh generation and independence study

Most simulations in this research are run with the ANSYS Fluent 17.1, except that some of the main flow path mesh was generated by STAR-CCM+ for convenience. Both software are commercially available. The meshes generated are shown in Fig.24 and Fig.25.

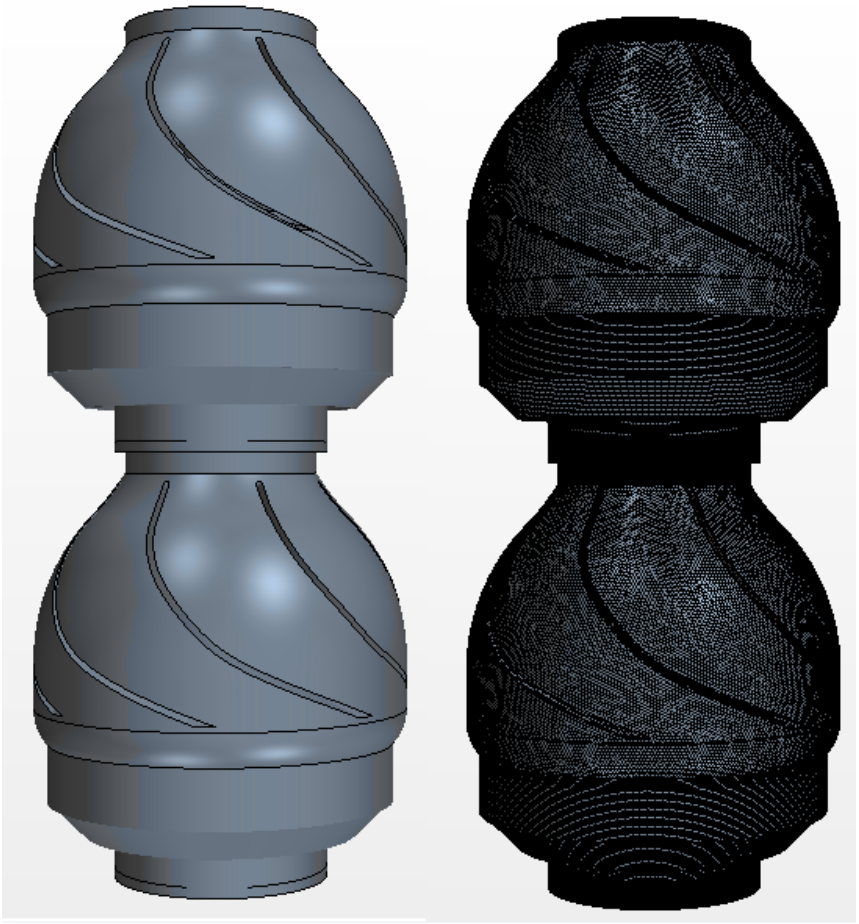

Figure 24. View of the mixing mesh generated for the simulation of secondary path

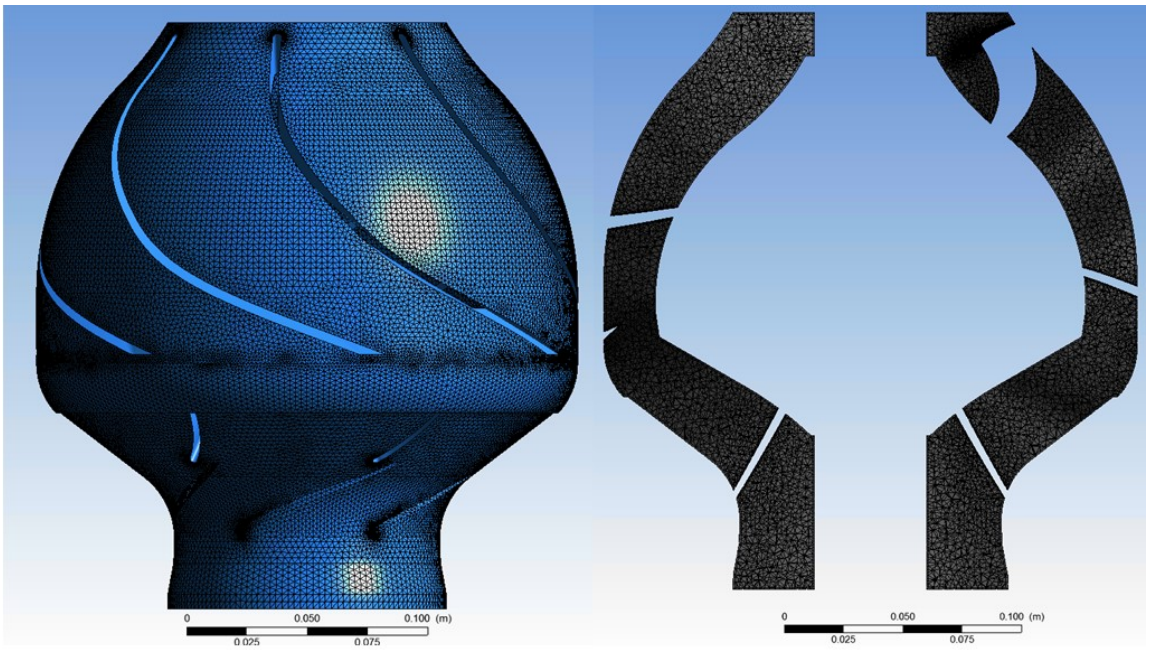

Figure 25. Unstructured mesh in the main flow path

The mesh in Fig.24 is used for the three phase simulation of secondary flow path. The mesh in Fig.25 is used for bubble size analyze with Population Balancing Module (PBM) and erosion prediction.

The mesh independence was tested with the main flow path for one set of impeller and diffuser. The simulation's environment is based on the 2nd stage in the 0% GVF test. This simulation setting is 3D transient realizable k- ε model with standard wall function, with a mass-flow inlet and a pressure outlet. The outlet is kept at 216 psig while the inlet has the incoming mass flow of water at the rate of 67.2 kg/s. After the impeller's rotation exceeds 10 rounds at a 3600rpm, the flow has become fully developed turbulence and the inlet pressure is stable. Three sets of unstructured mesh are tested in this part. The original one has over 2 million tetrahedral cells in the impeller

and over 1 million tetrahedral cells in the diffuser. The 2nd mesh increases cell number by 30% and the 3rd mesh increases cell number by 50%. The results are shown in Table 1. The pressure difference due to mesh size is less than 0.2%, thus the original mesh is suitable for this simulation.

Table 1. Mesh Independence study

Mesh Independence Study	Impeller cells Num.	Diffuser cells Num.	Avg. inlet pressure
Mesh1(original mesh)	2,701,059	1,855,383	124.85 psig
Mesh2(130% mesh)	3,244,057	2,299,713	124.95 psig
Mesh3(150% mesh)	3,611,301	2,568,074	124.97 psig

4.2 Simulation settings for secondary flow path

This simulation is a two-stage transient simulation. The realizable k-ε model with standard wall function is also applied here. With the requirement of 3D, transient, water-air-sand multiphase flow and dual stages, the simulation consumes much more CPU time than the single phase simulation. Moving mesh is applied here as well. The Eulerian Multiphase model is used with the per-phase interaction for turbulent setting. Temperature is fixed at 318K, which was the working condition during the test. Air is compressible, but its density is only affected by local pressure since there is no temperature change. The bubble diameter is fixed at 0.1 mm. The sand particles are treated as a granular phase with granular viscosity, radical distribution and solid pressure defined by Syamlal-Obrien method (ANSYS Fluent Manual, 2016). The sand particle

has a diameter of 0.08mm and maximum packing limit of 0.63. The phase interaction between the sand and the water is defined by the Syamlal-Obrien method, which is suitable for granular particle flow. Other phase interactions are defined by the default Schiller-Naumann Method. This simulation is a second order simulation for a better result. The time step size is set to 2.3E-5s, which means the impeller rotates 0.5 degree each time step.

All the boundary conditions are obtained from the G400 test with 20% GVF at the inlet as shown in Table 2.

Table 2. Boundary condition for dual stage simulation with secondary flow path

Pressure at outlet	Mass flow inlet-water	Mass flow inlet-air	Mass flow inlet-sand
231psig	64.7kg/s	0.06 kg/s	0.1 kg/s

4.3 First stage simulation with Population Balancing Module (PBM)

This simulation is a two-phase simulation focusing on the prediction of the abnormal pressure degradation in the first stage of the ESP. Most settings related to the water and air phases are the same as that in the previous three phase simulation. The only difference is that the diameter of bubbles are not limited to a fixed value, instead it is defined with the help of the Population Balancing Module (PBM) as a discrete set within a certain range.

Referring to ANSYS Fluent PBM manual (2013), the PBM provides multiple methods for definition of bubble diameter. Here we use the discrete method for the bubble breaking-up and coalescence. This method defines the secondary phase as a

discrete list of bins with different sizes. In this module, a general transport equation for bin fraction is applied with mass conservation for the closure of the problem. The bubbles diameter defined by this method is not continuous, which is not the case in reality, thus defining the diameter with a larger range and more bins will improve the results. Considering a balance between better results and simulation time, we chose the bins as shown in Table 3.

Table 3. Calculated bubble diameter distribution with PBM

Bin Number	Bin Size (m)
Bin-0	0.019200001
Bin-1	0.012095243
Bin-2	0.007619525
Bin-3	0.0048
Bin-4	0.003023811
Bin-5	0.001904881
Bin-6	0.0012
Bin-7	0.000755953
Bin-8	0.00047622
Bin-9	0.0003

4.4 Prediction of erosion and a possible method for calibration

The erosion prediction is always a challenging task in the numerical simulation of multiphase flow. Since the particle could be treated either as an Eulerian granular phase or a discrete particle phase, different simulation settings and erosion prediction methods are used in this prediction.

For the simulation with the Eulerian granular phase, we can apply the erosion model (Eq. 1) developed by Pirouzpanah (2014), which relates the erosion with sand volume fraction, turbulence kinetic energy and sand near wall velocity.

As for the discrete phase method, the erosion module from ANSYS is applied for the prediction of erosion. According to the ANSYS Fluent Manual (2016), the erosion rate can be calculated by the following equation,

$$ER = \sum_{p=1}^{N_{particles}} \frac{\dot{m}_p \, C(d_p) f(\alpha) v^{b(v)}}{A_{face}} \tag{4}$$

where $C(d_p)$ is a function of particle diameter, α is the impact angle of the particle path with the wall face, $f(\alpha)$ is a function of impact angle, v is the relative particle velocity, $b(v)$ is a function of relative particle velocity, and A_{face} is the area of the cell face at the wall. Note that C, f, and b are defined as boundary conditions at a wall, rather than properties of a material, so the default values are not updated to reflect the actual materials being used.

The general form of the erosion function is

$$ER = Cv^b f(\alpha) \tag{5}$$

Where C and b could be either function or constants.

For example,

The Tulsa Angle Dependent Model:

$$ER = 1.559e^{-6}B^{-0.59}F_s v^{1.73} f(\alpha) \tag{6}$$

$$1.559e^{-6}B^{-0.59}F_s = C \tag{7}$$

$$v^{1.73} = v^b \tag{8}$$

Where ER is the erosion ratio (mass of surface eroded per mass of particles impinging), B is the Brinell hardness, and F_s is a particle shape coefficient.

$$f(\alpha) = \begin{cases} 0 + 22.7\alpha - 38.4\alpha^2 & \alpha \le 0.267 rad \\ 2 + 6.80\alpha - 7.5\alpha^2 + 2.25\alpha^3 & \alpha > 0.267 rad \end{cases} \tag{9}$$

(ANSYS Fluent Manual 2016)

With the erosion data obtained from previous experiment (Steck, D. 2014 and Chen, Y. 2017), it is possible to use the following algorithm to calibrate the input parameter.

Note in our erosion test, the surface hardness and particle shape factor are constants. So when applying the Tulsa Angle Dependent Equation, we can consider C and b are constants.

Eq. (5) divided by material density ρ_m.

$$\frac{ER}{\rho_m} = \frac{C}{\rho_m} v^b f(\alpha) A \tag{10}$$

$$\log\left(\frac{ER}{\rho_m}\right) = \log\left(\frac{C}{\rho_m} v^b f(\alpha)\right) = \log C - \log \rho_m + \log f(\alpha) + b \log v + \log A \tag{11}$$

where $\frac{ER}{\rho_m}$ can be recognized as the eroded thickness.

Now we have one set of erosion data from an experiment, including the eroded surface thickness.

Set D_m as the measured eroded thickness, D_{s1} as the eroded thickness from simulation result with the input parameter C_s and b_1, D_{s2} as the eroded thickness from another simulation result with the input parameter C_s and b_2, we have the following equations: (supposing D_m can be calculated with the correct C and b).

$$\log D_m = \log C - \log \rho_m + \log f(\alpha) + b \log v \tag{12}$$

$$\log D_{s1} = = \log C_s - \log \rho_m + \log f(\alpha) + b_1 \log v \tag{13}$$

$$\log D_{s2} = = \log C_s - \log \rho_m + \log f(\alpha) + b_2 \log v \tag{14}$$

Note at every point on the surface, $f(\alpha)$ and $\log v$ should be the same.

Then we have

$$\log(D_m / D_{s2}) = \log(C / C_s) + (b - b_2) \log v \tag{15}$$

$$\log(D_{s1} / D_{s2}) = (b_1 - b_2) \log v \tag{16}$$

By removing $\log v$ we have,

$$\frac{\log(D_m / D_{s2}) - \log(C / C_s)}{\log(D_{s1} / D_{s2})} = \frac{b - b_2}{b_1 - b_2} \tag{17}$$

$$\log(D_m / D_{s2}) = \frac{b - b_2}{b_1 - b_2} \log(D_{s1} / D_{s2}) + \log(C / C_s) \tag{18}$$

The above equation is valid at every single point, and the only unknown in this equation is b and C, which are parameters we need to calibrate.

After picking up a few points on the eroded surface, we can use the linear regression method to get the slope, interception point and correlation of $\log\left(D / D_{s2}\right)$ and $\log\left(D_{s1} / D_{s2}\right)$.

5. TWO-STAGE SIMULATION WITH SECONDARY FLOW PATH

The first part this research focuses on the two stage simulation with all secondary flow paths within the flow field. Here the secondary flow paths refer to the clearance between bearings and shaft, the clearance between impeller and diffuser, the clearance between stages due to installation requirement and the balancing hole. All these secondary flow paths together form the backflow path and contribute to the head degradation and erosion of bearings.

All simulations in this part of research used ANSYS Fluent 17.1. The simulations are based on moving mesh, transient 3-D, $k-\varepsilon$ turbulence with Eulerian multiphase enabled. The Eulerian multiphase method is set to be per phase for better accuracy. Gravity is considered as well. The two stages are meshed together and no periodic mesh is applied.

To better compare with experiment results, the boundary conditions and operation conditions are set the same with the G400 erosion test with 20% GVF at first inlet. There are three stages assembled vertically with three phases inside – water, air and sand. The simulation is performed on the second and third stages with all paths. The first stage is different due to inhomogeneous of bubble sizes and other effects, which will be discussed in next chapter. In this simulation, the bubble size is fixed at 0.1mm and the air is considered compressible due to pressure change. Temperature is fixed at 320K. The outlet is set to be pressure outlet at 231 psig and the inlet is set to be mass flow inlet. The impeller is rotating at 3600rpm. The expected inlet pressure from

experiment is 61.0 psig, the result from simulation is 67.1 psig. The predicted head rise for the two stages has an error 3.58% compared with the experiment.

5.1 Flow field inside the duo stages with secondary path

The section view of the main flow path and secondary flow path is shown in Fig. 26.

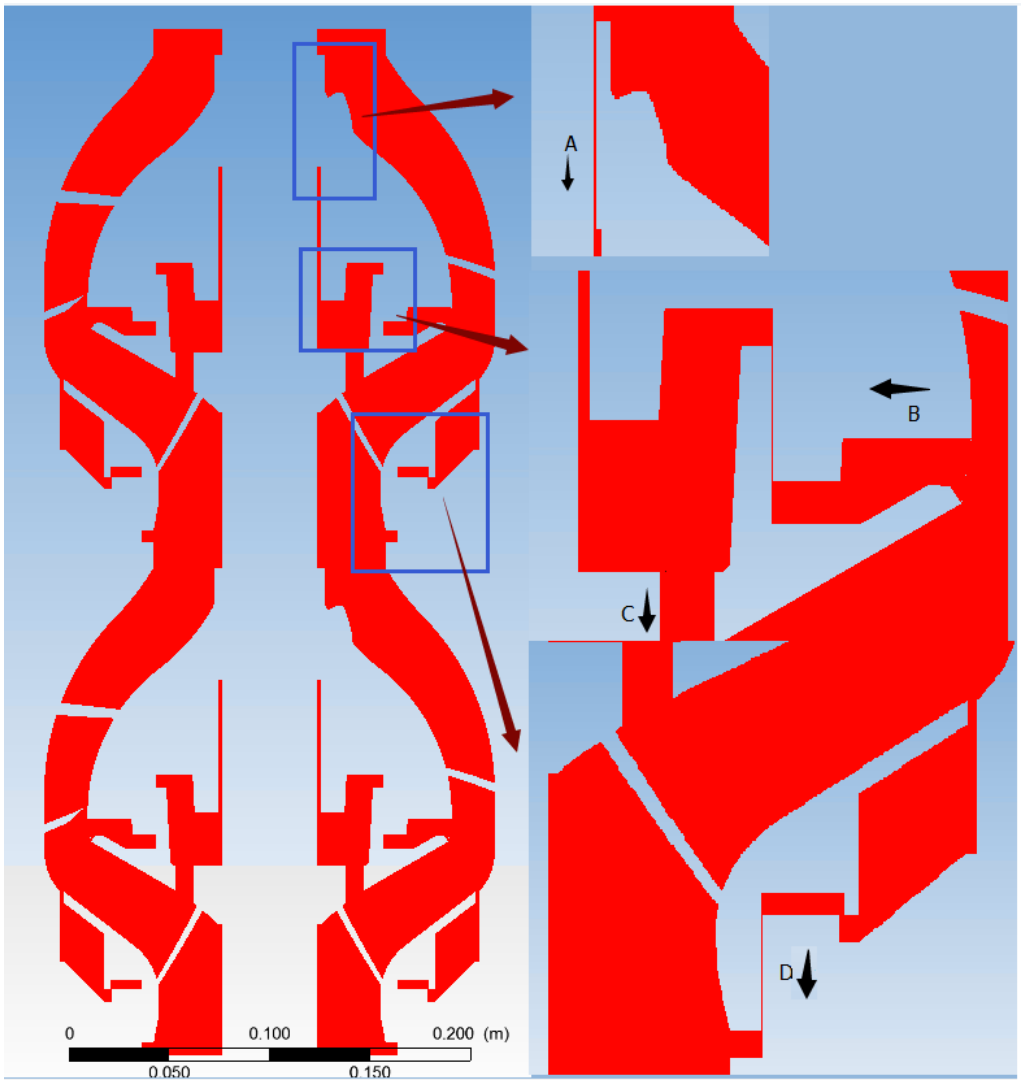

Figure 26. Section view of flow path and secondary flow paths

The secondary flow paths consist of four parts, which are bearing-shaft clearance (Fig.26.A), impeller-diffuser clearance (Fig.26.B), balancing holes (Fig.26 C), and cross stage impeller-diffuser clearance (Fig.26 D). The black arrows in Fig.26 show the direction of the water in the multiphase flow in these secondary flow paths.

The velocity magnitude distribution for all phases on the section view is shown in Fig. 27. In the main flow path, all three phases are moving at similar speeds. The bubble size for the air phase is fixed at 0.1mm, so the speed of bubbles are easily affected by the main phase due to the drag force due to the large area of interaction surface. As for the sand phase, the volume fraction of sand is very small compared with other two phases, and in the Eulerian simulation the sand is set as a continuous granular phase instead of individual particles. Thus, the interactions between particles are ignored and sand in the main phase is flowing with water almost at the same speed.

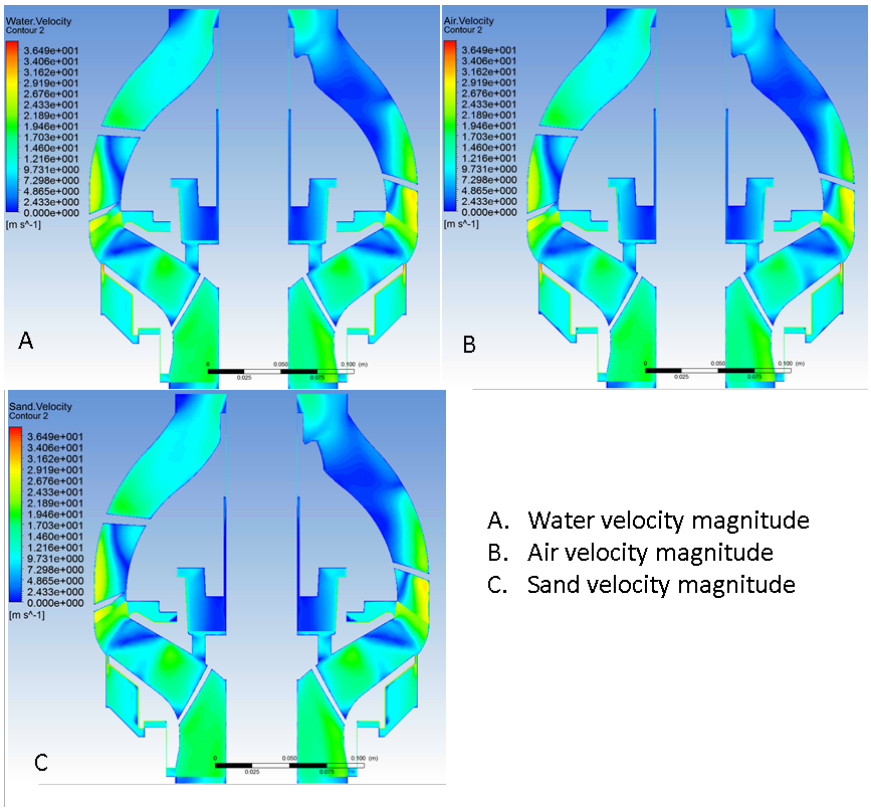

Figure 27. Velocity magnitude distribution on the section plane.

When it comes to the secondary flow paths, the story is different. There are no rotating blades forcing the flow to move upwards. The rotating of smooth impeller surfaces adds to the circumferential velocity but does not contribute to the mass flow rate of the secondary flow as much as the pressure difference. The pressure difference drives the flow backwards at a lower speed compared with the main phase. Inside the secondary paths, the combined effect from pressure difference, density difference, viscosity difference and rotation of impeller walls results in two phenomena: the reverse of secondary phases' mass flux in backward flow and the separation of phases. The details of these two phenomena are shown and discussed in 5.3.

5.2 Mass flow rate of each phase in secondary flow path

After obtaining all data from the simulation, the mass flow rate of each phase in each path is calculated in Table 4. All the positive directions of the paths are defined as the water flow directions, the same as the black arrows in Fig. 26.

Table 4. Mass flow rate of each phase in secondary flow path

Mass Flow Rate[kg/s]	Total	Water	%	Air	%	Sand	%
Total	6.49E+01	6.47E+01		6.03E-02		1.00E-01	
Bearing Clearance	2.42E-01	2.41E-01	0.37%	5.54E-04	0.92%	1.77E-04	0.18%
imp-diff(same stage)	7.23E-01	7.20E-01	1.11%	3.53E-03	5.85%	-1.05E-03	-1.05%
Balancing holes	1.12E+00	1.11E+00	1.72%	1.61E-03	2.68%	6.47E-04	0.64%
diff-Imp-diff(cross stage)	1.44308	1.44137	2.23%	-6.39E-04	-1.06%	2.35E-03	2.34%

From Table 4, the percentage of mass flow for all phases in secondary flow paths are significantly small than main phase flow, which is reasonable. There are around 1% of gas and 0.2% of sand in the bearing clearance. Although this amount is relatively small comparing with the main flow rate, these backwards mixture flows could cause severe erosion on the clearance surface since the thinnest part of this clearance is just 6 mils. In addition, the air phase and sand phase are not always flowing in the same direction as the water phase, which could be caused by gravity and centrifugal force. The different directions of phases in the secondary flow path shows there could be some vortices and backwards flows creating the separation of phases, which could also contribute to the erosion process.

The mass flow is calculated by integration on the interface of each connection surface of secondary paths. The means the positive direction could be just the direction where most of the flow passes. Even on the same interface, the flow direction could be different due to vortices.

5.3 Streamlines and vortices

Fig.28 and Fig.29 show the 3D streamline of water in the whole field and in a single impeller. Fig 30-31 show the 2D streamline of each phase on the cross section plane.

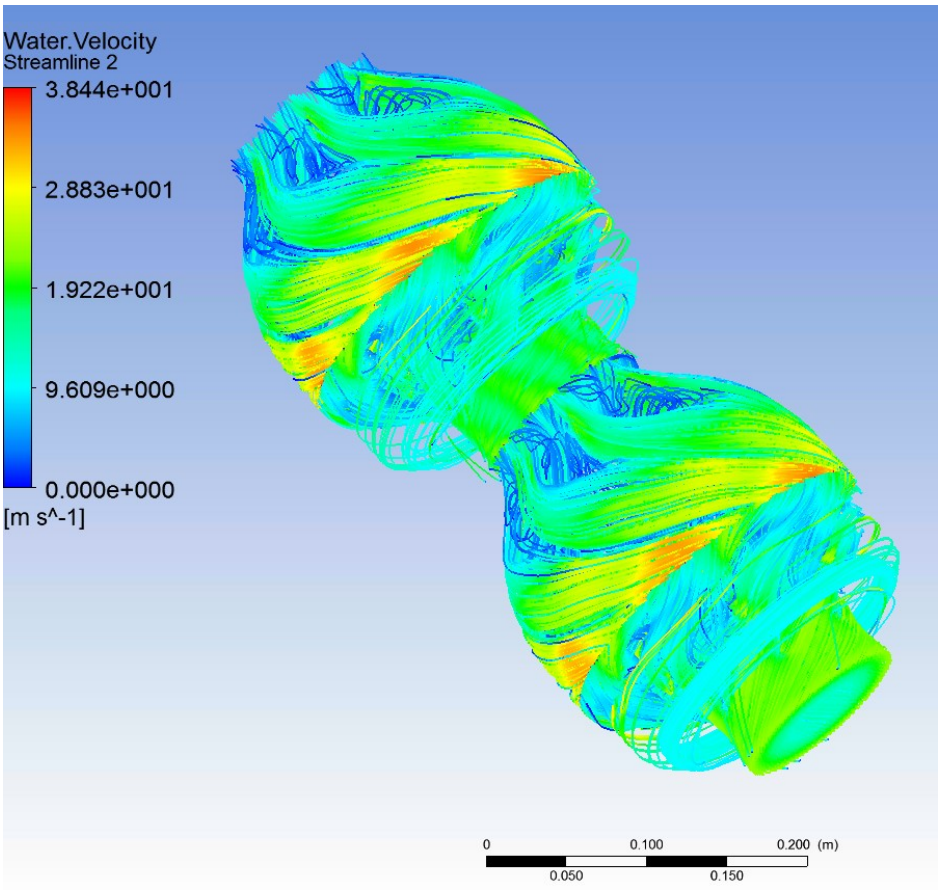

Figure 28. Water streamlines in the whole flow field

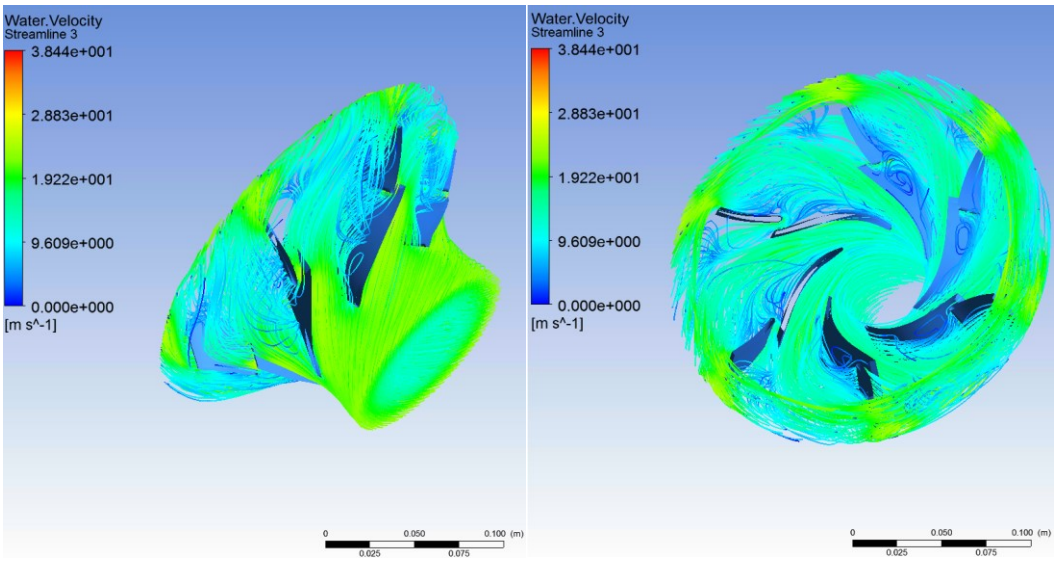

Figure 29. Water streamlines in a single impeller with blades

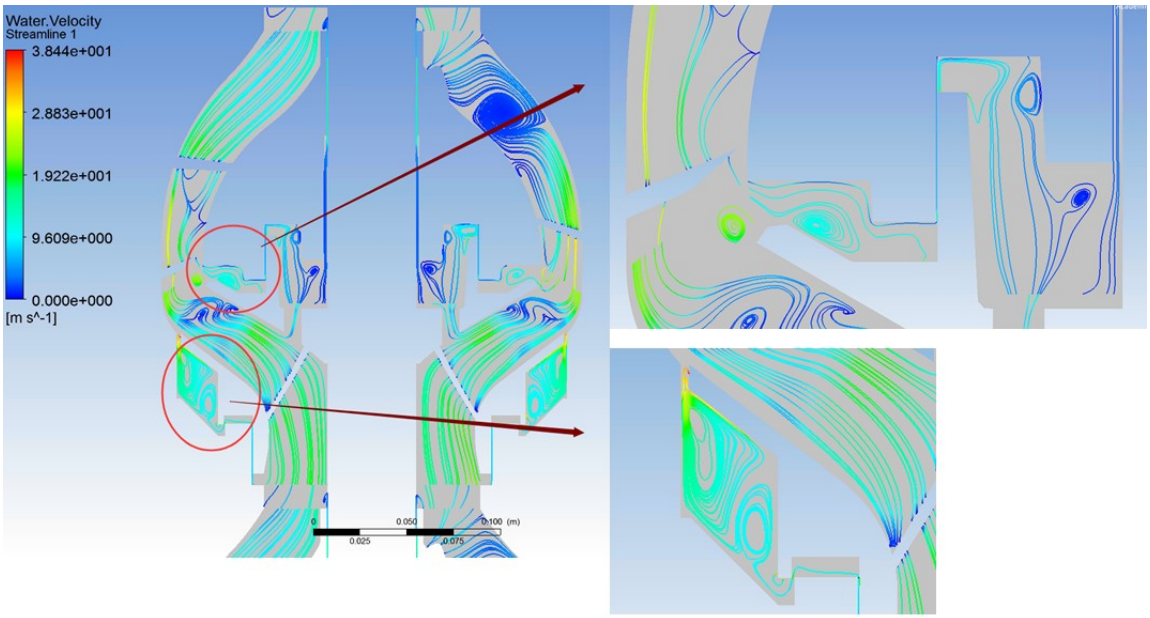

Figure 30. Water streamlines on the cross-section plane.

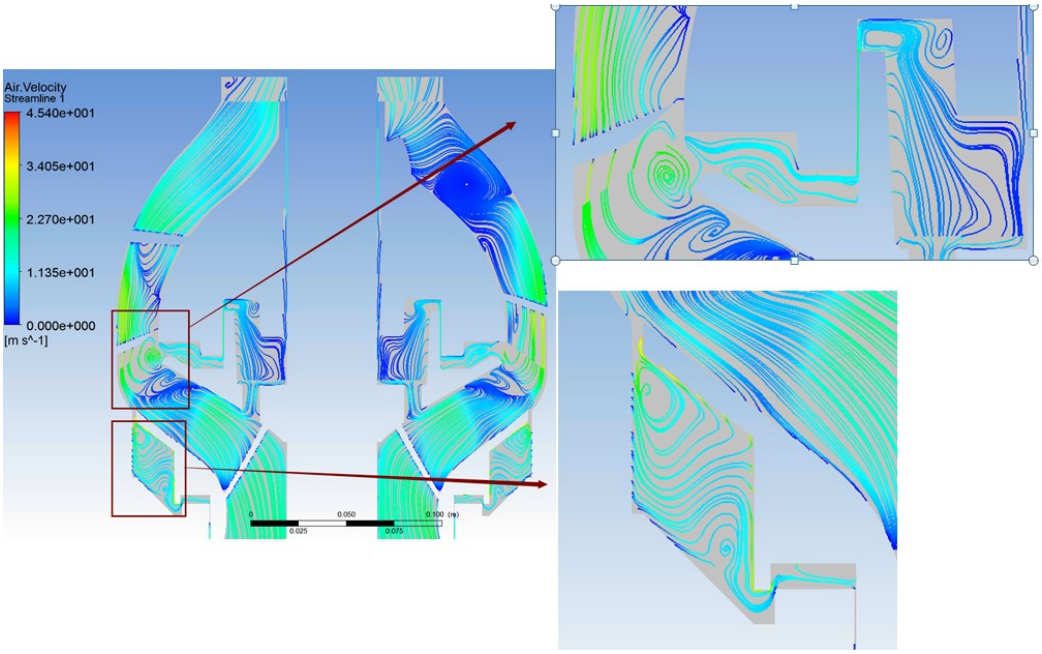

Figure 31. Air streamlines on the cross-section plane.

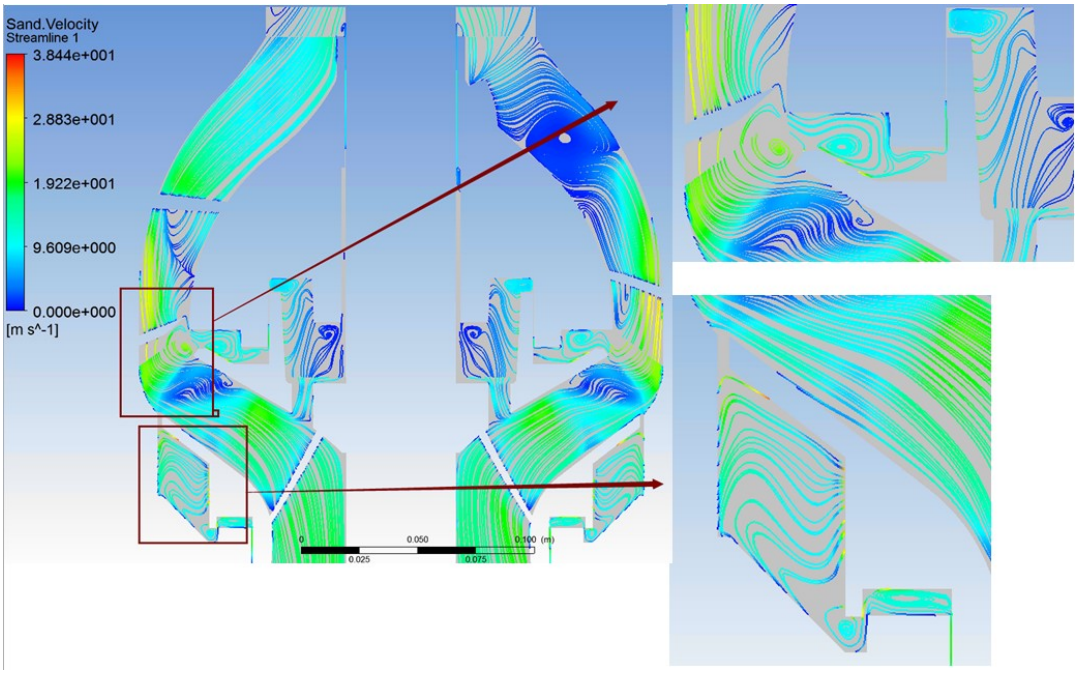

Figure 32. Sand streamlines on the cross-section plane.

From the 2D streamlines shown in Fig.30-32, the streamlines of different phases show similar patterns in the main flow path. The positions of the vortices cores are similar. However the detailed patterns inside the secondary flow path are different.

Due to density and viscosity difference, each phase has its own vortex pattern in the secondary flow path, leading to the separation of phases. Fig. 33 shows the separation of phases in the clearance between stages.

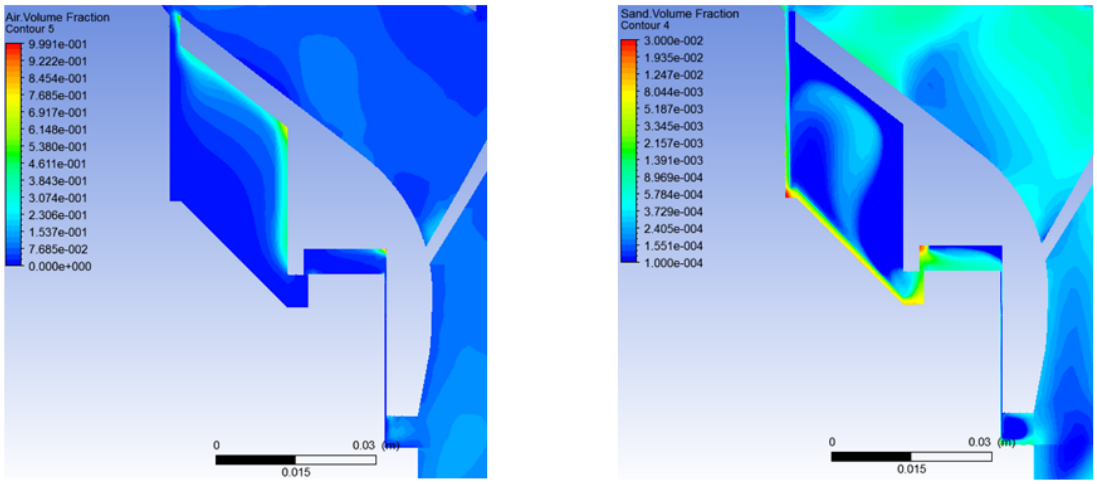

Figure 33. Separation of phases detected between stages

Fig. 34 shows the streamlines of each phase in the stage-to-stage clearance. The background is colored by z-direction velocity v_w. Red when the flow is going upwards, blue when going downwards, and green when v_w is relatively small. At the interface of the clearance, the combination of pressure difference and rotation of impeller walls creates strong vortices. The flow is going up and down at different places on the same interface. When the phases have an inhomogeneous distribution, the flow pattern of each phase is different. In Fig. 34, the upper interface of the secondary flow path has all

phases going in and out. The main flow is going downwards driven by pressure difference. Due to gravity effect, the bubbles in the air phase float up and generate more mass flow in the z+ direction. This explains the negative mass flow rate of air in Table 4.

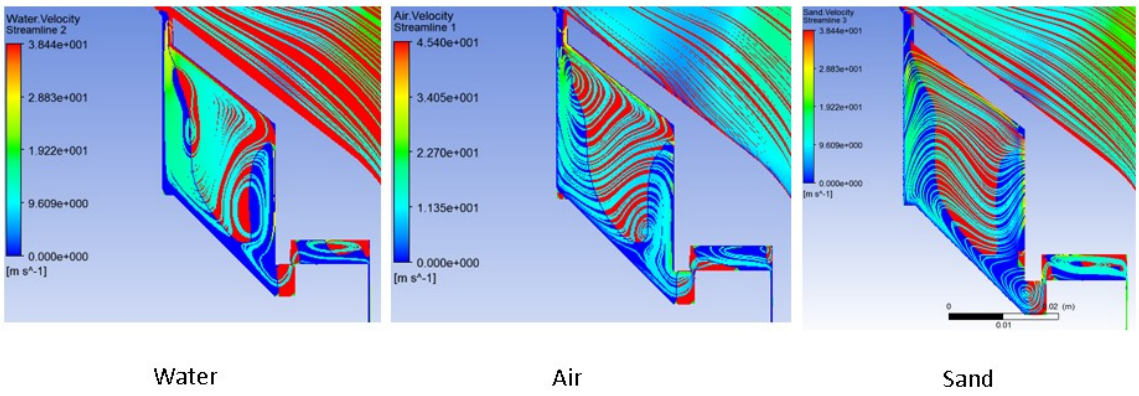

Figure 34. Water, air and sand streamlines inside the stage-to-stage clearance

Similar things happen in the secondary flow path between the impeller and diffuser in the same stage. Fig. 35 shows the streamlines of each phase in the stage-to-stage clearance. The background is colored by radial direction velocity v_r. Background is red when the flow is going in the positive radial direction, is blue when going negative direction, and is green when v_r is relatively small. Refer to Table 4, the sand phase also has negative mass flow rate in this clearance, which is driven by centrifugal force.

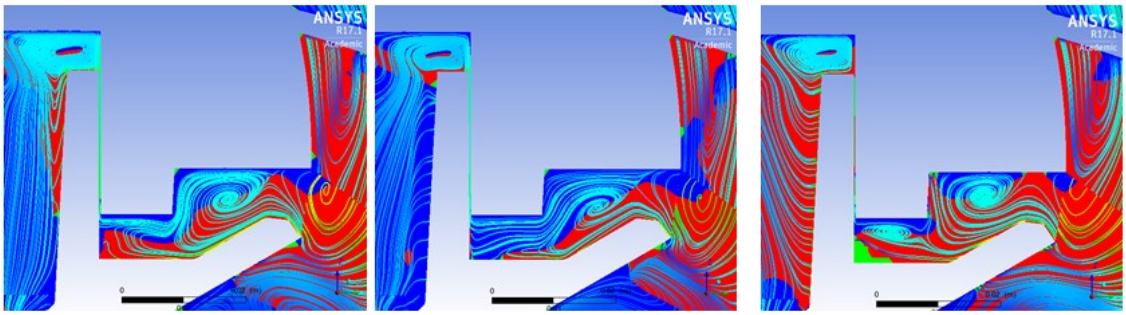

Figure 35. Water, air and sand streamlines inside the imp-diff secondary flow path

5.4 Pressure distribution

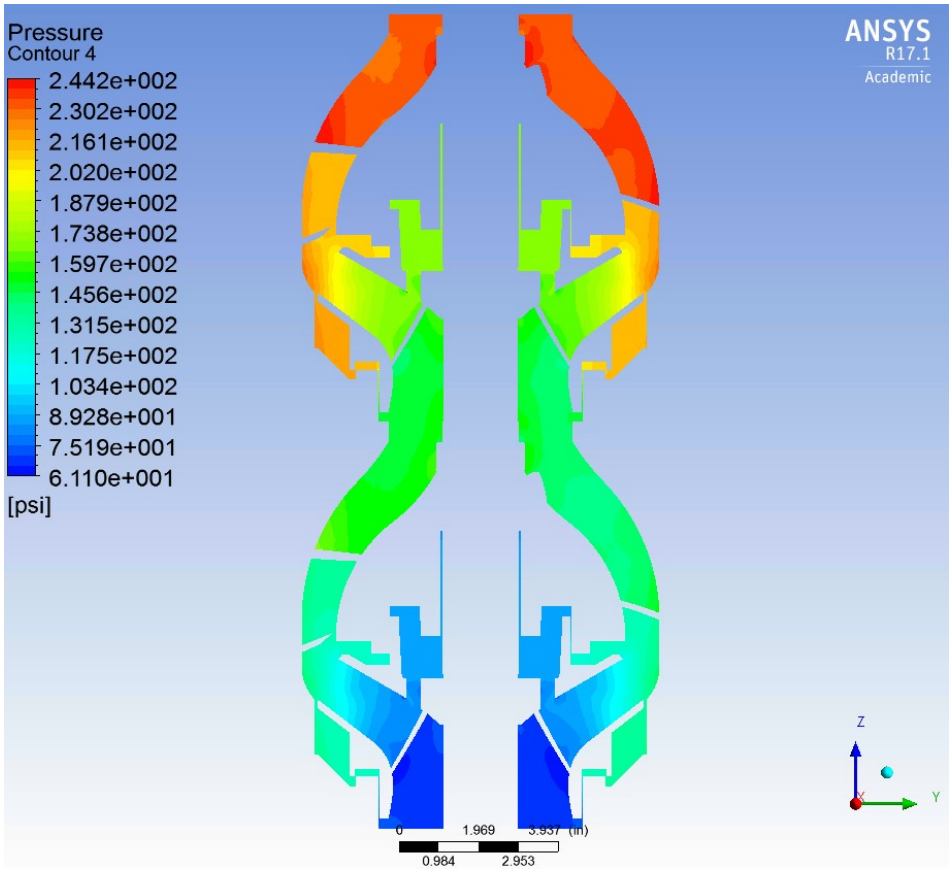

Figure 36. Pressure distribution on section plane.

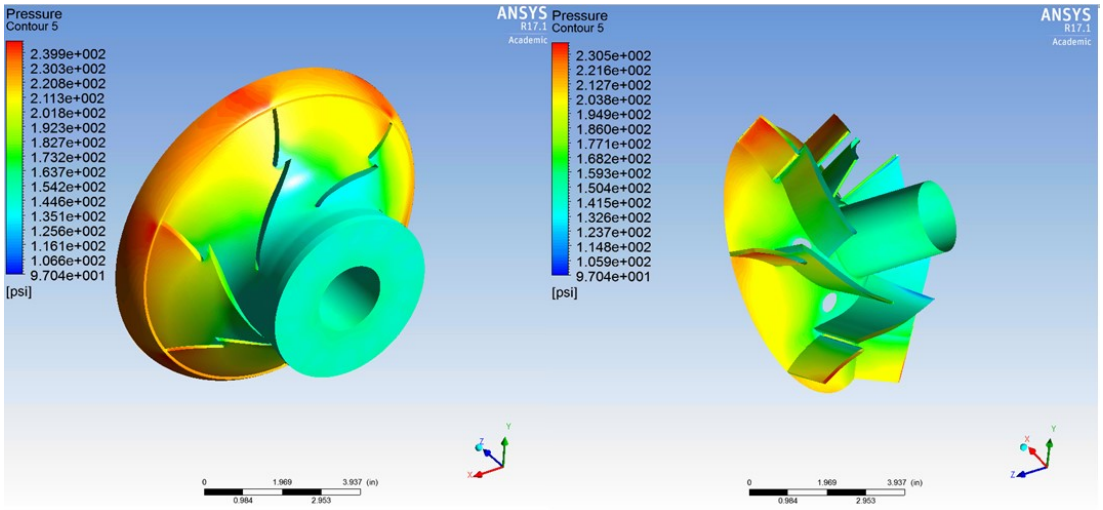

Figure 37. Pressure distribution on impeller surfaces and blades (Upper impeller)

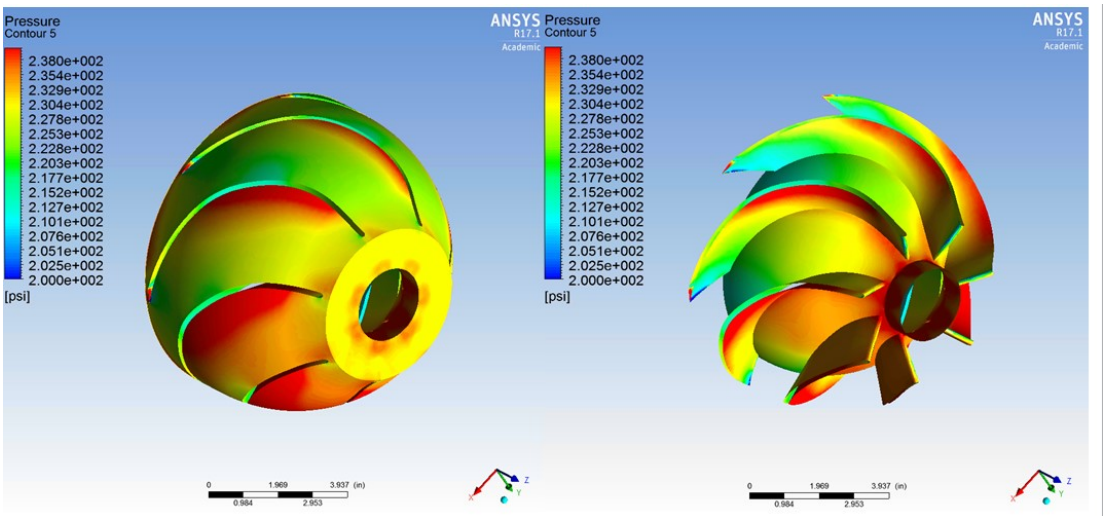

Figure 38. Pressure distribution on diffuser surfaces and blades. (Upper diffuser)

Fig. 39(a) shows the pressure difference in the upper and lower ends of the balancing holes, which drives about 1.7% of the flow backwards. The pressure difference in Fig. 39(b) between stages drives 2% of flow backwards. These backward

flows contribute significantly to head loss, but not significant enough for the head degradation observed in high GVF test conditions.

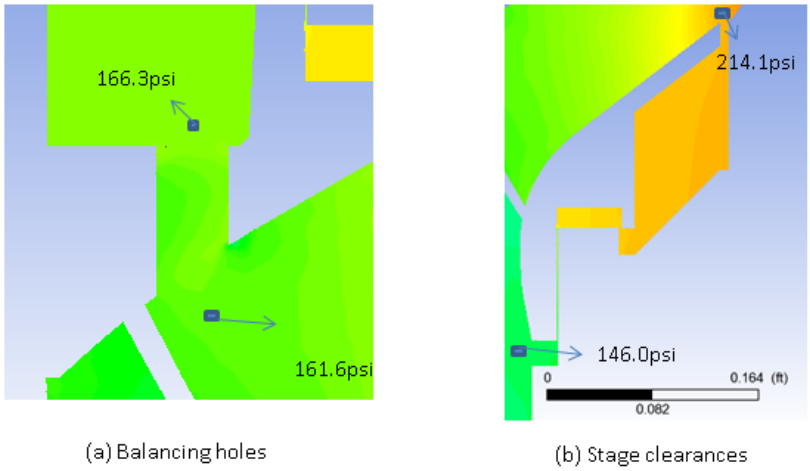

Figure 39. Pressure difference in balancing holes and stage clearance

This split-vane ESP generates pressure both by centrifugal force and the movement of the impeller. The impeller's blades push the flow from the inlet at a designed angle, adding kinetic energy and increasing centrifugal force. Pressure is then generated as the flow slows down. The blades, shrouds and hubs regulate and redirect the flow upwards with high resistance, generating the high pressure rise inside the ESP. In Fig. 37 and Fig. 38, the pressure side of the blades is regulating the flow and generating high pressure along the blades. The secondary flow paths reduce the pressure rise by allowing the flow to leak backwards. The split-vane design helps to increase pressure rise by adding resistance, but also increases the radial thrust. The purpose of the split-vane design is not to increase efficiency, but enable the pump to work with high GVF flows by preventing gas locks near the impeller blades.

5.5 Air volume fraction distribution

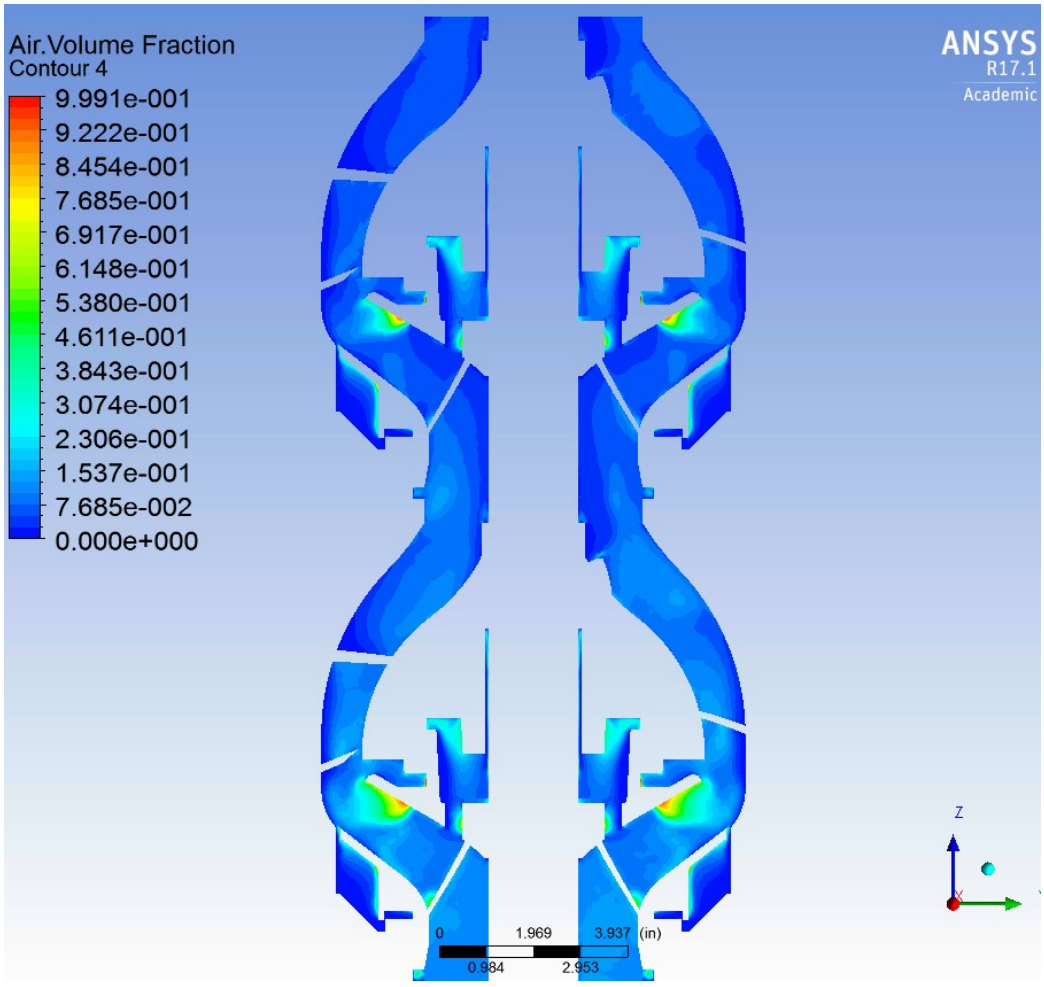

Figure 40. Air volume fraction in section view.

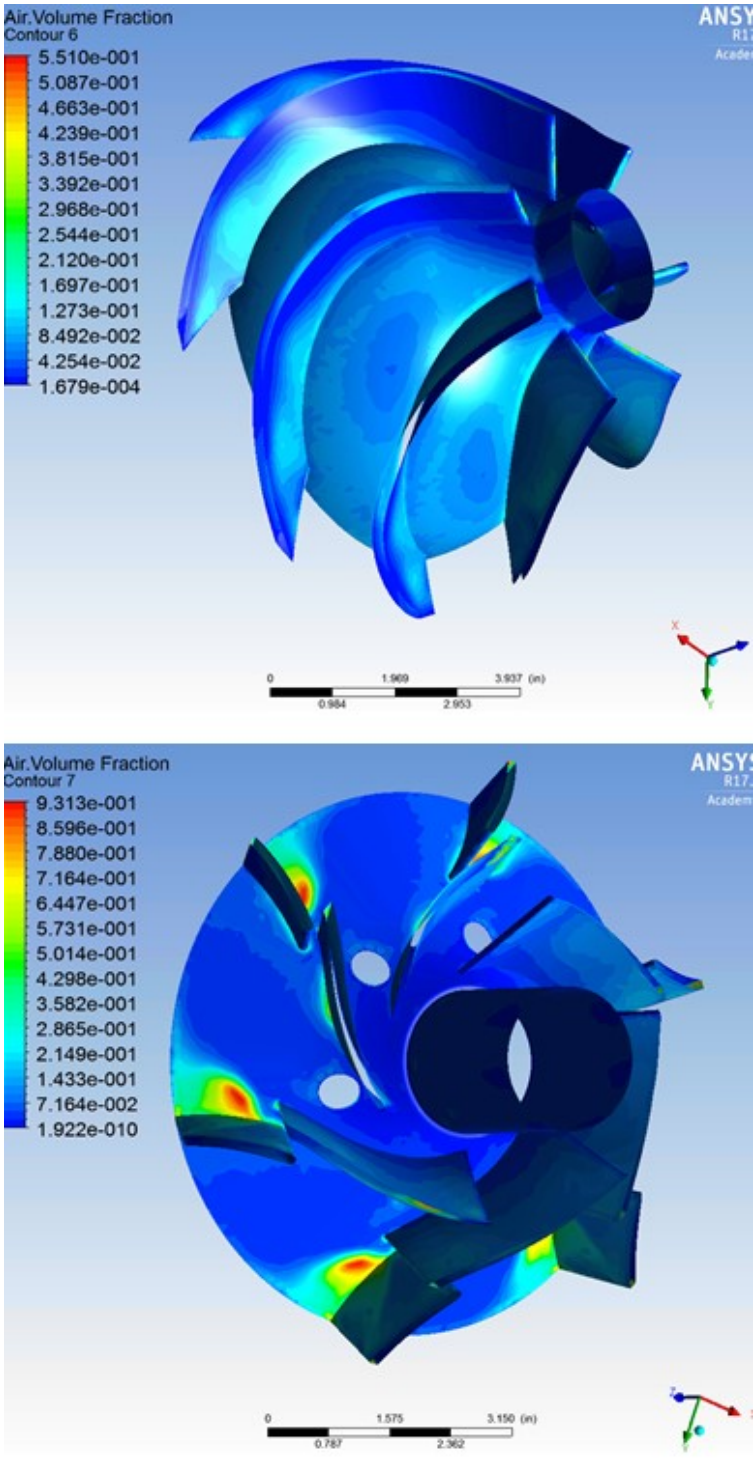

Figure 41. Air volume fraction near wall distribution (A. diffuser hub and blades; B. impeller hub and blades @ distance 0.005in)

The air volume faction distribution in Fig.41 is acquired at a distance of 0.005 in offset from the wall. Near the exiting blades of the impeller high gas volume fraction zones are observed on their suction sides. Since the bubble size is fixed at 0.1 mm, the high gas volume zones are still filled with water volume instead of being isolated by gas locks. The streamlines in Fig. 42(a) seems to indicate the existence of large isolated air zones, but when increasing seeding points for the streamline post processing, the water still occupies these zones in Fig. 42(b). The fixed bubble size simulation cannot detect real gas locks without water inside.

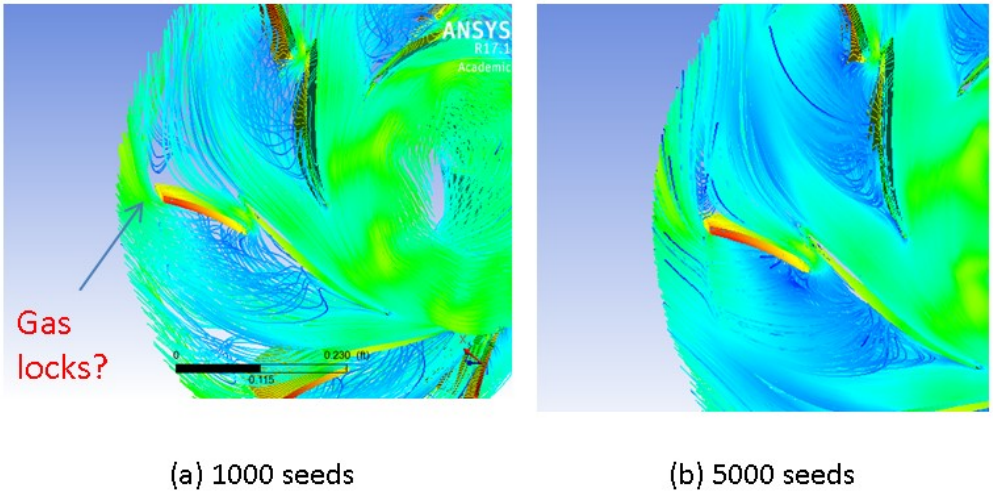

Figure 42. Gas accumulation with fixed bubble at diameter of 0.1 mm

The accumulation of air is created by the separation of water and air after hitting the exiting blades. After passing the leading edge, pressure drag from an adverse pressure gradient forces the air to slow down and accumulate on the suction side. The water has a density much higher than air and tends to keep its direction after passing the

leading edge. Thus, the separation of flow is occurred as shown in Fig. 43. On the larger blades the adverse pressure difference is not strong enough, so no separation is detected.

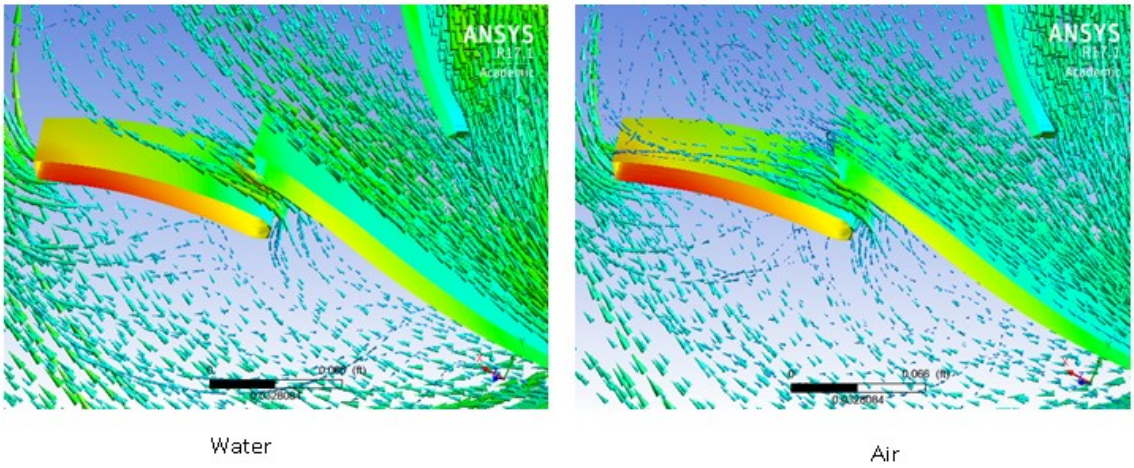

Figure 43. Water and air 3D streamlines near the impeller blades.

5.6 Sand volume fraction distribution

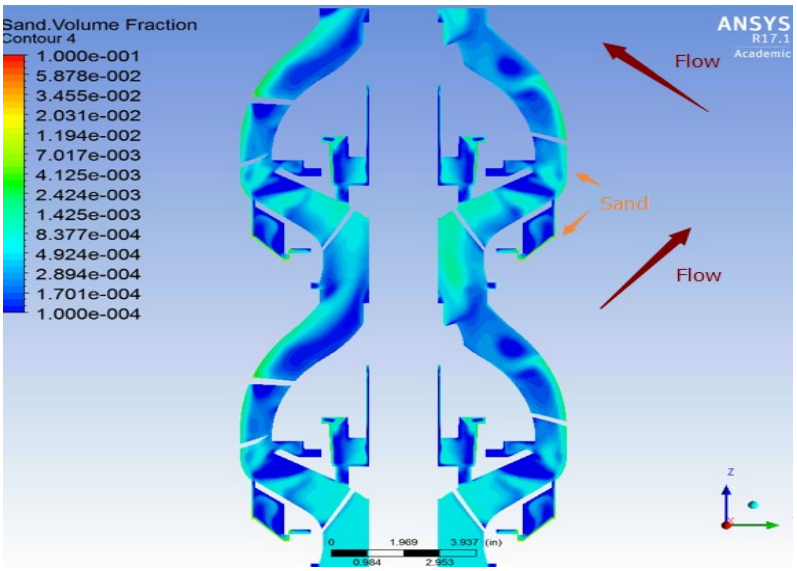

Figure 44. Sand volume fraction in section view

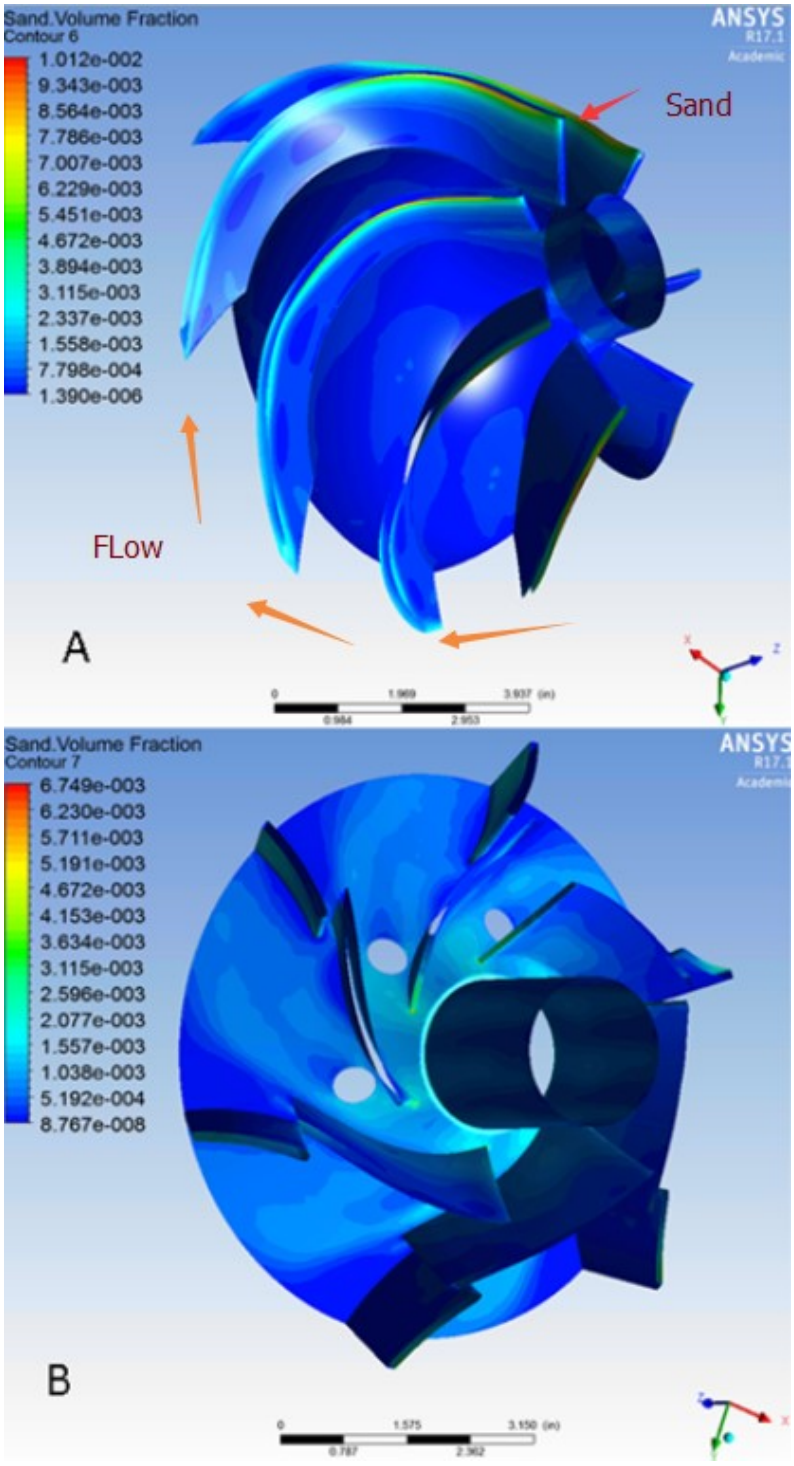

Figure 45. Sand volume fraction near wall distribution (A. diffuser hub and blades; B. impeller hub and blades @ distance 0.005in)

From Fig. 44 and Fig. 45, high sand volume concentration is detected on the leading edge of the impeller blades and the pressure side of the diffuser blades near the shroud. This concentration is a result of the sand's high density and centrifugal force. In the main flow path, the velocity of flow is high and gravity has a limited effect. In the secondary phase, the sand concentration is affected by centrifugal force and gravity, as is shown in Fig. 46. The high sand concentration on diffuser blades near the outlet in Fig. 45 (a) is driven by vortices in the diffuser near the outlet. On the pressure side of the diffuser blades, an adverse pressure gradient also exists (refer to Fig. 38). As shown in Fig. 47, this adverse gradient reduces the speed of the flow and generates vortices, forming air concentration zones and pushing sands to the top edge.

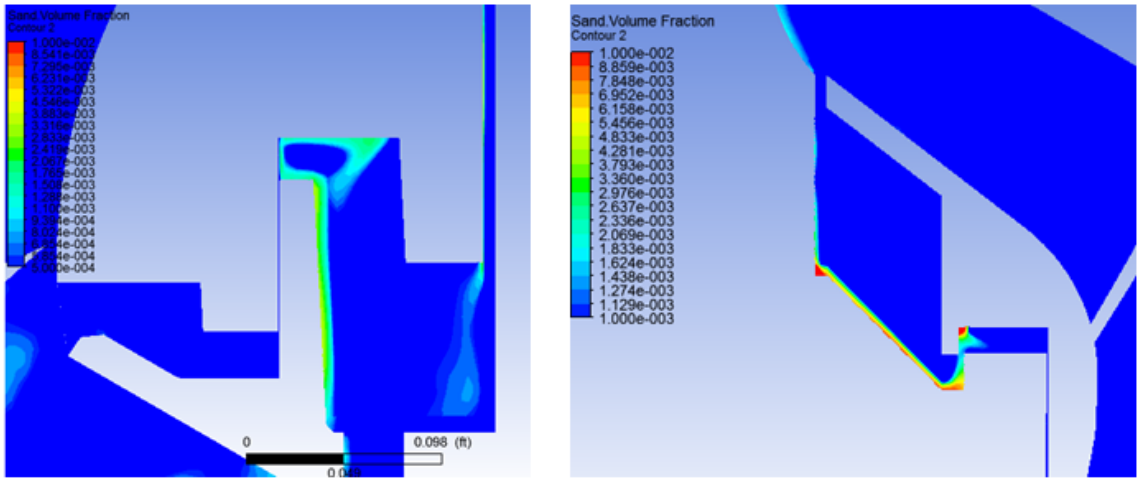

Figure 46. Sand concentration in secondary flow path.

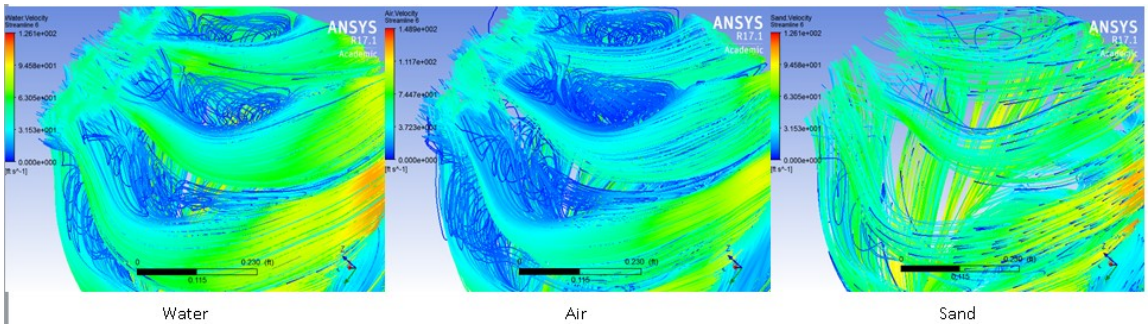

Figure 47. 3D streamlines showing vortices near the pressure out let.

5.7 Erosion prediction with Eulerian model

The detailed discussion of erosion prediction and erosion models is in Chapter 7. The simulations in this chapter are all Eulerian multiphase flow simulations, where the sand phase is considered as granular instead of discrete particles. Only Eulerian erosion models can predict the erosion zones for these simulations. Applying the Eulerian model from Sahand Pirouzpanah(2014), a qualitative prediction is obtained.

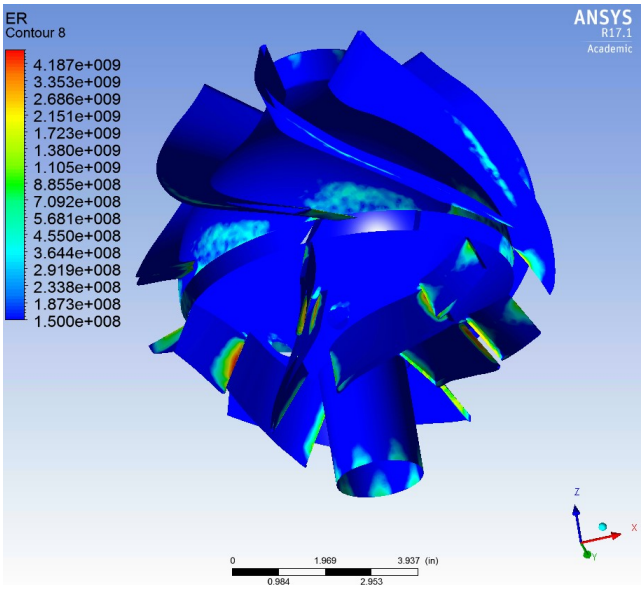

Figure 48. Erosion zone predicted on blades and hub.

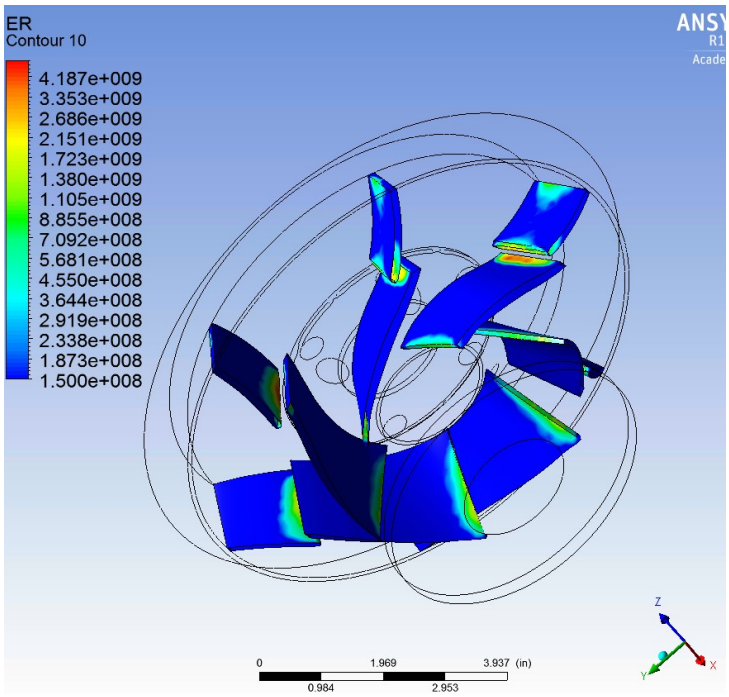

Figure 49. Erosion zone predicted on impeller leading and exiting blades

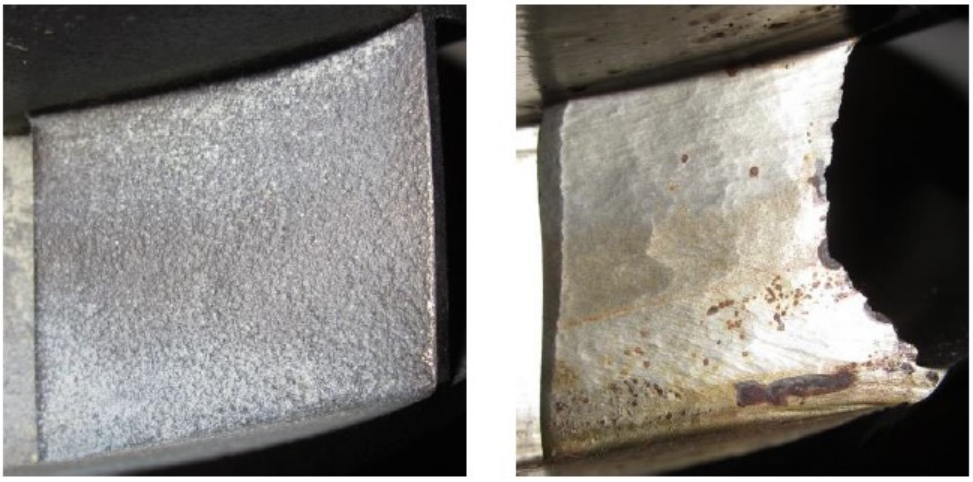

Figure 50. Eroded 2nd impeller exiting blades before and after 66 hours of test (Steck, 2014).

Figure 51. General view of 2nd diffuser and impeller before and after test (Steck, 2014).

An Eulerian multiphase flow simulation cannot detect the attack angle of particles on surfaces and does not provide impact particle data. This method still provides reasonable qualitative predicted erosion.

There are some interesting results comparing with experimental data. Based on Fig. 50 from experiment, the erosion on exiting blades of impeller is most severe. In Fig. 49, the erosion is predicted on the leading edge and the pressure side near the trailing edge. The predicted zones match with the experiment, including triangle zone in after erosion. But the test results show more erosion happened than predicted. A possible

reason is that the predicted erosion rate is for the initial geometry. As the erosion process progresses, the geometry will change and the erosion rate will be different, resulting in some inaccuracy of a prediction. Also, the erosion predicted on the diffuser blades' leading edge in Fig. 48 is only half of the edge's length, the mostly eroded part is at the middle of the edge. The test result in Fig.51 supports this prediction. By comparing the photo of original diffuser (upper left) and eroded diffuser (lower left), there is a curve on the diffuser blades' edge after the erosion test. It is possible the curve is created by erosion from the middle edge in the beginning.

The erosion predicted here is mainly abrasive erosion, since the sand phase in the Eulerian simulation is flowing along the surface. For the impact erosion prediction, please refer to Chapter 7 for more information.

5.8 Summary

This two stage simulation shows the inner flow field of all flow paths and provides a prediction of head rise 3.6% lower than experiment result. The second flow path allows about 1%~2% of the total flow to go backwards, resulting in some head loss and erosion in the clearances, which will cause bearing and pump failure. Due to density and viscosity differences, not all phases flow in the same direction in the secondary flow paths resulting in separation of phases and trapped vortices in some zones. Gas concentrations are also observed on the suction side of the impeller exiting blades. The adverse pressure gradient on the impeller exiting blades and diffuser blades generates vortices and separation of flow. The prediction of erosion in this section is limited to an

Eulerian model only, further impact erosion prediction quires other simulations with different models.

6. SIMULATION WITH CHANGING BUBBLE SIZE

For most of the simulations in the study of ESPs without the first stage, the bubble size is kept constant and the results are acceptable. When the first stage is simulated under the same condition with other stages, the result often shows significant deviation from the experiment. This error raises our interest in the first stage simulation, and suggests further investigation and new methods are needed for better accuracy.

6.1 First stage head loss

Table 5 shows the pressure rise in performance tests for G400 with 0% GVF, 10%GVF and 20%GVF inlets. Noticing the head degradation becomes worse at high GVF and the degradation is worst at first stage, something unique is happening inside the first stage. Thus, numerical simulations are used to investigate this phenomenon.

Table 5. Comparison of single stage pressure rise in different GVF tests

P(psig)	Inlet	STAGE1 EXIT	STAGE2 EXIT	STAGE3 EXIT	Stage pressure rise
0%GVF	45.1	129.6	216.1	N/A	84.5-86.5
10%GVF	45.1	106.7	194.7	N/A	61.6-88
20%GVF	40	60.7	140.7	231.1	20.7-80-90.4

At 0% GVF, 1st stage pressure rise is 98% of that in 2nd stage. At 10% GVF 1st stage pressure rise is 70% of 2nd stage, At 20% GVF 1st stage pressure rise is 26% of 2nd stage, Comparing all three 2nd stages at different GVFs, the pressure rise changes from

86.5 psig to 88 psig and then to 80 psig, which is insignificant compared with the changes in first stage.

6.2 Simulation with fixed bubble size

The 1st stage in the 20% GVF test is chosen for study. The pressure rise inside is just 20 psi while that in the 2nd stage is 80 psi. In the first step of study, two simulations are carried out for each stage. The simulation settings are shown in Fig. 52, similar with that in previous chapter except they are single stage and for only main flow path.

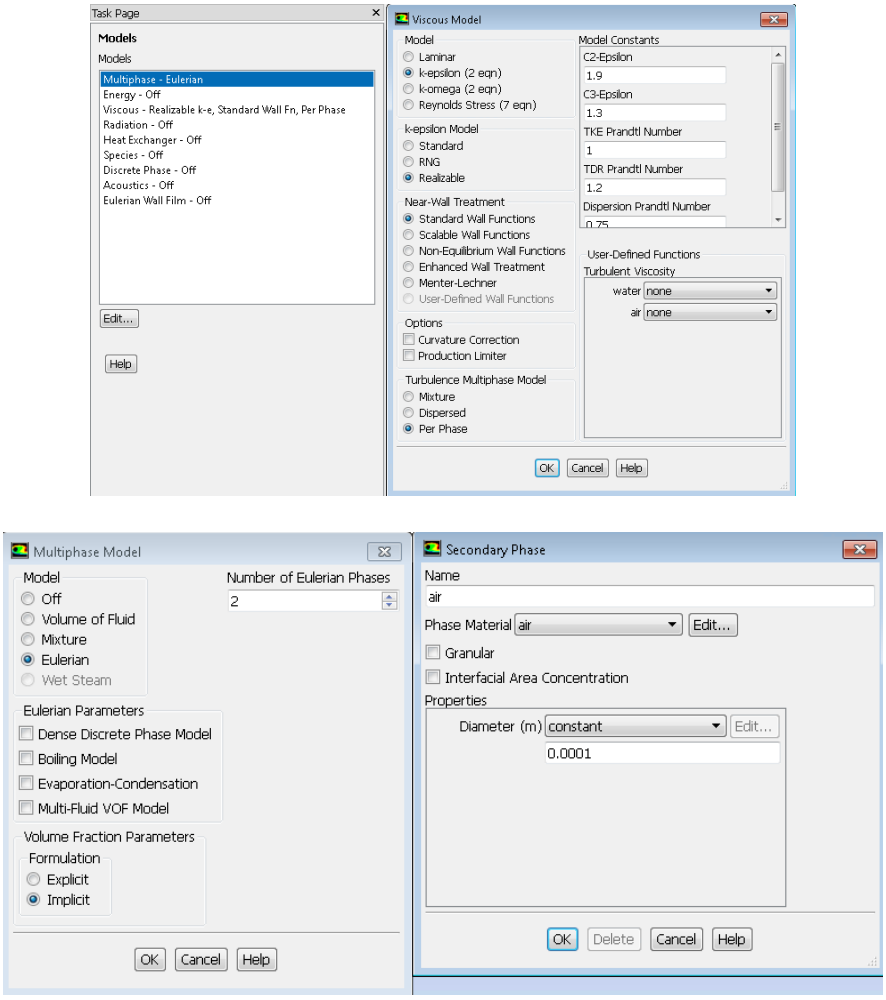

Figure 52. Fixed bubble size simulation settings for 1st & 2nd stages

For these two simulations, all conditions are identical expect the inlet pressure. Based on experiment result, the first stage outlet is set to be 60.7 psig, and second stage outlet is set to be 140.7 psig.

The predicted head rise for 2nd stage is 78.3 psi, which is acceptable compared with the experiment result 80 psi. Meanwhile the predicted head rise of 1st stage is 46.6 psi, which is more than doubled compared with the experiment result 20.7 psi. This suggests some interesting phenomenon is happening only in 1st stage, which cannot be explained by this fixed bubble size Eulerian simulation.

6.3 A hypothesis to explain the abnormal head loss in first stage

Referring to the literature review of this research, some researchers attribute the first stage difference to the inhomogeneous distribution of the inlet flow. It is true the distribution of air in the inlet can cause difference for the stage performance, but the bubbles breaking-up and coalescing effect could be the real cause for this problem.

The previous simulations set the bubble size to be fixed at 0.1mm, which agrees with previous researcher and experiment observations inside the ESPs. The reason most ESP simulation are kept at fixed bubble size from 0.1mm to 0.3 mm is that in high level turbulence flows, larger bubbles are less likely to exist. Experimental results have verified this assumption to be true. This is why the fixed bubble setting is considered questionable in this research.

Referring to the literature review part, many researchers have observed gas lock or slug flows at high GVF when they are testing with a single stage or they focus on the first stage of a multistage ESP. This does not contradict the small bubble size assumption

above. The assumption above requires high levels of turbulence, which exists in most part of the ESP flow field except the first stage impeller. The flow passing through the first stage inlet is quite 'peaceful' comparing with the flow after the impeller-diffuser blades contact zone. Large bubbles could exist easily before contacting with the first set of blades. Thus, the fixed bubble setting could be wrong for the first stage simulation. Further development of the simulation method is needed for this part. To verify if the bubble size effect is the reason for the abnormal head degradation in the 1st stage, we need to perform simulations which enable the bubble size to change, enable the bubbles to break-up and coalesce.

6.4 Work with ANSYS Fluent PBM for changing bubble size simulations

In ANSYS Fluent, the population balance model is provided as an add-on module. The purpose of this module is to solve industrial flow applications involving a secondary phase with a size distribution. The size distribution includes solid particles, bubbles, and droplets. In multiphase flows involving a size distribution, a balance equation is required to describe the changes in the particle population. This balance is referred to as the population balance. (ANSYS Fluent Population Balance Manual, 2013)

This module enables the setting of changing bubbles sizes in this research. There are in total three solution methods to the population balancing equation: discretized population balance, standard method of moments, and quadrature method of moments. In this module, the size of particles/bubbles could be set as any numbers in a continuous range. However, since the simulation needs to enable the bubbles to change sizes only

by breaking-up and coalescing, the sizes of bubbles are required to be set as a list of discrete numbers instead of any number in a continues range.

The following steps are used to set up the simulation cases with ANSYS population balancing module in this research.

1). Set everything up the same as the normal Eulerian multiphase simulation in the fixed bubble size simulation.

2). Enable the module: Type the TUI command “define models addon-module” in the console and enable the Population Balance model. The GUI now changes and an item is added to the Models menu.

3). Set the parameters for the population balance model. Go to Models-> Population balancing model. Select ‘Discrete’ from the method list, ‘Geometric Ratio’ from the definition list, and ‘air’ from the phase drop-down list. Enter 10 for Number of Bins, 2.66 for Ratio Exponent and 0.0001 m for Min. The detailed setting is shown in Fig.53.

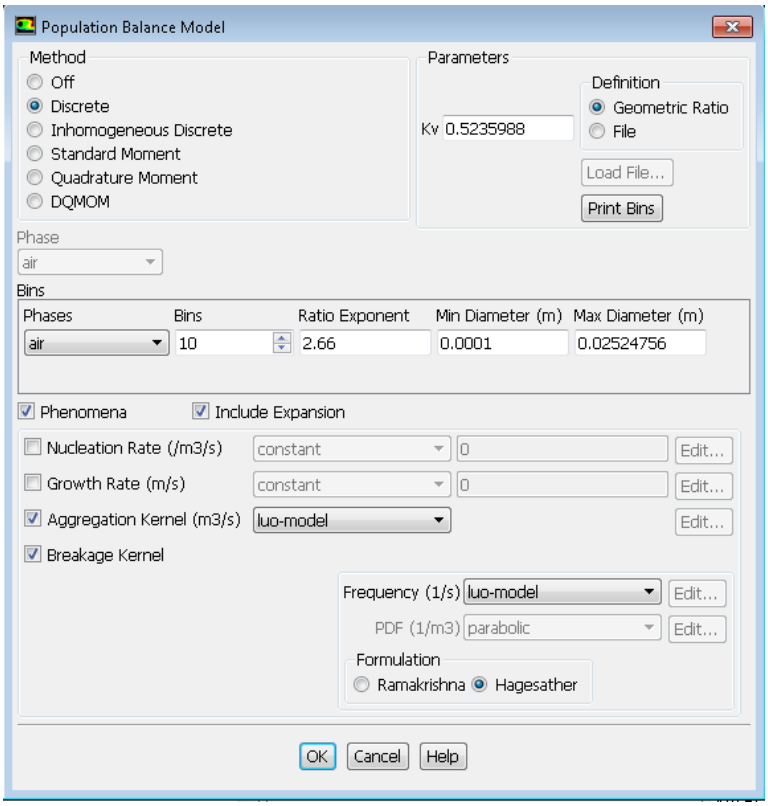

Figure 53. Settings for population balance module with ANSYS Fluent 17.1

The bins are the factors to generate the discrete list of bubble sizes. Bubbles are only allowed to break up or coalesces to the neighboring size in the list. A larger number of bins will improve the simulation result by allowing the bubble size to change more smoothly. However, a larger number of bins will also result in significant increase in simulation time. Considering both time-efficiency and accuracy, the simulations in this research use 10~12 bins beginning from the minimum size of 0.1mm.

The aggregation kernel and breakage kernel from the phenomena group box are enabled with Luo-model (Luo, 1994 & Luo, 1996) selected for both kernels. This model is developed for bubble breaking-up and coalescing simulation.

Then redefining the inlet air phase for bubble size configuration, the middle size bin-4 is selected to be the bubble size of the inlet. With this setting, the bubble sizes can change due to breaking-up and coalescing phenomenon.

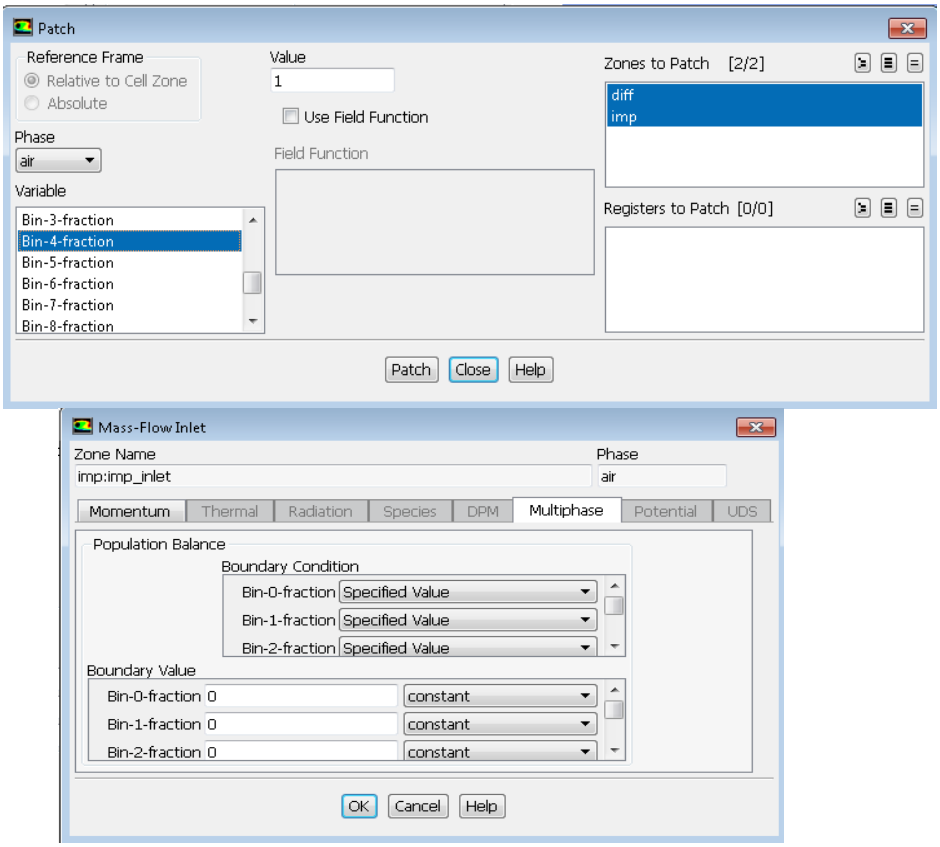

Figure 54. Bins settings for simulations in the research

6.5 Simulation results with PBM method.

Two PBM cases are set up for this part – the 1st stage of 10% GVF test and the 1st stage of the 20% GVF test. Another simulation with water only for the 1st stage of 0% GVF test is also set for comparison.

6.5.1 Pressure rise prediction in first stage

For the 1st stage in 20% GVF simulation with PBM, the predicted inlet pressure is 44 psig. The inlet pressure from the test if 40.7psig. This is a big improvement comparing with the simulation without PBM method, which predicts the inlet pressure to be 14 psig. Still there is a 3.3 psig difference from the real situation, which may be improve by further increase the number of bins and adding secondary flow paths.

The 1st stage simulation for 10% GVF case provides a better result, the predicted inlet pressure is 44 psig while the real inlet pressure is 45.1 psig

By applying the population balance module, the simulation results are much improved and more reasonable.

6.5.2 Bubble size distribution.

The discrete bubble sizes (bins) are generated and shown in Table. 6

Table 6. Discrete bubble sizes for PBM simulation. (Unit: mm)

Bin-0	Bin-1	Bin-2	Bin-3	Bin-4	Bin-5	Bin-6	Bin-7	Bin-8	Bin-9
25.2	13.7	7.39	3.99	2.16	1.17	6.32	0.342	0.185	0.1

The minimum bubble size is set to be 0.1 mm. The maximum allowed bubble size is 2.52 cm.

6.5.3 Pressure distribution

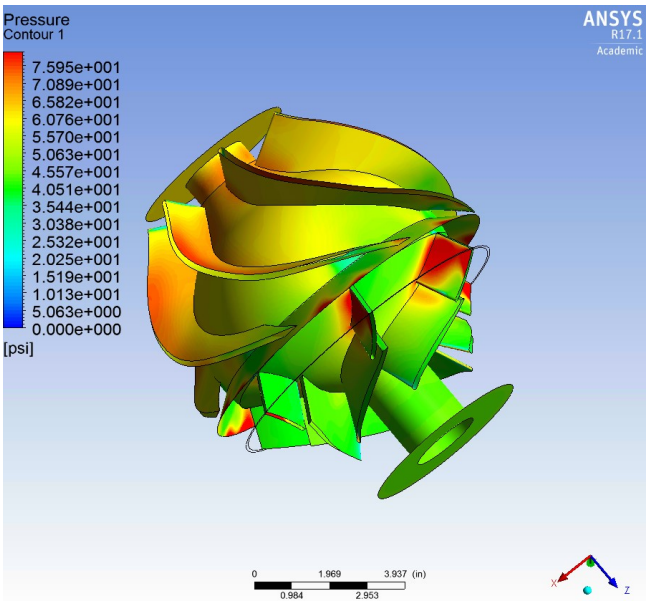

Figure 55. Pressure distribution on blades and hubs of the 1st stage at 20% GVF

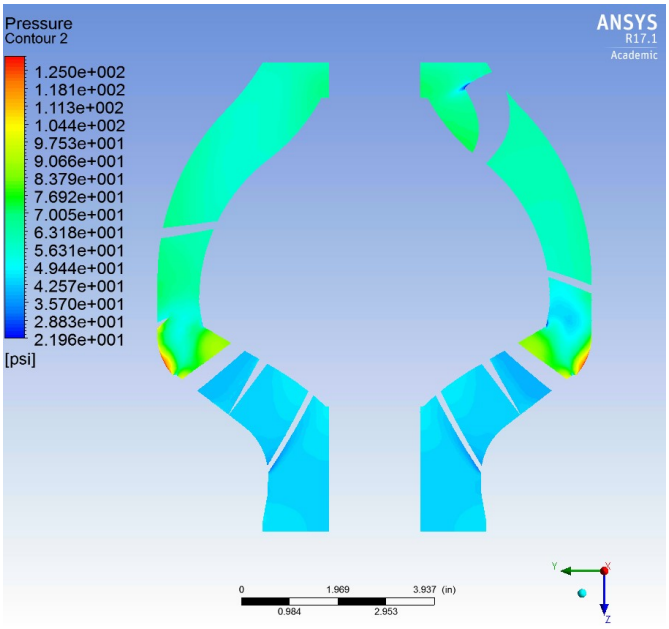

Figure 56. Pressure distribution on the section plane of the 1st stage at 20% GVF

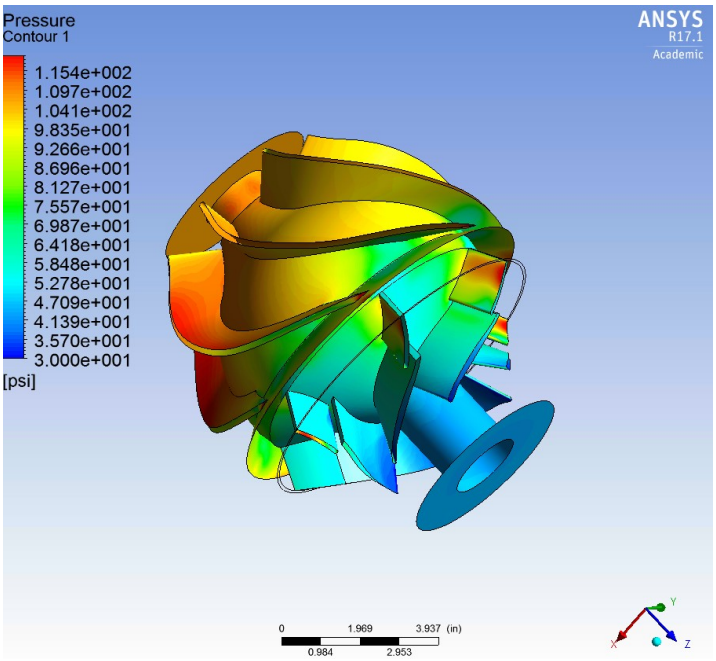

Figure 57. Pressure distribution on blades and hubs of the 1st stage at 10% GVF

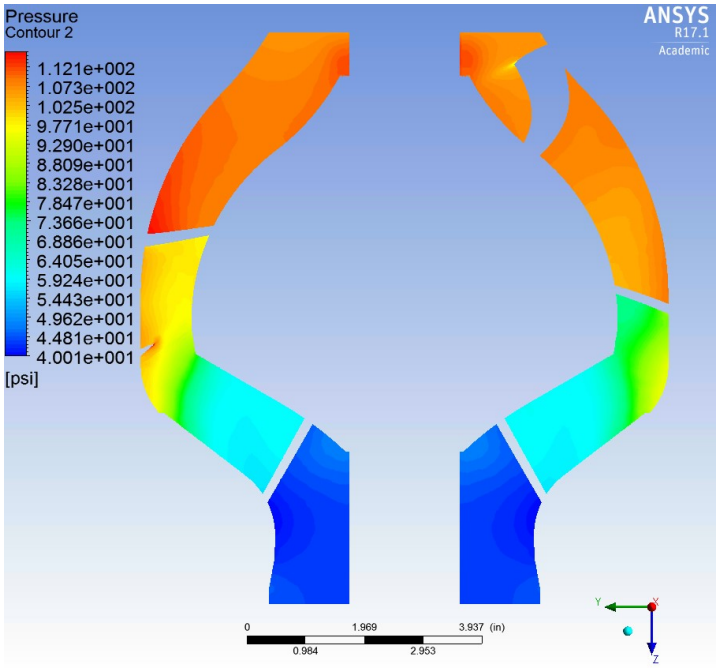

Figure 58. Pressure distribution on the section plane of the 1st stage at 10% GVF

The pressure rise in the first stage is much lower than the other stages. In the GVF20% test, the first stage the pressure rose from 40 psig at the inlet to 60 psig at the outlet, while the second stage's pressure rose from 60psig to 140 psig. Fig. 55 and Fig. 56 show that inside the first stage there exists high pressure above 100 psig near the blade contact zones. Then the pressure is quickly reduced to around 60 psig along the flow path. The pressure rise inside a pump is generated by resistance of fluid motion slowing it down and centrifugal force. There is something unique that absorbs the forces and energy in the first stage. There are two possible mechanisms causing this phenomenon. First, the large gas slugs near the impeller blades are compressible and act as springs, damping resisting force and transfer the kinetic energy to internal energy. Second, the large bubbles in the impeller breaks into much smaller bubbles in diffuser with the chopping effect of the blades interacting which generates high turbulent zones and absorbs kinetic energy.

6.5.4 Air volume distribution

The basic idea of the PBM simulation in this research is to uniformly inject medium size of bubbles and then allow them to break-up and coalesce within the first stage under the luo-model for aggregation and breakage. To verify the breaking-up and coalescing phenomenon does occur in the first stage, especially in the first impeller, the volume rendering method is used to show the bin fraction distribution inside the first stage. The bin fraction distributions for 10%GVF and 20%GVF are shown separately in Fig. 59 and Fig. 60. Note the volume rendering is created by visualization of variable gradient layer by layer, thus will appears not smooth in some regions.

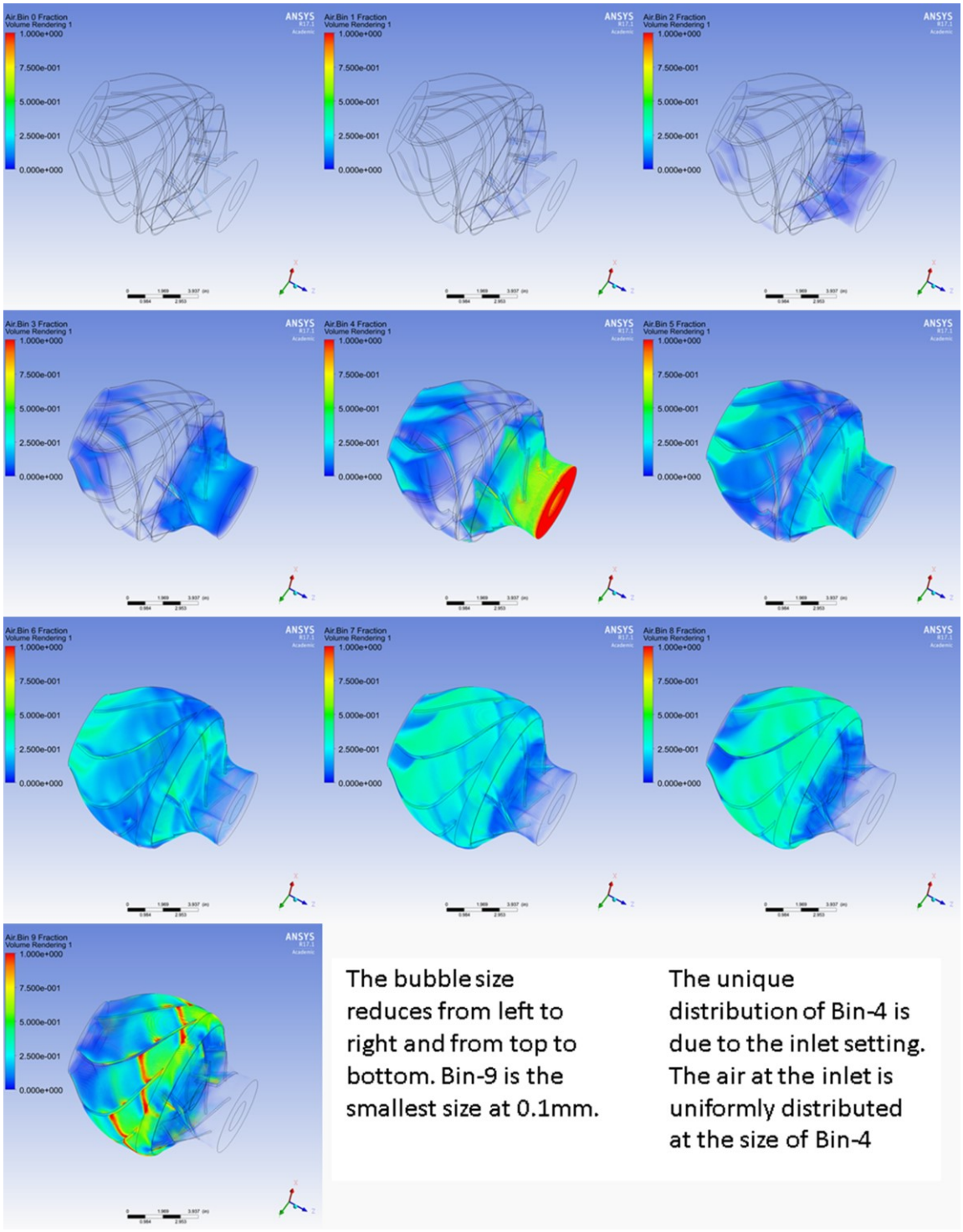

Figure 59. Bin fraction distribution for 1st stage of 10% GVF simulation

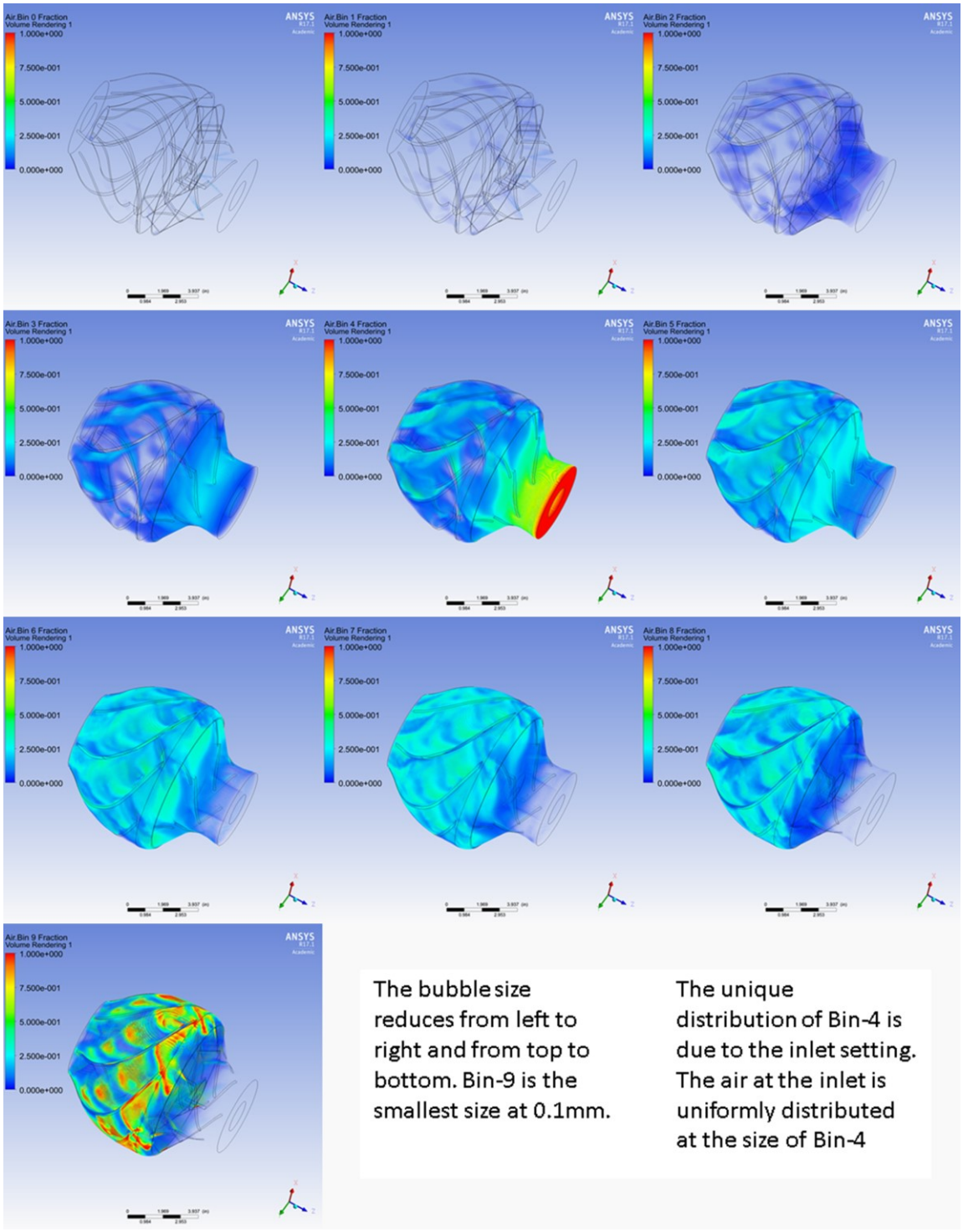

Figure 60. Bin fraction distribution for 1st stage of 20% GVF simulation

From Fig. 59 and Fig. 60, larger bubbles tend to exist in the first impeller, ahead of the blades contact zone. After the flow passes contact zone and enters the first diffuser, the bubble size become much smaller. The largest fractions of bubble sizes after the contact zone are bin-7~ bin-9 (size 0.1mm to 0.34mm), which agrees with previous observations from experiment. The distribution of bin-4 is different with others since it is the inlet bubble size set in the inlet condition. These volume renderings show the middle-sized inlet bubbles quickly coalesce into larger ones in the first impeller and then break into small ones in diffuser.

The bins fractions are only the distribution of bubble sizes. Higher bin fraction in the flow region does not necessarily mean there are many bubbles at this size in this location, since we also need to consider the total air volume fraction. Fig. 61 shows the volume rendering of air volume fraction inside 1st stages of 10%GVF and 20% GVF simulations.

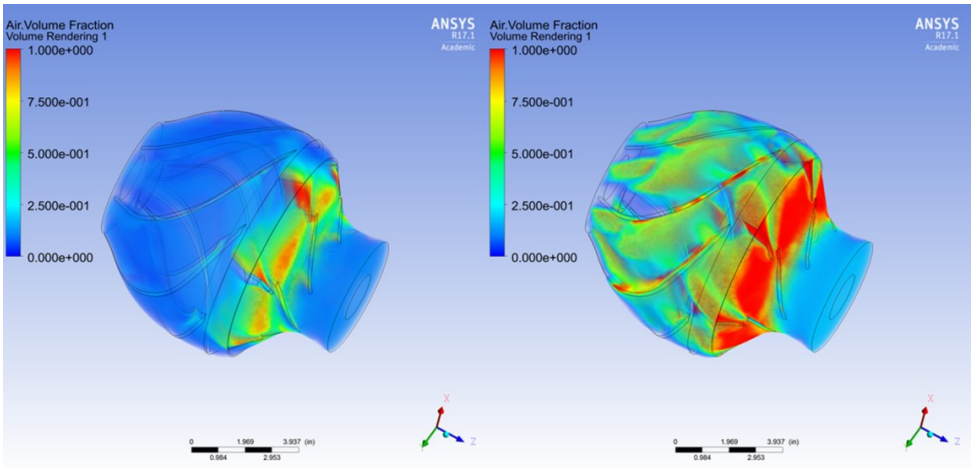

Figure 61. Air volume fraction in 1st stage of various GVF tests (Left 10% GVF, Right 20%GVF)

Combining the bin fraction and air volume fraction together, the real volume distribution of large bubbles can be obtained. Fig. 62 shows the distribution of bubbles at the size of bin 3 (4mm) in 1st stage of 20% GVF simulation. The threshold in Fig. 62 is set as 10%. The colored zones are places where big bubbles at the size of bin 2 exist and occupy over 10% of the local volume.

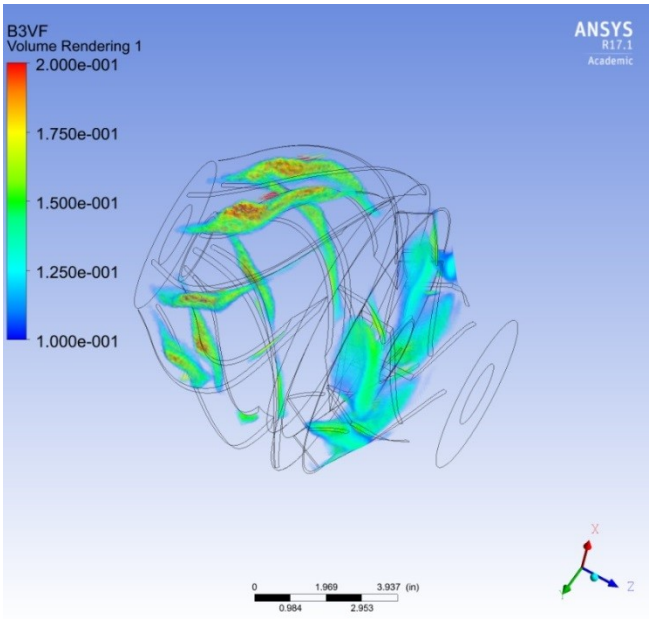

Figure 62. Example of large bubble (4 mm) existence in simulation

6.5.5 Comparison of flow field inside 1st impeller with and without PBM

With all data obtained from the simulations with and without PBM for 1st stages, it is possible to compare the inner flow fields of these two simulation methods, and then according to experiment test result to determine which one is more reasonable. Fig. 63 shows the streamlines of water inside 1st stage of 20%GVF simulation without PBM. Fig.

64 shows the same streamlines from the simulation with PBM method. Fig. 65 shows the comparison of air streamlines inside the 1st impeller with and without PBM.

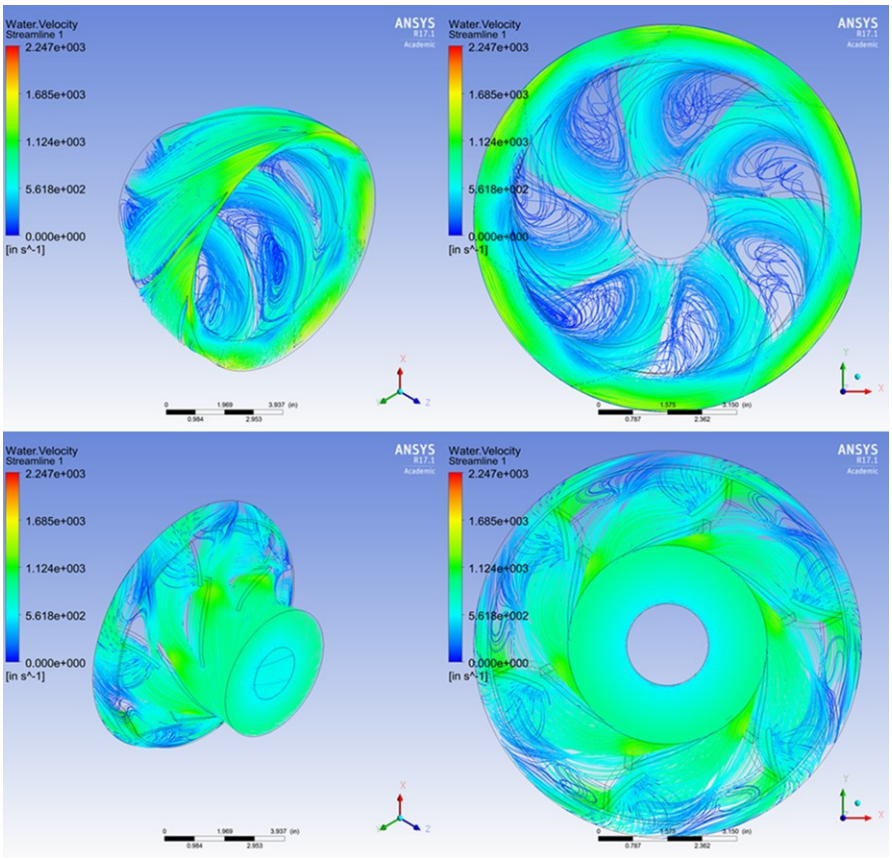

Figure 63. 3D streamlines of water inside 1st impeller at 20% GVF – no PBM

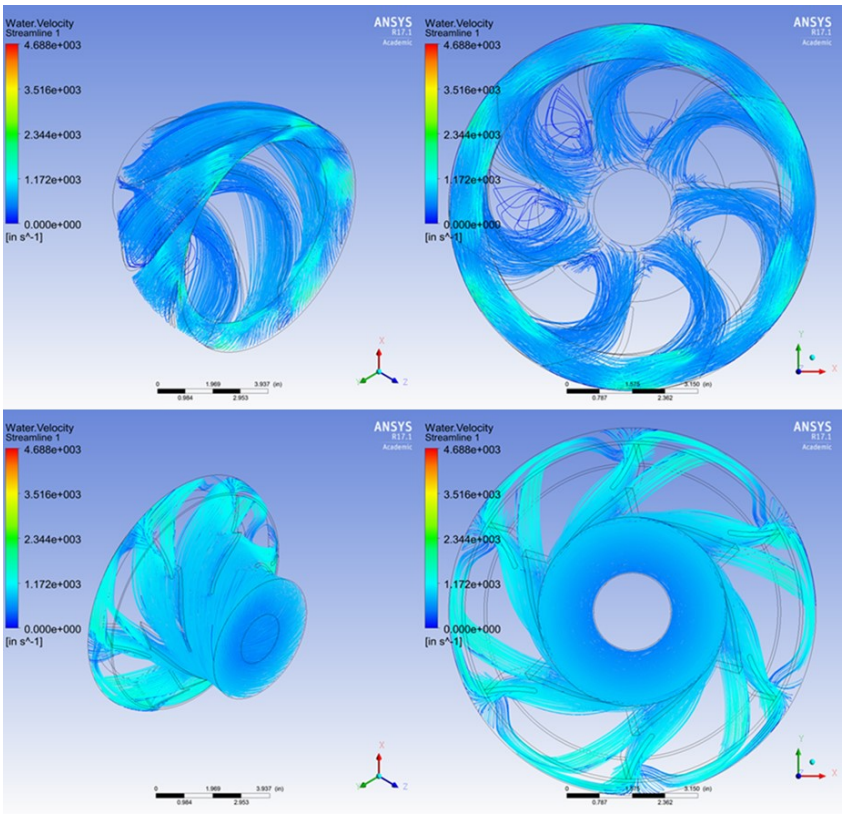

Figure 64. 3D streamlines of water inside 1st impeller at 20% GVF with PBM

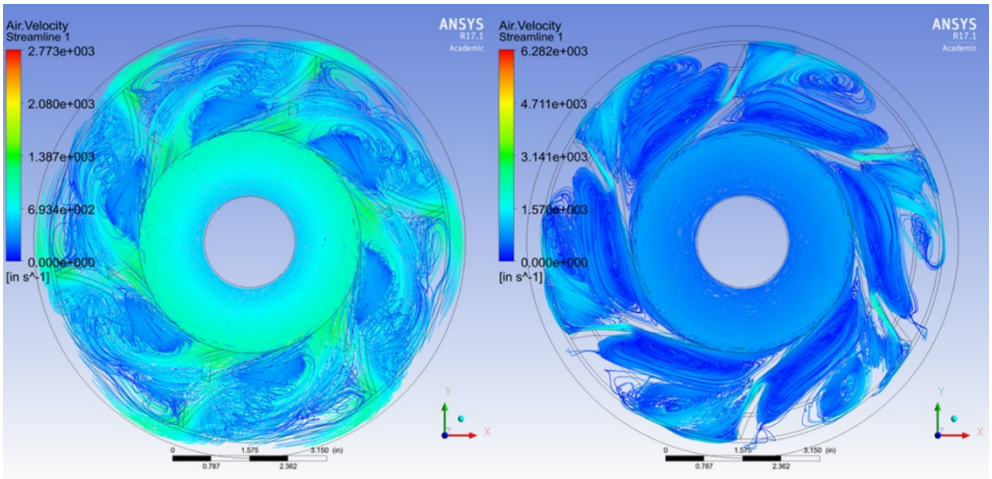

Figure 65. 3D streamlines of air inside 1st impeller at 20%GVF (Left: no PBM; Right: with PBM)

From Fig.63~65, the simulation with PBM predicts the existence of flow separation and air slug zone on the suction side of impeller blades.

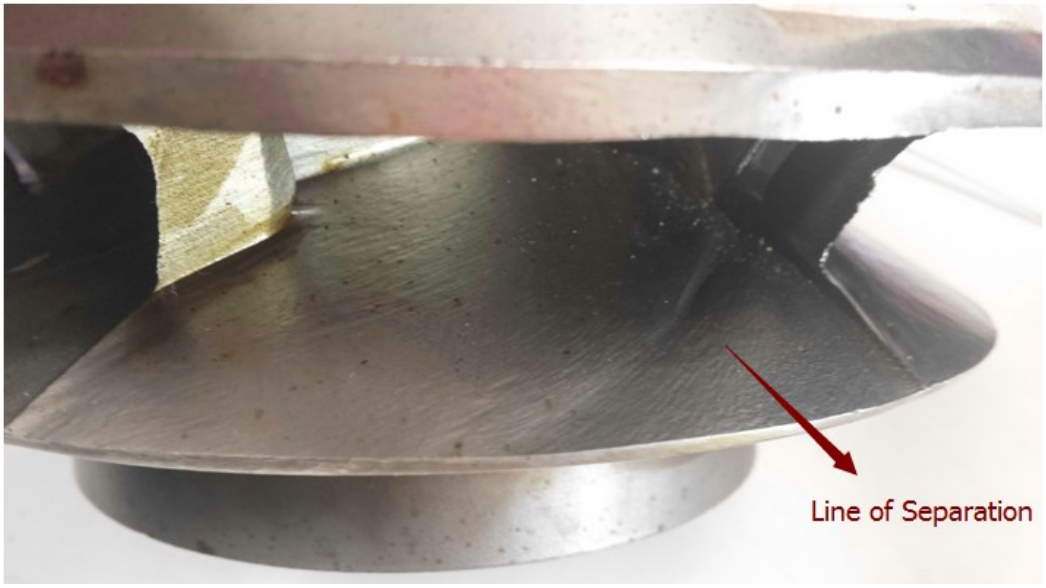

Figure 66. Experiment support of the PBM result

The simulation with PBM discovers the separation of water and air flows on the suction side of blades. The separation zone near the surface is completely occupied by gas slugs. These gas slugs narrow the main flow path and force water and sand to flow between the gas zone, resulting in a rapid injection of multiphase flow with mostly water and sand (refer to lower right picture in Fig. 64).

In the simulation results without PBM (Fig. 63), although the gas volume is high in these regions, the separation of flow is not complete. The air phase in these separation zones still coexists with the water phase, because the air phase is limited with small bubble size. Since water and sand can flow in the whole channel between the impeller

blades, the injection of flow is not observed and the velocity of water is lower compared with the PBM result.

If the PBM result is right, the surface of impeller hub will show a special erosion pattern – line of separation. The injection of flow is formed by water and sand at a high speed, while most of the air is separated in the gas slug with low speed. Based on the experiment results in Fig. 66, the separation of flow exists. Thus, the experiment result supports the PBM result and the changing bubble size hypothesis in this research.

6.5.6 Flow field inside 1st impeller at different GVFs

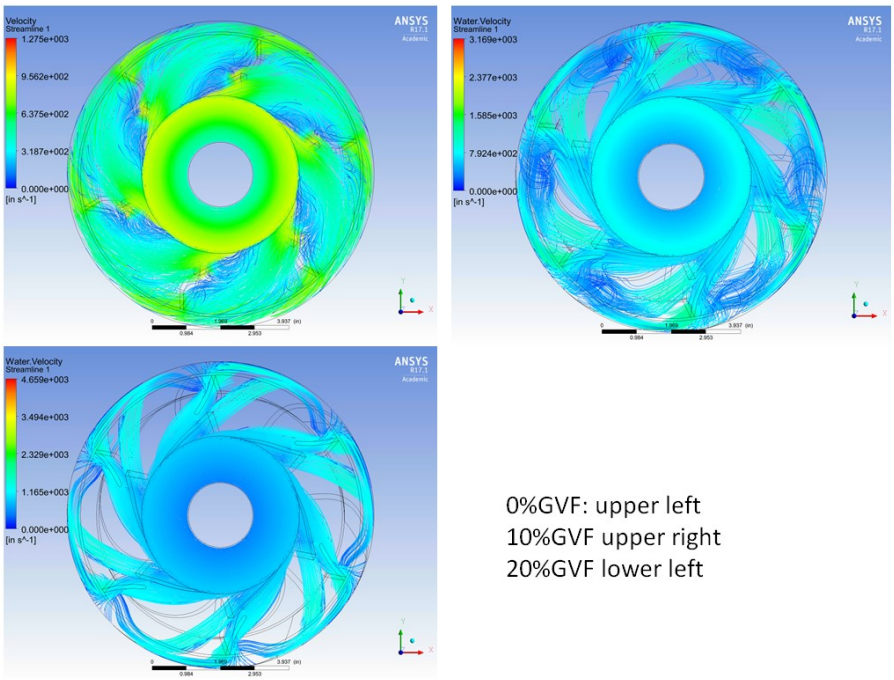

Figure 67. 3D streamlines of water in the 1st impeller at various GVFs

From Fig. 67, the separation of flows in the 1st impeller is observed and the separation zone becomes larger when the GVF increases. The accumulation of bubbles on the suction side of the exiting blades forms a gas slug and narrows the water path,

significantly increasing the velocity magnitude of water. The increased water velocity will also lead to increases in sand velocity and make the erosion in the 1st stage worse. Also, the vortices formed at high GVF condition could also contribute to the 1st stage erosion.

6.6 Summary

The pressure rise in the first stage of the G400-ESP is much smaller than that in other stages when working with high gas volume fraction. Although there are multiple reasons for this behavior, the bubble breaking-up and coalescing effect is the main cause and should be further studied. The simulation with population balancing module is a way to numerically study this problem and gives relatively better simulation results. However, it has its own drawbacks - the bubble sizes are limited to a discrete list instead of a continuous range. This method still provides a detailed illustration of the inner flow fields with large bubbles and gas blockages. The gas blocked zones in the first impeller narrows the water flow path and increases main flow velocity, which could explain the severe head degradation and often the severe erosion in the first stage. Taking the bubble size effect into consideration, the pump head degradation under high GVF circumstance is explained. Optimization of the first stage design could lead to further improvement of pump performance and life-span.

7. MULTIPHASE SIMULATION RESULTS WITH QUALITATIVE EROSION PREDICTION

Erosion is a complex phenomenon, which depends on particle properties, tracks, local flow, turbulence field, and multiphase effects (ANSYS Erosion Module 2014). Although there are many existing models for prediction of erosion, it is nearly impossible to have a universal erosion model. Different models are developed for different flow regimes, and experimental data is always needed to tune model parameters.

There are two different mechanisms of erosion: impact erosion and abrasive erosion.

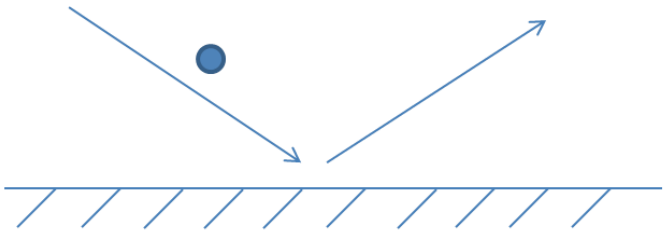

Figure 68. Illustration of impact erosion

Impact erosion is caused by the particles attacking the erosion surface at an angle. The impact erosion is caused by a single particle on a surface and is associated with the impact angle, particle's speed, density and shape, and surface materials. To obtain a

reasonable estimation of impact erosion from a simulation, all the near-wall particles' traces must be recorded over a certain amount of erosion time.

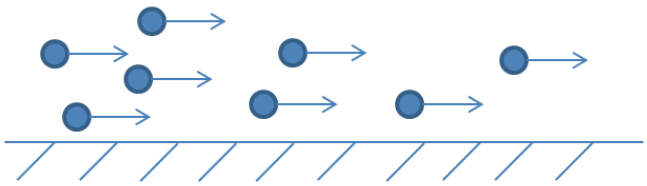

Figure 69. Illustration of abrasive erosion

Different from the impact erosion, the abrasive erosion is not caused by particles hitting the surface at an angle. Instead, they are flowing parallel to the surface and scratching the surface the same way as a piece of sand paper. Due to the difference in erosion mechanisms, impact based erosion models cannot capture the abrasive erosion. The abrasive erosion is related with particle volume fraction, particle near-wall speed, wall material and near-wall turbulence environment.

For ESP related simulations, both impact and abrasive effects are critical for the estimation of erosion. The impact erosion is possibly stronger at high turbulence zones, especially near blades since the blades alter and regulate the flow directions. Abrasive erosion could be the cause of erosion on casings and secondary flow paths, including balancing holes and bearing clearance.

7.1 Erosion prediction in Eulerian simulation

In the first part of this chapter, the Eulerian simulation is used for particle phase, which is set as granular in ANSYS Fluent. The simulation case for this part is based on the second stage of the water-sand two phase flow tested in our lab.

7.1.1 Theory

Pirouzpanah(2014) conducted a two phase simulation on particle laden flow in a mixed flow pump by applying the Eulerian-Granular scheme with ANSYS Fluent. By studying the sand fraction, near wall sand speed and liquid turbulent kinetic energy, he suggested a new erosion model for Eulerian multiphase flow.

Equations (1), (2) and (3) are used for the prediction of erosion. This prediction is qualitative. The factors A and B in Eq.2 can be altered for better prediction. The pump in Pirouzpanah's research is a WJE-1000 manufactured by Baker-Hughes, an ESP with the similar design and aspects with the G400 ESP in this research.

$$EF = \left(\alpha_s\right)^{0.08} \left(\frac{V_s}{V_{s_0}}\right)^{0.07} \left(\frac{k_w}{k_{w_0}}\right)^{1.25} \tag{1}$$

$$ER\ (\mu m / hr) = A.EF^2 + B.EF \tag{2}$$

$$A = 0.0163,\ B = 0.8774 \tag{3}$$

The critical part of post processing is to capture the near-wall data for particle phase and turbulence. The velocity on walls cannot be used since sand is supposed to be the granular phase and has no-slip condition on the erosion surface.

7.1.2 ANSYS Fluent settings

The simulation is 3D transient with gravity enabled. Turbulence model is set to be realizable k-epsilon and near-wall treatment is set as enhanced wall treatment. The turbulence multiphase model is per phase. Although for water-sand two phase flow with low sand concentration, the dispersed multiphase model provides better efficiency. Considering the ESP stage has a relatively complicated flow field and sand particles could accumulate in some regions, this simulation still uses per phase model for better accuracy. The drag coefficient for the phase interaction is set as Syamlal-Obrien, which is suitable for fluid-particle interaction. The inlet and outlet conditions are obtained from the test. The data from 2nd stage in the 0%GVF test of G400 are used as comparison for this simulation. The volume flow rate is around 40kBpd, near its best efficiency point. Inlet flow has the sand uniformly mixed at 1.5g/L.

7.1.3 Flow fields contours

Four field variables are critical to this part of research: pressure, particle volume fraction, particle velocity, and turbulence kinetic energy. The contours of these variables are shown in Fig. 70~73.

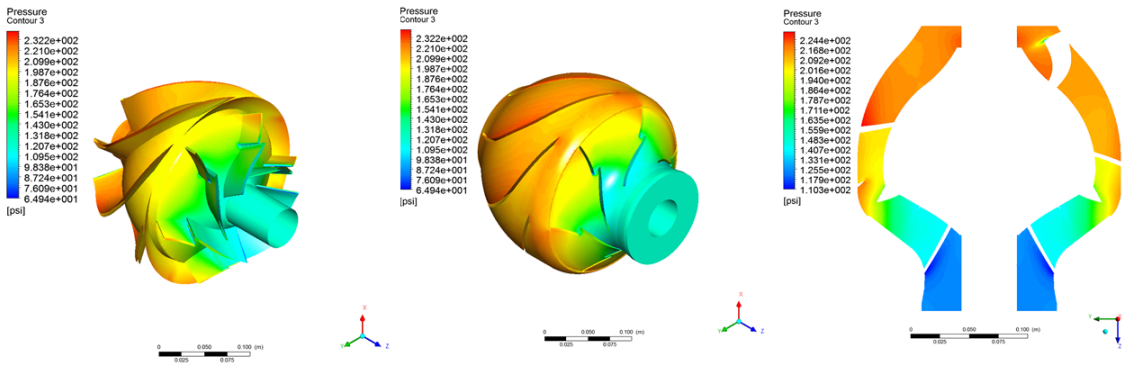

Figure 70. Static pressure distribution

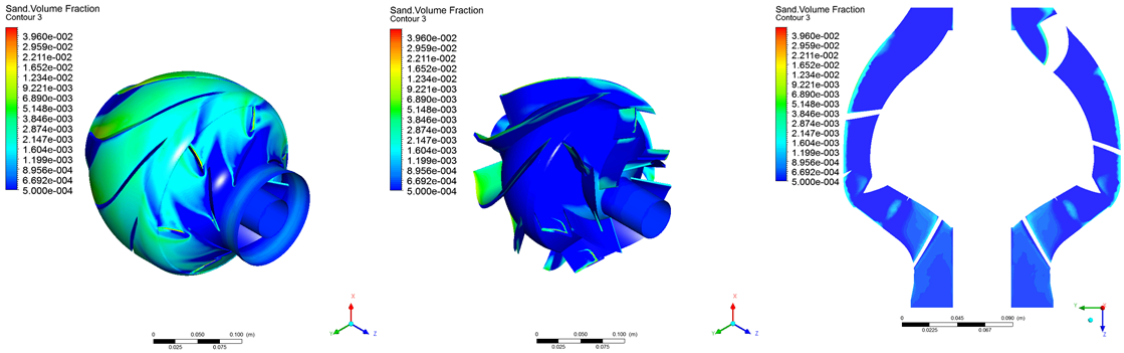

Figure 71. Sand volume fraction near wall

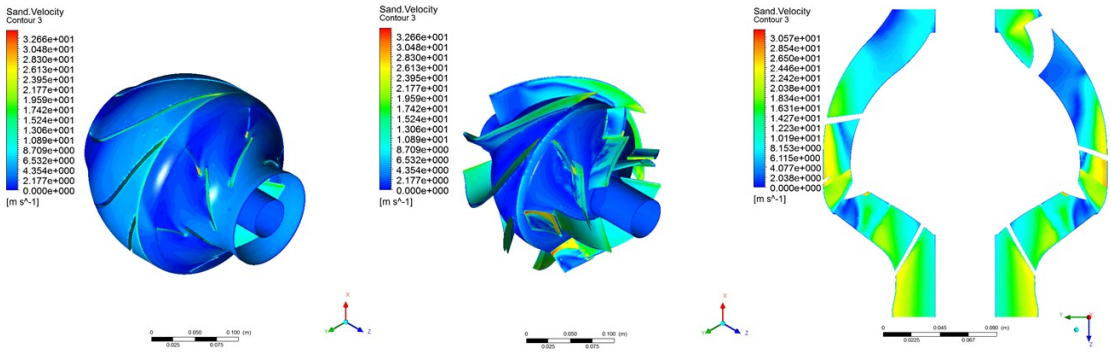

Figure 72. Sand velocity near wall

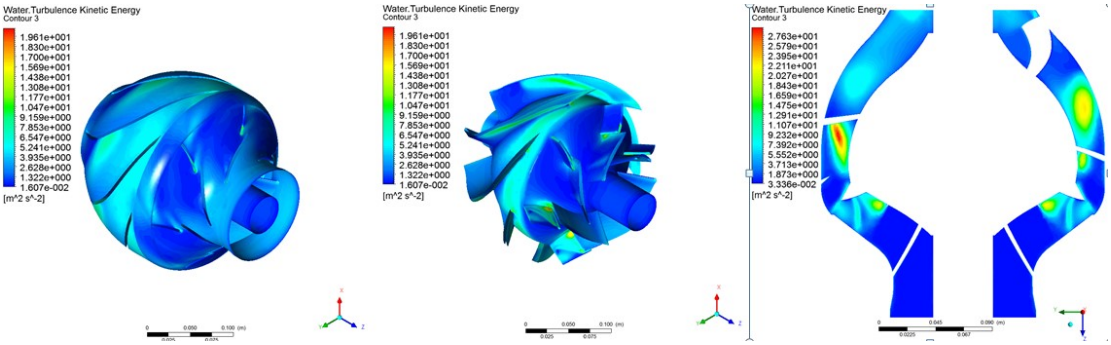

Figure 73. Water kinetic energy near wall

To investigate the inner field, blade-to-blade contours are extracted and shown in Fig. 74~76 at different locations of blades. Sand volume fraction on the pressure side of blades is higher.

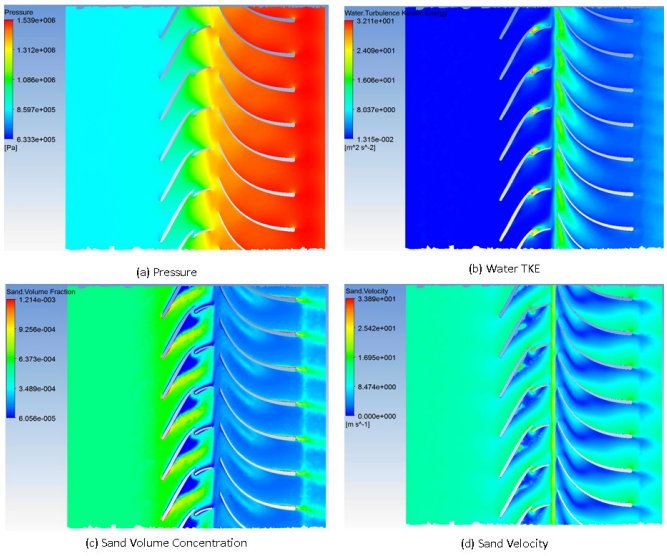

Figure 74. Blade-to-blade contour visualization @ Span=0.1

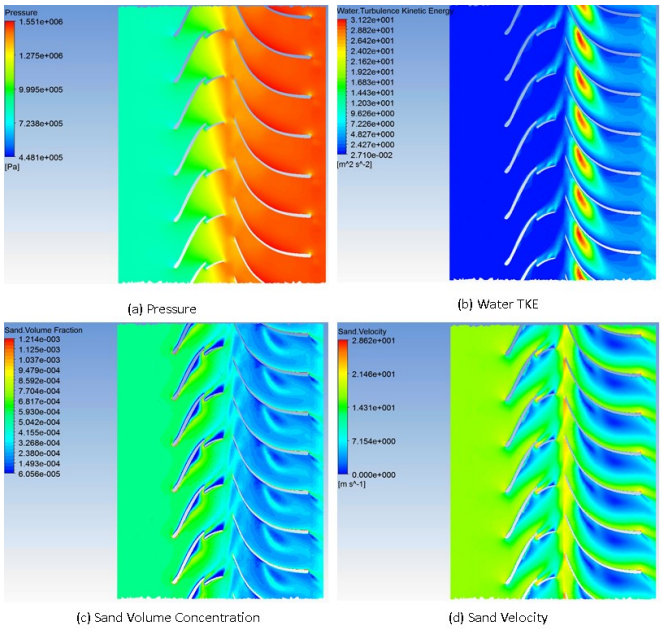

Figure 75. Blade-to-blade contour visualization @ Span=0.5

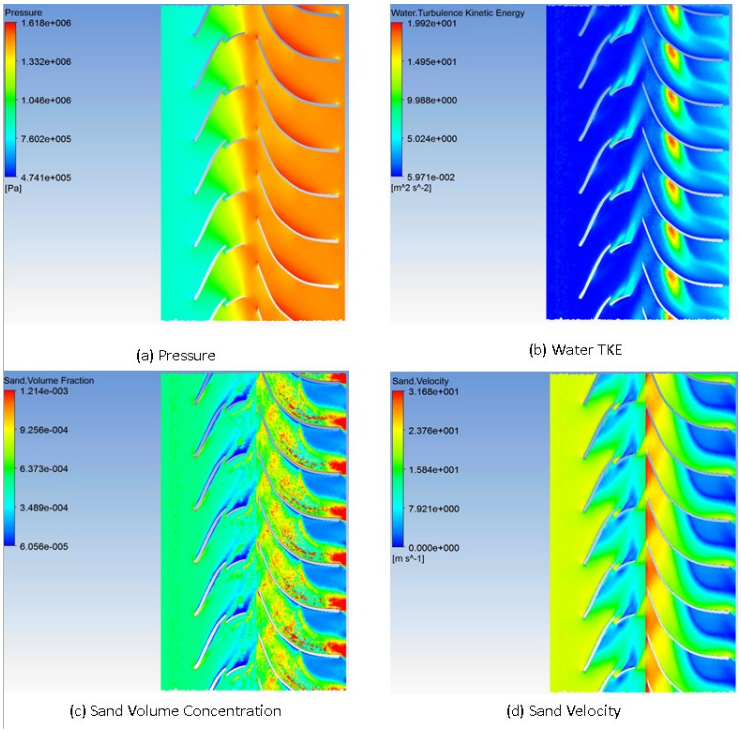

Figure 76. Blade-to-blade contour visualization @ Span=0.9

7.1.4 Erosion prediction

The predicted erosion on the leading edge of impeller blades matches with the experiments in some regions. But on the trailing edge of the blades, the result does match with the experiment, especially in the triangle erosion zone shown in Fig. 78(b). The predicted result is a line along the trailing edge in Fig. 79(a), not matching with the experiment result which shows a lower triangle zone in Fig. 79(b). The reason for this failure could be that this Eulerian approach does not take the particle impact into consideration. Another reason is that the erosion is predicted for the 0 hour geometry and the experiment result is collected after 66 hours.

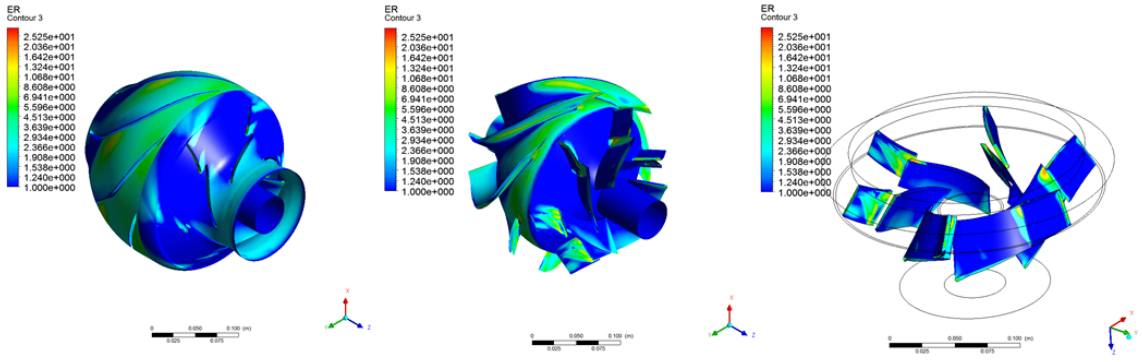

Figure 77. Eulerian erosion prediction of 2nd stage G400 0%GVF test

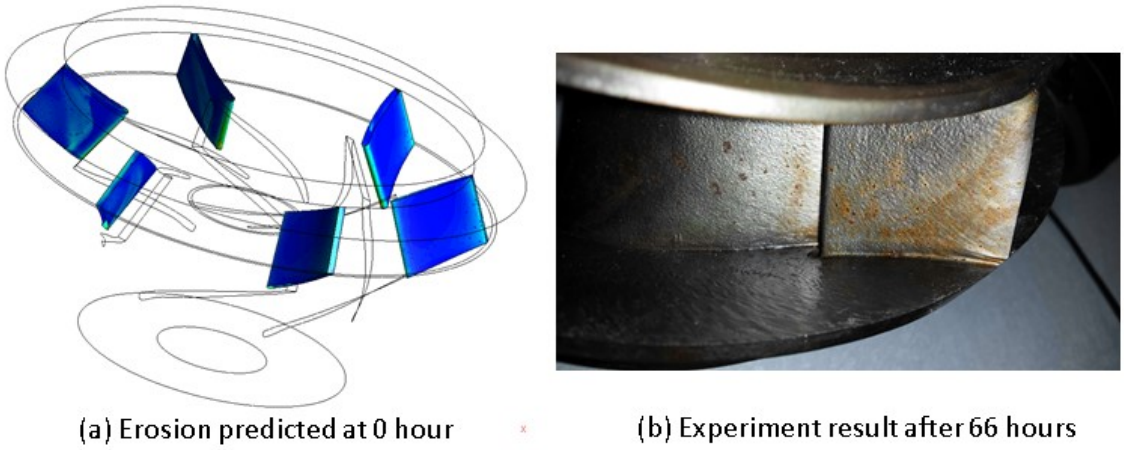

Figure 78. Predicted erosion and experiment erosion on the pressure side of impeller exiting blades

7.2 Erosion prediction with discrete phase model

The blades inside an ESP are driving/regulating the flow, so the particles' traces near the blades are often not parallel to the blade surface. The Eulerian approach in 7.1 cannot predict this part. A Lagrangian approach – discrete phase model is used for the following predictions.

7.2.1 Theory

In the discrete particle method, the particle phase is not recognized as a granular phase. Every particle in this phase is tracked and recorded with information including current position and velocity. In this approach, the continuous phase is still treated with the Eulerian method. Since this approach can provide the trace of individual particles, most impact erosion models require simulation with this discrete phase model. Instead of explicitly appearing in the models of Eulerian approach, the influence of turbulence is often implicitly contained in the models by changing particles' trace, velocity, and accretion.

The dispersed phase can exchange momentum, mass, and energy with the fluid phase. The DPM approach requires volume fraction of particle phase to be low enough so that interactions between particles can be neglected.

7.2.2 Simulation settings

In this simulation, the Eulerian phases are set the same as if there is no particle phase. Then the particle phase is added by enabling the Discrete Phase Model. The interaction between discrete phase and continuous phase is enabled, and DPS sources are updated every flow iteration. The unsteady particle tracking is updated every flow step. The pressure gradient force is selected by default, and the erosion/accretion is selected for erosion calculation.

The walls reflecting particles need to be defined with discrete phase reflection coefficients. The following normal and tangent polynomials are recommended by ANSYS and applied in this simulation.

$$R_n = 0.993 - 0.0307\alpha + 0.000475\alpha^2 - 0.00000261\alpha^3 \quad (19)$$

$$R_t = 0.988 - 0.029\alpha + 0.000643\alpha^2 - 0.00000356\alpha^3 \quad (20)$$

Eq.19 and 20 regulate the interaction between particles and walls.

The erosion simulation is not enabled before the flow field becomes stable and fully developed. Particles are uniformly injected into the impeller from the inlet and escaped from outlet. At the beginning of the simulation, the number of escaping particles increases gradually and finally approaches the injected number. Then the erosion simulation begins, which requires the integration of particles' impact erosion on walls during a certain amount of time. The erosion rate is expressed with lost material per unit time per unit area. The model used for erosion prediction is the default ANSYS Fluent erosion model (Eq.6~Eq.8), with modified impact angle functions.

7.2.3 Results and comparison

The particle traces are recorded in every time step. Fig.79 shows the particle traces recorded two rotations after particle injection.

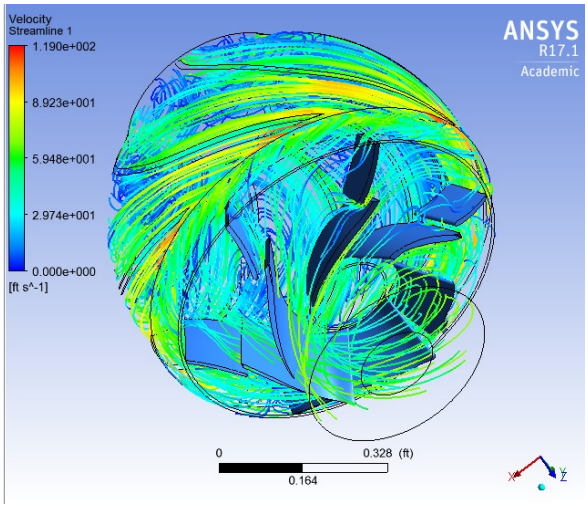

Figure 79. Tracked particle trace with Discrete Phase Model

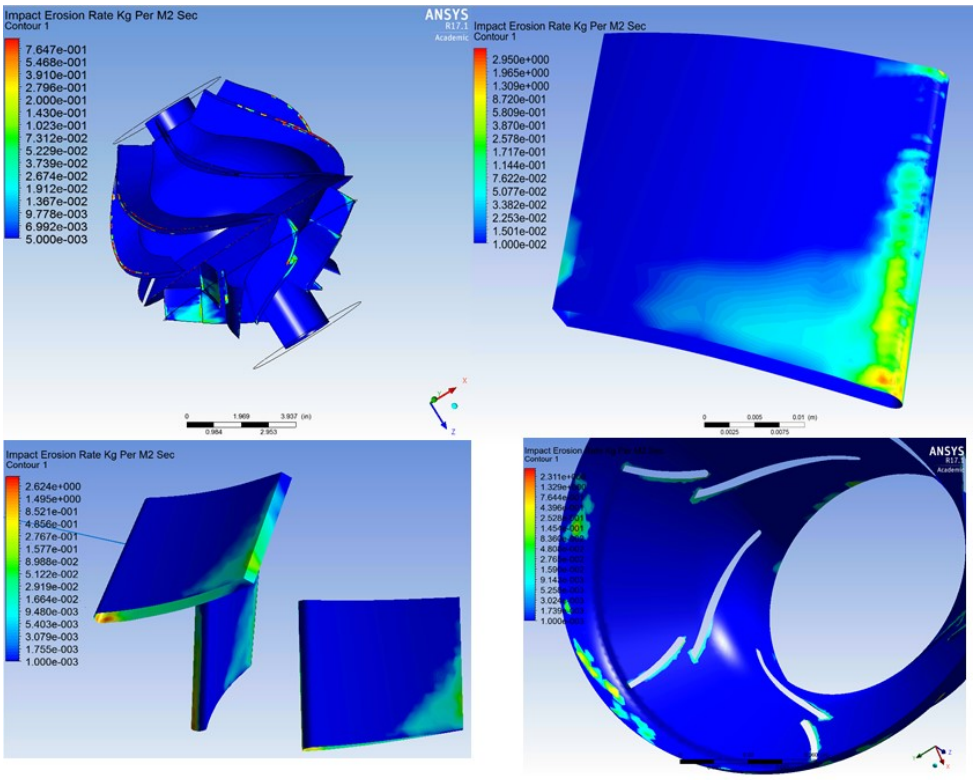

Figure 80. Various impact erosion zones predicted with DPM approach.

The simulation detects erosion in the following regions: leading edge on impeller blades, erosion on both pressure side and suction side of impeller exiting blades, and the erosion in the contact corner between impeller blades and shroud. These erosions zones are verified in Fig.81.

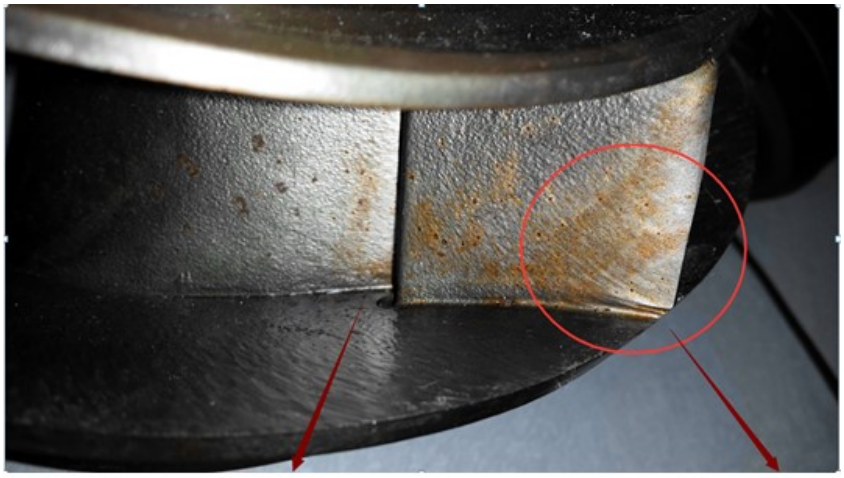

Figure 81. Erosion occurred at the same position predicted by impact erosion prediction.

With this DPM approach, the erosion prediction on impeller blades matches well with the experimental data.

7.3 The prediction of abrasive erosion on 1st impeller hub

Comparing results from 7.1 and 7.2, the discrete phase model proves its value in the erosion prediction on blades. However, when it comes to abrasive erosion the Eulerian approach works better. In Fig.82, the Eulerian model successfully predicts the erosion on the impeller hub of the 1st stage. This erosion is caused by the high-speed flow flushing on the hub after the flow separation. Since the flow direction is almost parallel to the surface, the impact erosion models based on DPM cannot predict this eroded line, which is clearly observed in experiment.

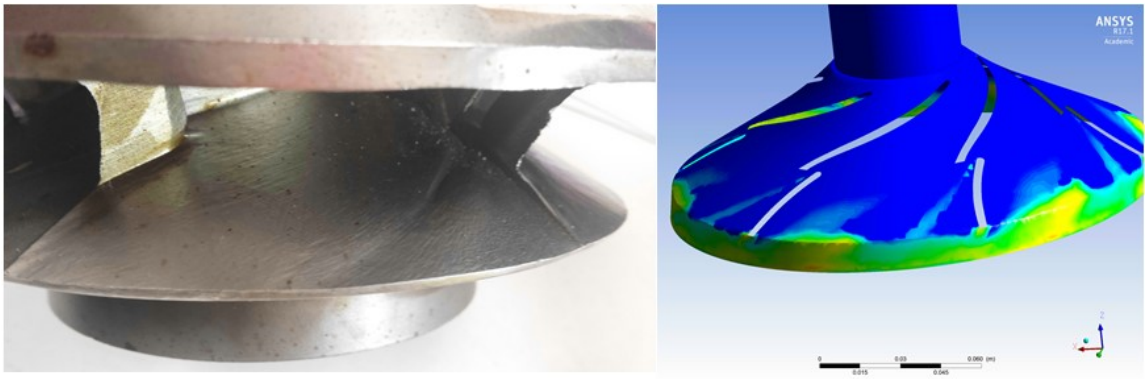

Figure 82. Abrasive erosion on impeller hub (1st stage, 20%GVF)

7.4 Discussion and summary

Due to the complicity of erosion processes, erosion prediction is always a challenge for numerical simulations. The two major forms of erosion, impact erosion and abrasive erosion, must be treated separately with different solution methods and models. The Eulerian approach is suitable for abrasive erosion prediction. When it comes to the impact erosion, only discrete phase model works for now. With so many existing erosion models, the qualitative prediction can be obtained. Quantitative prediction requires large numbers of experimental data for materials and particle properties, and data for interaction process including the impact and abrasive function.

Another problem of current ESP erosion research is that most simulations are for the uneroded mesh. The erosion rate calculated is only comparable with the initial experimental data. The after-erosion geometry could be very different from the initial one. Fig. 83 shows the first stage impeller blades from G400 20%GVF test after 66 hours. Fig. 84 shows the predicted erosion rate on the exiting blades at 0 with DPM. The predicted erosion zones make sense but are still different from the experiment.

Figure 83. 1st stage impeller blades after G400 20%GVF test

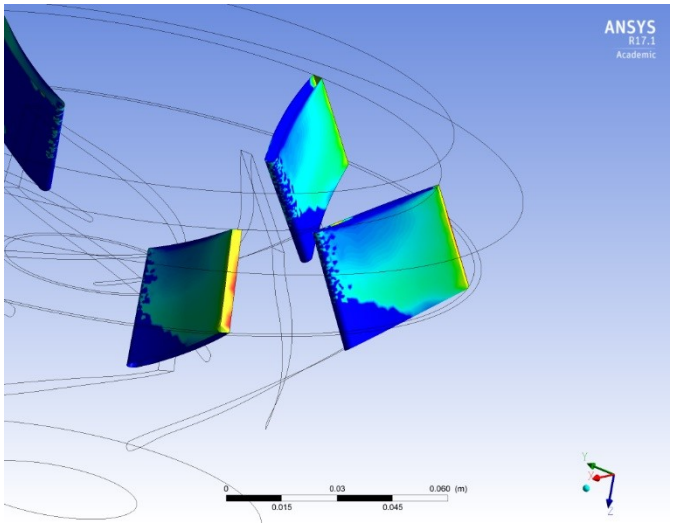

Figure 84. Predicted erosion zone one exiting blades

ANSYS Fluent provides the DPM simulation with dynamic mesh, which works in some test simulation on L-shaped elbow. However, for high speed rotating turbomachinery with complex surfaces, the time and computing resources this method consumes are usually unacceptable for industry.

8. CONCLUSION AND RECOMMENDATIONS

This research focuses on three parts of the G400 ESP using numerical simulations: the secondary flow path, the abnormal first stage pressure degradation and the erosion prediction. Various simulation cases are established and validated using experimental data.

A two-stage simulation with three Eulerian phases is completed including all secondary flow paths. The volume flow rate in the secondary flow path is much lower compared with the main flow stream with the flow field complicated by backward flow and separation of different phases. The secondary flow path allows about 1%~2% of the total flow recirculate to the pump inlet, resulting in some head loss and erosion in the clearances, which can cause further bearing and pump failure. Due to density and viscosity differences not all phases of the flow are in the same direction in secondary flow paths, resulting in separation of the flow and trapped vortices in some zones along the secondary flow paths. Gas accumulation is also observed on the suction side of the impeller exiting blades. The sand phase flows backwards at a considerable rate in the bearing clearance and stage clearance, resulting in abrasive erosion in the secondary flow channel and on the bearing surfaces. The accumulation of sand is also observed in some regions due to vortices, which can contribute to the pump failure.

The performance data from experiments show the first stage's abnormal behavior. This stage often shows significantly higher pressure degradation compared with other stages when gas is added to the system. This pressure degradation is also increased at higher GVF. Another interesting discovery is that only the first stage

performance cannot be simulated well by the fixed bubble size simulation. Other stages at various GVFs match well with the constant bubble size simulation. An hypothesis is made to explain this phenomenon – the bubbles inside first stage are affected by breaking-up and coalescing processes resulting in their sizes changing. To test this hypothesis, simulations using a population balancing module are performed and show reasonable results matching with the experimental data. This method provides detailed illustrations of the inner flow fields with large bubbles and gas locks, which are supported by experiment results. The gas locked zones in the first impeller narrows the water flow path and increases main flow velocity, which can explain the severe head degradation and erosion in the first stage. Taking the bubble size effect into consideration, the pump head degradation under high GVF circumstance is better analyzed. Optimization of the first stage design could lead to further improvement of pump performance and life-span.

Simulations for multiphase flow with sand phase are performed with two different models: Eulerian multiphase models and discrete phase model. Qualitative erosion predictions are made with both models. The Eulerian models works better for the abrasive erosion on the shroud and hub. The impact erosion from DPM gives better prediction on the blades. Without enough experimental data for the fundamental properties of material, particle and impact angle, the accuracy of the prediction is limited.

For the future work, an experimental investigation into the flow field of the first stage is recommended. Erosion in the secondary flow path should be further studied with

the bearing test facility. New erosion models need to be developed and the dynamic erosion process in ESPs can be made with updated software and hardware.

REFERENCES

ANSYS® Fluent, (2013), "ANSYS Fluent population balance module manual", Release 12.0, Help System, ANSYS, Inc.

ANSYS® Fluent, (2014), "ANSYS Fluent erosion module manual", Release 15.0, Help System, ANSYS, Inc.

ANSYS® Fluent, (2016), "Fluent guide", Release 17.1, Help System, ANSYS, Inc.

Baker Hughes, (2010), "Electrical submersible pumps", retrieved 01/09/2016, from https://www.bakerhughes.com/news-and-media/resources/brochures/multiphase-pump.

Barrios, J. B., (2007), "Visualization and modeling of multiphase performance inside an electrical submersible pump", Ph.D. Dissertation, the University of Tulsa, Tulsa, Oklahoma.

Caridad, J. & Kenyery, F., (2004), "CFD analysis of electric submersible pumps (ESP) handling two-phase mixtures", Journal of Energy Resources Technology, 126, 99-104.

Gamboa, J. and Prado, M., (2010), "Visualization study of the performance breakdown in the two-phase performance of an electrical submersible pump", Proceedings of 26th International Pump Users Symposium, Houston, 16-18 March, 2010.

Gudigopuram, S., (2016), "Experimental and CFD simulation of a helico-axial pump", Ph.D. Dissertation, Texas A&M University, College Station, Texas.

Izturiz, D.L., (2007), "Effect of bubble size on an ESP performance handling two-phase flow conditions", Master Thesis, Simón Bolívar University, Sartenejas, Caracas, Miranda, Venezuela.

Kirkland, K., (2013), “Design and fabrication of a vertical pump multiphase flow loop”, Master Dissertation, Texas A&M University, College Station, Texas.

Krüger, S., Martin, N., Dupont, P., (2010), “Assessment of wear erosion in pump impellers”, Proceedings of the Twenty Sixth International Pump, Users Symposium.

Lea, J., (1982), “Effect of gaseous fluids on submersible pump performance”, Journal of Petroleum Technology 34(12): 2922.

Luo, H., (1994), “Coalescence, breakup and liquid circulation in bubble column reactors”. Ph.D. Dissertation, the Norwegian Institute of Technology, Trondheim, Norway.

Luo, H. and Svendsen, H. F., (1996), “Theoretical Model for Drop and Bubble Breakup in Turbulent Dispersions”, AIChE Journal, 42(5): 1225–1233.

Marsis, G. E., (2012), “CFD simulation and experimental testing of multiphase flow inside the MVP electrical submersible pump”, Ph.D. Dissertation, Texas A&M University, College Station, Texas.

Mitsukiyo, M. and Kiyoshi, M., (1974a), “Effects of entrained air on the performance of a centrifugal pump : 1st report, performance and flow conditions”, Bulletin of JSME 17(110): 1047-1055.

Mitsukiyo, M. and Kiyoshi, M., (1974b), “Effects of entrained air on the performance of centrifugal pumps : 2nd report, effects of number of bades”, Bulletin of JSME 17(112): 1286-1295.

Nguyen, T., (2011), “Advanced artificial lift methods”, retrieved 01/09/2017 from http://www.nmt.edu/~petro/faculty/Nguyen/PE571/Presentation/C1/1_IntroductionToArtificialLiftMethods.ppt.

Pagalthivarthi, K. V., Gupta, P. K., Tyagi, (2011), “CFD prediction of erosion wear in centrifugal slurry pumps for dilute slurry flows”, The Journal of Computational Multiphase Flows, P224-245.

Petrowiki, (2016), “Electrical submersible pumps”, Retrieved 09/09/2016, from http://petrowiki.org/Electrical_submersible_pumps.

Pineda, Hugo *et al.*, (2016), “Phase distribution analysis in an Electrical Submersible Pump (ESP) inlet handling water–air two-phase flow using Computational Fluid Dynamics (CFD)”, Journal of Petroleum Science and Engineering, 139 (2016) 49–61.

Pirouzpanah, S., (2014), “Experimental measurement of multiphase flow and CFD erosion modeling in electrical submersible pumps”, Ph.D. Dissertation, Texas A&M University, College Station, Texas.

Poullikkas, A., (2003), “Effects of two-phase liquid-gas flow on the performance of nuclear reactor cooling pumps”, Progress in Nuclear Energy 42(1): 3.

Sahand Pirouzpanah and Gerald L. Morrison, (2014), “Predictive erosion modeling in an esp pump”, Proceedings of the ASME 2014 4th Joint US-European Fluids Engineering Division Summer Meeting, FEDSM2014, August 3-7, 2014, Chicago, Illinois, USA.

Salehi, E., Gamboa, .J and Prado, M., (2013), “Experimental studies on the effect of the number of stages on the performance of an electrical submersible pump in two-phase

flow conditions", WIT Transactions on the Built Environment, Vol 129, p227-237, WIT Press.

Sato, S., Furukawa, A., Takamatsu, Y., (1996), "Air-water two-phase flow performance of centrifugal pump impellers with various blade angles", JSME International Journal, 223-229.

Sekoguchi, K., Takada, S., and Kanemori, Y., (1984), "Study of air-water two-phase centrifugal pump by means of electric resistivity probe technique for void fraction measurement; first report, measurement of void fraction distribution in a radial impeller", Bulletin of JSME 27(227): 227-213, 931-938.

Steck D., (2014), "Experimental study of multiphase pump wear", Master Dissertation, Texas A&M University, College Station, Texas.

Zheng, D., (2014), "Three phase erosion testing and vibration analysis of an electrical submersible pump", Master Dissertation, Texas A&M University, College Station, Texas.

Zhou, D., (2010), "Simple Model of Electric Submersible Pump In Gassy Well", Journal of Petroleum Science & Engineering, 70(3-4): 204.

Zhu, Jianjun and Zhang, Hong-quan, (2014), "CFD simulation of ESP performance and bubble size estimation under gassy conditions", SPE Annual Technical Conference and Exhibition, 27-29 October, Amsterdam, The Netherlands.